MODELING AND CONTROL OF VARIOUS STYLES OF PAPER MACHINE HEADBOXES

By

Angelo G. Facca

Submitted to the Faculty of Engineering

In

Partial Fulfillment of the Requirements for the

Master of Science in Engineering Degree

Lakehead University

Thunder Bay, Ontario

Canada, P7B 5E1

December 1, 2002

ABSTRACT

In this thesis non-linear mathematical models of a typical paper machine approach system with three different styles of headboxes are presented. The non-linear models include the dynamics of the fan pump, DC motor, pressure screen, attenuator, headbox and piping sections. Headbox models of a hydraulic and two air-cushioned headboxes (traditional and internal weir) are covered. The models were developed from first principles.

Total head at the headbox slice is controlled by manipulation of the applied armature voltage of the variable speed DC motor. Stock level in the air-cushioned headboxes is controlled by manipulation of the air pad bleed valve. Simple analog Proportional-Integral (PI) controllers were selected to track without offset the desired level and total head set-points. The downhill simplex method developed by Nelder and Mead was used for controller fine-tuning. The performance criterion was the integrated absolute error (IAE) with weighting factors for both pressure and level loops.

Frequency responses for each model were generated using a commercially available software program called EASY5™. Step and frequency response plots were generated at operating points of 60, 75 and 90 kPa to evaluate the non-linear behaviour of each headbox model. The step response plots highlighted the strong interaction that exists between level and pressure loops of the air-cushioned headboxes. With the PI gains used the transient responses of the pressure loop of all headboxes were underdamped. The open-loop frequency responses in all models illustrated the non-linearity of the centrifugal fan pump. In addition the effect of the fan pump on the stock level and total head was found to be strong. The effect of the bleed valve on the stock level was also determined to be strong. With the traditional headbox the effect of the bleed valve on the total head was found to be weak whereas with the weir headbox at low frequencies it was found to be strong.

One-way decoupling was proposed to improve the control performance of the air-cushioned headbox level loop. For simplicity a lead / lag compensator was selected to approximate the ideal decoupling frequency response determined directly from the open-loop frequency responses. A significant reduction in stock level deviations before and after the addition of one-way decoupling in both the time and frequency domain was observed thereby proving its usefulness when combined with the feedback PI controllers.

ACKNOWLEDGEMENTS

I would like to thank Dr. A. Gilbert and Dr. K. Natarajan for their assistance. Furthermore to Cascades Fines Papers Group Thunder Bay Inc. for providing some of the research material referenced throughout the report.

TABLE OF CONTENTS

LIST OF FIGURES

LIST OF TABLES

CHAPTER 1

Introduction to the Paper Making Process and the Headbox

1.1 Introduction

Pulp from a machine chest is pumped through the approach system to the paper machine as illustrated in Figure 1. The approach system consists of the section of piping between the storage chest and the headbox. A typical approach system consists of primary and secondary centrifugal fan pumps, a bank of centrifugal cleaners, a pressure screen, and a headbox. The most important component of the entire flow system is the headbox itself since it distributes pulp evenly to the paper machine where it is transformed into usable paper products.

The thick stock from the storage chest at about 3% consistency is diluted with white-water from the wire pit and mixed by the action of the primary centrifugal fan pump. The stock consistency that emerges from the centrifugal fan pump has a consistency of less than 1%. In papermaking, consistency refers to the weight percent of pulp contained in a stock mixture. Stock consistency is not controlled, but the consistency that exists in the approach system is a result of the basis weight settings. Basis weight is controlled via the basis weight controller that sets the position of the basis weight valve shown in Figure 1.

To remove any contaminants that are present, the stock is passed through a bank of centrifugal cleaners. Figure 2 shows a simplified vertically installed centrifugal cleaner. The feed pipe to the centrifugal cleaner enters tangentially in order to create a free vortex flow in the outer region and a forced vortex flow in the inner region of the cleaner [1]. The main job of the centrifugal cleaner besides contaminant removal is to classify pulp fibres. Pulp fibres are separated based on shape and specific surface area [1]. As a result "shives", "chop" or long fibres that are not completely developed will be rejected and sent for further refining. Different operating points in the centrifugal cleaners can be obtained by varying the "accepts" and/or "rejects" pressure settings.

The accepted pulp from the centrifugal cleaner then proceeds to either a temporary storage tank (secondary silo) or a primary pressure screen. The pressure screen is designed to selectively remove certain elements from a pulp feed thereby making the accepted pulp suitable for papermaking [1]. Fibre classification for a pressure screen is probabilistic, based on both fibre size and flexibility. Fibres that don't pass through the screen plate are rejected and sent to

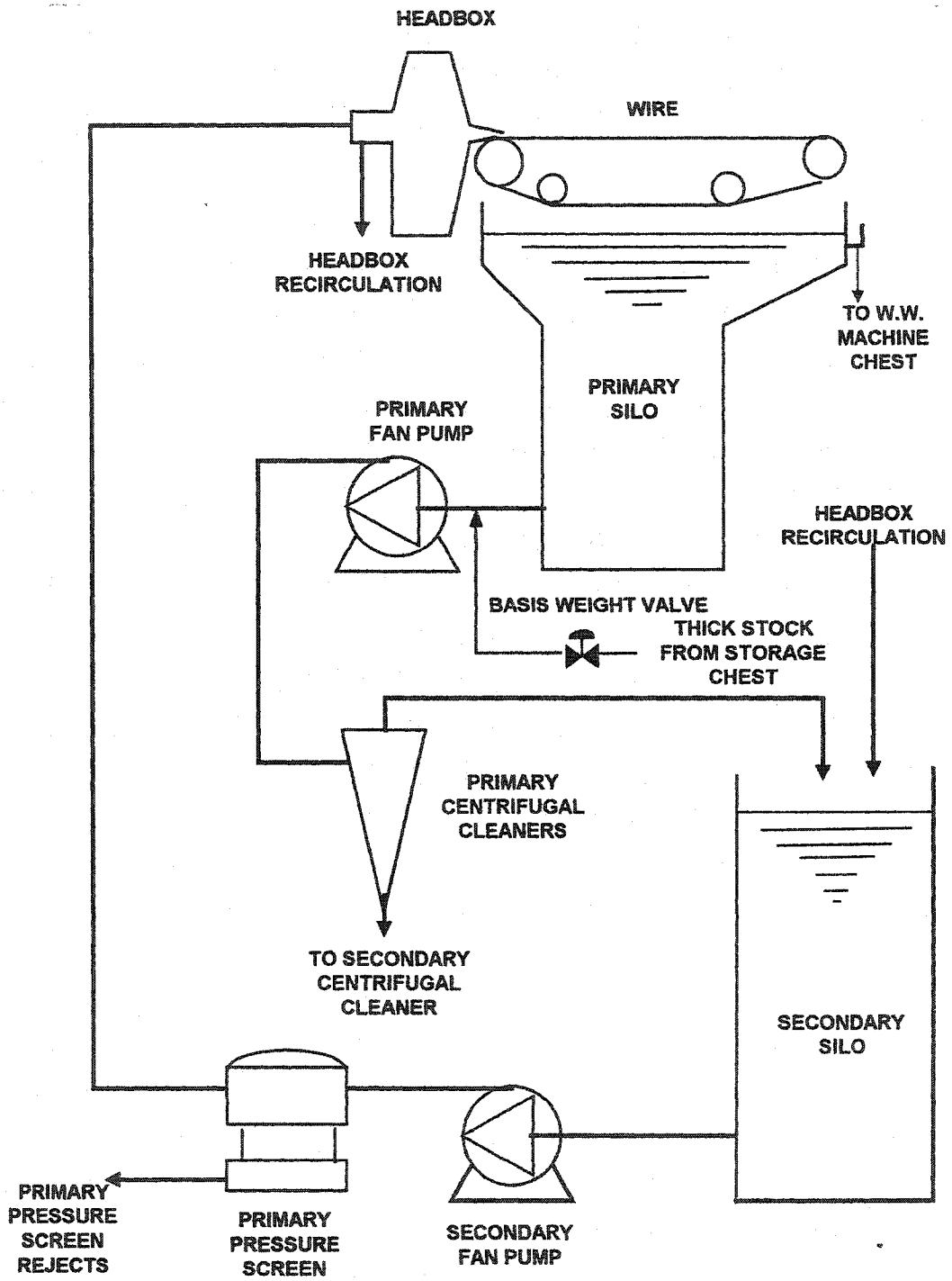

Figure 1: Typical Headbox Approach System

additional pressure screens for further classification. Figure 3 depicts a typical pressure screen labelled with the feed, "accepts" and "rejects" flow. With respect to the dynamic models, the pressure screen will appear as a resistive element that creates a corresponding pressure difference (ΔP) from the feed to the "accepts" stream. A second fan pump is used to transport stock from the secondary silo to the headbox (Figure 1). This fan pump provides both the driving force for stock to pass through the pressure screen and the total head requirements at the headbox slice. The headbox forms part of the Fourdrinier paper machine, which also consists of the following sections: forming section, press section, dryer section and paper accumulator (reel).

The accepted pulp stock from the pressure screen proceeds to the tapered distributor where stock flow is changed from a circular to a rectangular cross-sectional area. The stock continues to the headbox, which is used to discharge the stock as a uniform jet of pulp onto an endless, continuously moving fabric. A fibre mat is formed as water is removed on the Fourdrinier table by suction forces generated by inverted airfoils located beneath the forming fabric. Sufficient water is expelled on the forming table so that the wet sheet can be removed and carried on an endless, continuously moving felt fabric through a press section for further water removal. Final drying of the paper is accomplished in a dryer section where the paper comes into contact with the outside of steam-filled cylinders. To improve the surface properties of the paper, it is passed through a calendar stack. The paper is then accumulated on a reel and sent to storage. The end grade and use of the paper product determines the specifications required for each section contained in the basic Fourdrinier Paper Machine shown in Figure 4.

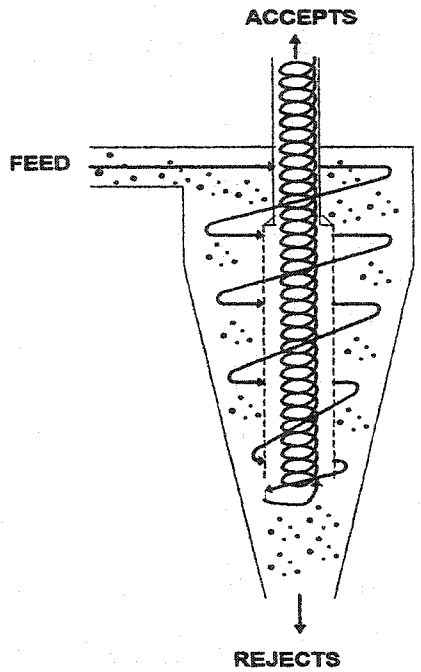

Figure 2: Centrifugal Cleaner

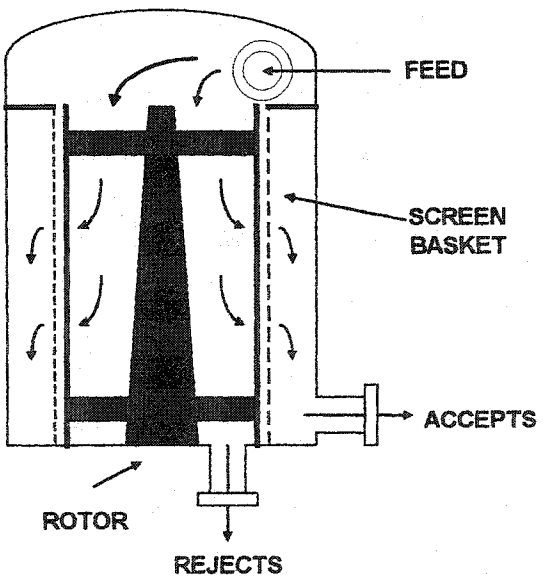

Figure 3: Pressure Screen

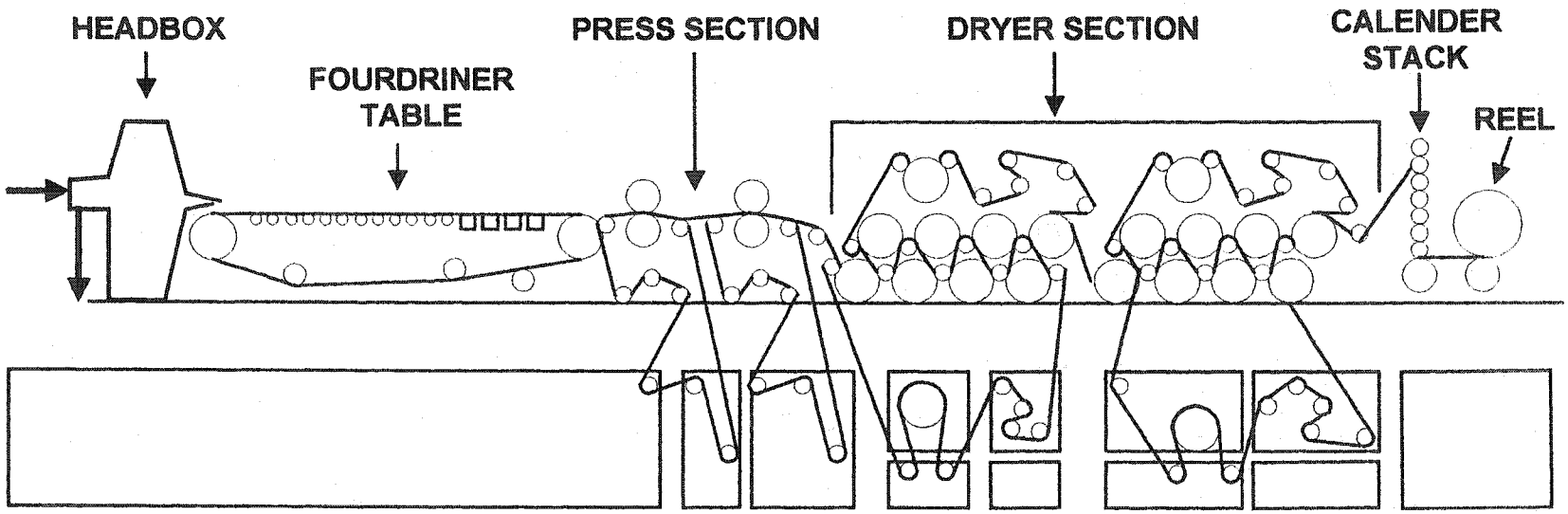

Figure 4: Fourdrinier Paper Machine

1.2 The Functions of a Headbox

The headbox functions to transform the pipeline flow into an even rectangular discharge equal in width and at the same velocity as the paper machine forming fabric. The strength properties in both the machine direction (MD) and cross direction (CD) of the formed paper are a direct result of the design and proper operation of the headbox. Consequently in order to address the issues of paper quality, the design of the headbox has to fulfill the following objectives [3]:

1. The headbox has to generate sufficient internal micro-turbulence to keep the fibres well dispersed prior to being deposited on the forming fabric.
2. The headbox has to provide damping to variations in the velocity profile of the emerging jet in the machine direction.
3. The headbox has to ensure that the transition of stock from headbox to the moving Fourdrinier forming fabric (wire) is smooth and that the angle that the jet impinges on the fabric is correct to provide the best fibre formation possible.

1.3 Headbox Classifications

Headboxes can be subdivided into two general categories: open or pressurized (closed). The open headbox shown in Figure 5 appeared in approximately 1803. It was the earliest known means of providing a jet of stock to a moving fabric to produce paper in a continuous fashion. From Bernoulli's equation shown below, the jet velocity that can be obtained for the open headbox depends on the square root of the level of stock that is present.

$$V = \sqrt{2gh} \tag{1}$$

Where V is the emerging stock jet velocity (m/s), g refers to the gravitational acceleration constant (9.81 m/s^2) and h is the stock level in the headbox (m).

To improve paper quality and increased production speeds, the open headbox was converted to a pressurized headbox. As a result a small-pressurized headbox could achieve the same total head requirements as a much larger open headbox.

Over the years, two distinct styles of pressurized headbox were developed: the air-cushioned headbox and the hydraulic headbox. The air-cushioned headbox can further be classified as having the following distinct features:

1. internal pond ("traditional headbox")
2. internal overflow weir ("weir headbox")

Illustrations of the hydraulic, traditional and weir headboxes shown with simple PI controllers discussed in this thesis are presented in Figures 6-8 respectively. By comparing Figure 6 with that of Figures 7 and 8, the greatest distinction is that the hydraulic headbox does not have an integrated air pad above the stock level. Compared to the air-cushioned headbox, the hydraulic headbox is relatively small and simple in design. For the hydraulic headbox the stock discharge velocity is dependent on the pressure head developed entirely by the fan pump. In contrast the stock discharge velocity from the air-cushioned headbox is dependent on both the level of stock (hydrostatic head) and the air pad pressure.

With respect to the control strategy presented in Figures 6-8 the present arrangement implemented in industry is that total head be controlled by varying the applied armature voltage of a variable speed DC motor that is connected to the centrifugal fan pump [2]. From Figure 1 it is the secondary fan pump that we are concerned with since it is responsible for the delivery of stock to the headbox.

With the absence of an air pad, and no stock level to control, the hydraulic headbox only requires one PI controller as is shown in Figure 6. In contrast for the two styles of air-cushioned headboxes (Figures 7,8) the total head at the slice is the summation of the hydrostatic and piezometric head (air pressure above stock is converted into an equivalent height of stock that would create the same pressure). Compressed air is supplied to the air pad through the fixed air supply valve (Figures 7,8). For both headboxes, the stock level is controlled by manipulation of the air bleed valve. As a result two PI controllers are required to control total head and stock level. It should be noted that in the weir headbox it is the stock level after the weir that is controlled. Figure 8 shows a stock discharge line for stock that passes over the weir. The position of this valve is typically fixed and is not used to control the stock level after the weir. Stock level measurement is by a differential pressure (DP) cell that is tapped across the stock level after the weir.

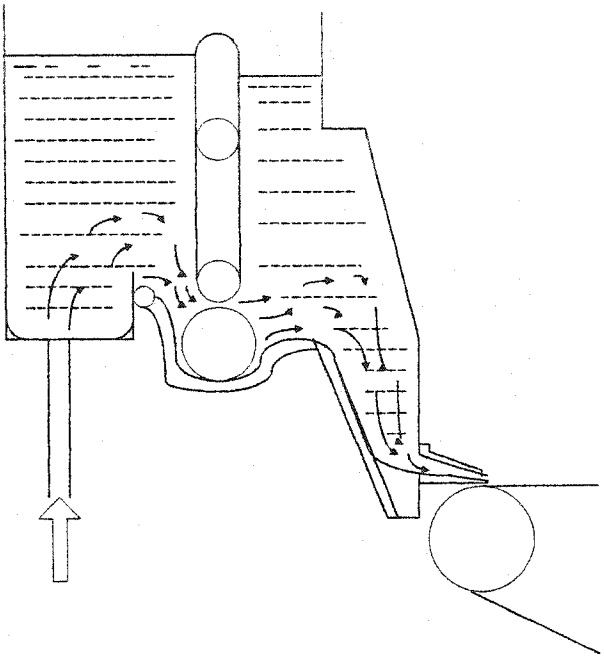

Figure 5: Open Headbox

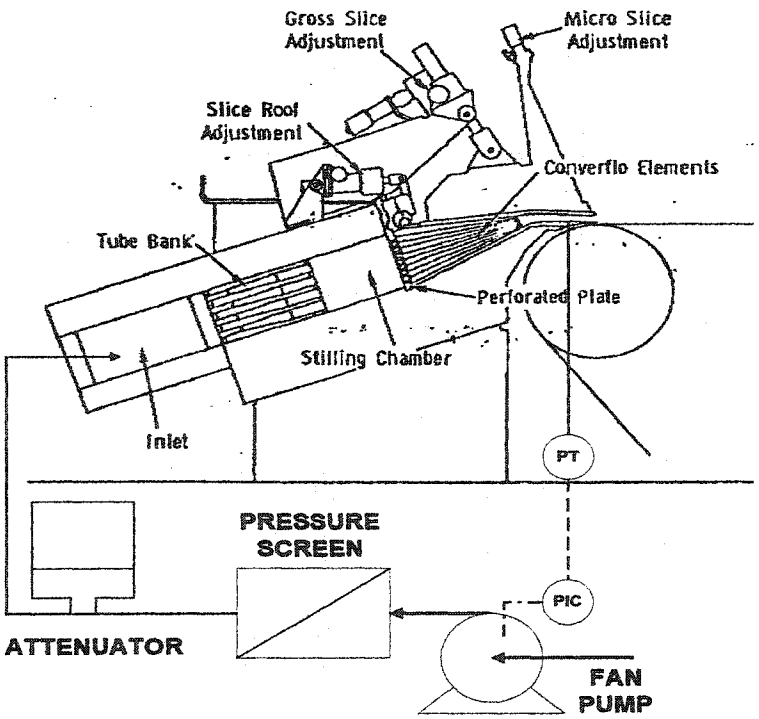

Figure 6: Hydraulic Headbox (Beloit Converflo)

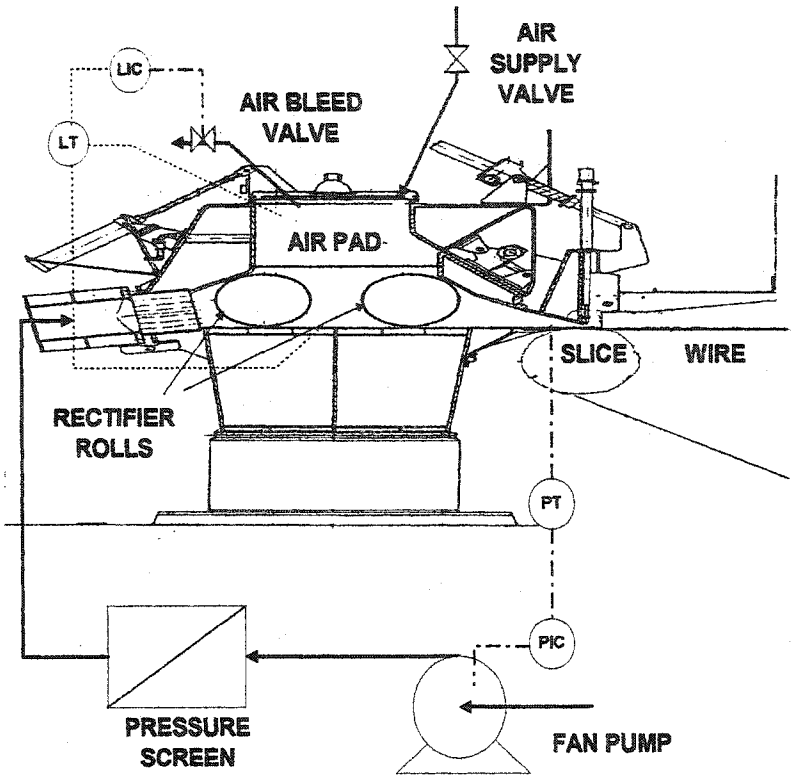

Figure 7: Air-cushioned Traditional Headbox (Valmet)

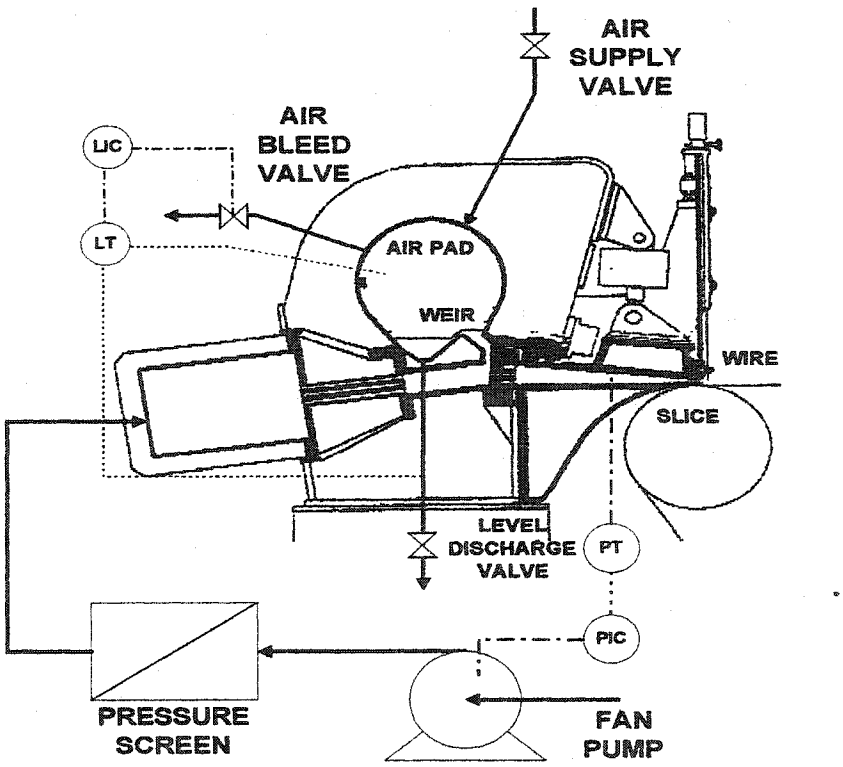

Figure 8: Air-cushioned Weir Headbox (Valmet Sym-Flo)

1.4 The Sections of a Headbox

The operational goal of any headbox is to provide a uniform jet at the slice and to minimize disturbances in both the machine and cross direction. At the same time the headbox must provide adequate internal turbulence to prevent fibres from flocculating. These issues are dealt with the actual design of the headbox. No matter which classification of headbox is used, common design features are present in each. These common sections are listed as follows:

1. distributor (flow spreader)
2. turbulence generator
3. stilling chamber
4. micro-turbulence generator
5. slice channel

Figure 9 illustrates these sections as they appear on the hydraulic headbox. This picture would also pertain to the weir headbox except that above the stilling chamber section appears the integrated air pad and the overflow weir as presented in Figure 8.

The function of the distributor as the name suggest is to distribute stock to the headbox but to also convert the flow from a circular to a rectangular cross-sectional area. Its tapered design with a portion being bypassed enables stock to be withdrawn while at the same time maintain a uniform velocity profile along the width of the headbox. The flow velocities being operated in the headbox determine the amount of taper that is used. In earlier headbox designs this distributor was not tapered and many problems in cross-directional paper quality resulted. This design flaw became more noticeable as production speeds increased. It wasn't until the mid-1950's that Jasper Mardon solved this problem by the introduction of the tapered manifold with stock bypass [3]. Stock is withdrawn from the manifold to the turbulence generator at 90 degrees in order to attenuate any stock line surges that may exist. Although a friction loss (ΔP) will always be present across the distributor, the pressure difference can be cancelled out by changing the stock velocity as per Bernoulli's law. Typical bypass rates of up to 10% are required to cancel the pressure difference across the distributor. The stock that is bypassed through the end of the distributor is piped back to the white-water silo as illustrated in Figure 1.

The turbulence generator section is used to both attenuate pressure pulsations but also to create controlled turbulence to prevent fibres from flocculating. In both the weir and hydraulic

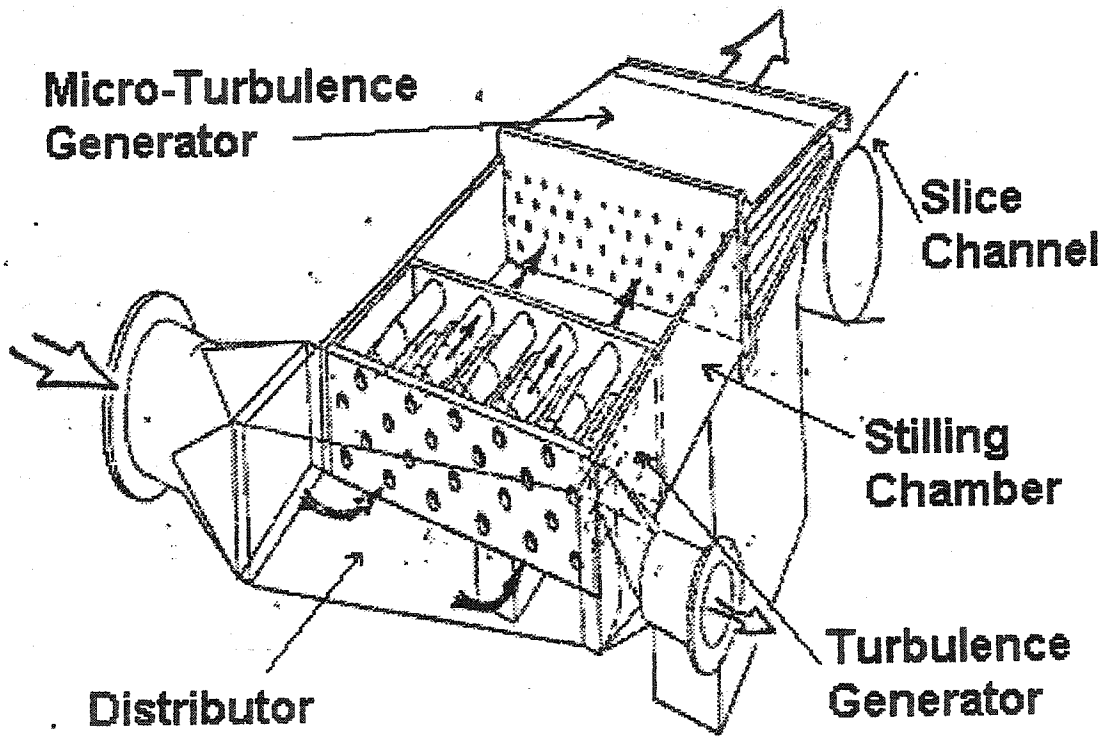

Figure 9: Headbox Sections (Beloit Converflo)

headboxes, a bank of tapered tubes is installed to change the velocity of stock thereby providing the necessary turbulence. The tube bank replaces the older rotating rectifier rolls found in the traditional headbox shown in Figure 7. The reason for the change was that a tube bank offered a lower pressure difference. In addition the chances of the tubes becoming plugged with fibre was essential eliminated, which was a common problem for the holes of a rectifier roll.

The stilling chamber acts as a transition zone that allows additional cross-directional pulp mixing to occur prior to final distribution on the paper machine forming fabric. For the air-cushioned headboxes this section was expanded to include an integrated air pad above the stock. For the traditional headbox the size of this section and volume of stock present are large compared to that found in the weir headbox.

Further turbulence is created in the micro-turbulence generator section. In this section higher intensity turbulence is imposed on the passing stock. In the traditional headbox an additional rotating rectifier roll is used. For the weir headbox a tube bank is implemented in place of the rotating rectifier rolls. In contrast the hydraulic headbox shown in Figures 6 or 9 uses a perforated plate, which then leads to a series of horizontal sheets that provides sufficient fibre distribution.

The final stage is the slice channel, which accelerates the stock to the desired wire speed. The slice channel is also responsible for placing the jet on the wire at the appropriate angle to the forming fabric as to prevent irregular flow patterns or basis weight variations. To accommodate different stock flow rates, the headbox slice is fully adjustable by the manipulation of lifting gear units placed at approximately 1.2 m intervals along the width of the slice [4]. Once in operation small CD jet irregularities can be corrected by the manipulation of manually controlled micrometer-type fine adjustors [4]. Typically the micro-adjustors are coupled with step motors that are computer controlled.

CHAPTER 2

Non-linear Headbox Fundamental Models

2.1 Introduction

Mathematical models pertaining to the approach system of a modern paper machine from the fan pump to three different styles of pressurized headboxes were developed from basic principles. The headbox models that are included relate to the hydraulic, traditional and weir headboxes presented in Figures 6-8. The motivation for developing these models was to compare the dynamics of each headbox as most published literature considers only the traditional headbox. A complete model as presented in this thesis consists of the centrifugal fan pump, variable speed DC motor, pressure screen, attenuator (hydraulic headbox), headbox and the sections of piping that join each of the components in the approach system.

With respect to headbox models that were found in published literature, Nader et. al. developed a non-linear model of a traditional headbox [5]. A model of the weir headbox (Valmet Sym-Flo) derived using first principles was first presented by Lebeau et. al. [6] and then modified by Tuladhar et. al.[7]. Tuladhar et. al. introduced the dynamics created by the presence of the turbulence generator section and flow of stock through the overflow discharge line. The model that was presented consisted of four non-linear differential equations but did not include the presence of the overflow weir. It appears that the stock level set-point this particular paper considered must have been above the height of the weir making the dynamics of this headbox similar to that of the traditional headbox. As a result the overflow weir did not factor into the dynamics of the headbox and therefore behaved like a traditional headbox model. As with the model presented in this thesis, the geometric non-linearity of the integrated air pad was neglected. To date no model for the hydraulic headbox could be found in any published literature. For each of the headbox models discovered in the literature, only the dynamic equations regarding the headbox itself were presented while the other component in the approach system were absent.

The advantage of using the complete approach system model from fan pump to headbox is that through computer simulations the closed loop transient response of each headbox can be studied in detail. A model could then be linearized around different total head operating points to aid in the selection or optimization of controller parameters. Since experimental time on a

working headbox is limited at best, the models that have been validated with experimental data could then be used as a substitute to costly experimental trials.

2.2 Elements of the Approach System Included in the Non-linear Model

To model the approach system of a modern paper machine the following components are required:

1. variable speed DC electric motor/ fan pump combination
2. pressure screen
3. attenuator (hydraulic headbox)
4. air pad (traditional, weir headboxes)
5. piping sections
6. headbox

The piping network from fan pump to headbox as it pertains to the traditional and weir headboxes was illustrated in Figures 7,8. For the hydraulic headbox an in-line attenuator was shown in Figure 6 between the pressure screen and headbox. The attenuator is placed as close as possible to the headbox distributor in order to offer the same stock surge attenuation that is provided by the integrated air pad of the air-cushioned headbox. Mathematical models pertaining to two common styles of attenuators will be provided in later sections of this report.

A consistency model is also included to approximate the head losses that are generated in each of the piping sections because variations in consistency affect head loss through density and viscosity effects.

2.3 Variable Speed DC Motor/ Fan Pump Equations

A crucial piece of equipment in the entire wet end of the paper machine is the centrifugal fan pump. The fan pump not only supplies stock to the headbox but also provides all (hydraulic) or most (air-cushioned) of the total head within the headbox. The total head within the headbox governs the jet velocity and is varied by manipulating the applied armature voltage to the DC motor. A variable speed DC motor is selected since the high torque-to-inertia ratio of this motor gives it a quick response to control signals [8].

A schematic diagram of an armature controlled DC motor / fan pump combination is shown in Figure 10. The DC motor is linked to the fan pump via a speed reducing coupler. The

DC motor electrical circuitry contains a resistive term R_A, an inductance term L_A, and the back electromotive force (back-emf) induced on the armature winding E_B. If the individual voltages around the circuit are summed then the following equation is derived:

$$V_A = V_R + V_L + V_B + V_M \tag{2}$$

Where V_A is the applied armature voltage, V_R is the voltage through the resistor, V_L is the voltage through the inductance, V_B represents the back electromotive force (V) and V_M refers to the armature reaction voltage. The back emf is related to the speed of the pump by the following equation [8]:

$$V_B = K_B W_{PUMP} G_{RATIO} \tag{3}$$

Where K_B refers to the back electromotive force constant (V·s/rad), W_{PUMP} is the pump speed (rad/s), and G_{RATIO} is the ratio of the number of teeth in the pump gear to the number of teeth in the motor gear (dimensionless). Replacing the right-hand side of Equation (2) in terms of pump speed and motor current the following equation results [8]:

$$V_A = R_A I_A + L_A \frac{dI_A}{dt} + K_B W_{PUMP} G_{RATIO} + K_A I_A \tag{4}$$

Where R_A is the armature resistance (ohm), I_A is the armature current (A), L_A is the armature inductance (Henry), and K_A refers to the armature reaction constant (ohm). The last term in Equation (4) (i.e. $K_A I_A$) represents the armature reaction voltage. Due to the size of the DC motor typically found to power the fan pump (i.e. 400 hp +) it is necessary to account for the effect that the armature magnetic force has on the induced back electromotive force in the machine [9]. Rearranging Equation (4) and solving for the derivative of armature current with respect to time yields the following equation:

$$\frac{dI_A}{dt} = \frac{1}{L_A}\left[V_A - R_A I_A - K_B W_{PUMP} G_{RATIO} + K_A I_A\right] \tag{5}$$

The armature current (I_A) applied to the DC motor develops torque (T) as is given by Equation (6) [8].

$$T = K_T I_A G_{RATIO} \tag{6}$$

The term G_{RATIO} is added to recognize that the fan pump is coupled to the DC motor through a speed reduction gearbox.

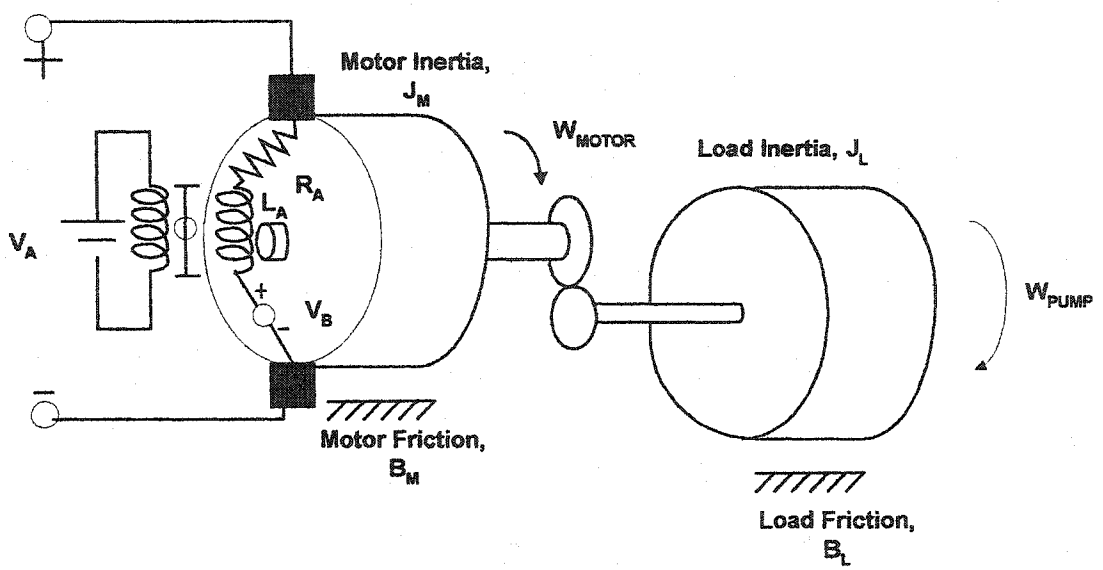

Figure 10: Schematic Diagram of a DC motor / Fan Pump Combination

The total inertial (J_{TOTAL}) multiplied by the derivative of pump speed with respect to time, the total viscous friction (B_{TOTAL}) multiplied by the pump speed, the load torque on the pump (T_{LOAD}) and the torque developed due to the effect that the armature magnetic force has on the back-emf (T_A) sum to give the total torque (T) developed by the DC motor as presented in Equation (7).

$$T = J_{TOTAL}\frac{dW_{PUMP}}{dt} + B_{TOTAL}W_{PUMP} + T_{LOAD} + T_A \tag{7}$$

The term T_A in Equation (7) is defined as follows [8]:

$$T_A = K_A\frac{I_A^{\,2}}{W_{PUMP}} \tag{8}$$

Substituting Equations (6, 8) into Equation (7) and solving for the derivative of pump speed with respect to time yields how a mechanical torque imbalance causes the fan pump speed to change as presented in Equation (9) [8]:

$$\frac{dW_{PUMP}}{dt} = \frac{1}{J_{TOTAL}}\left[K_T I_A G_{RATIO} - B_{TOTAL}W_{PUMP} - T_{LOAD} - K_A\frac{I_A^{\,2}}{W_{PUMP}}\right] \tag{9}$$

Where W_{PUMP} is the pump speed (rad/s), J_{TOTAL} refers to the total inertia of the motor / pump combination (N·m·s^2/rad), B_{TOTAL} is the total viscous friction of the motor / pump combination (N·m·s/rad), T_{LOAD} is the torque of pulp stock on the pump (N·m) and K_T is the motor torque constant (N·m/A).

The total inertia and viscous friction of the motor / pump combination is calculated by the summation of the contributions of the individual components with a correction factor for the step down in gears [8].

$$B_{TOTAL} = B_M + G_{RATIO}^{\,2}B_L \tag{10}$$

$$J_{TOTAL} = J_M + G_{RATIO}^{\,2}J_L \tag{11}$$

Where B_M is the viscous friction of the motor (N·m·s/rad), B_L is the viscous friction of the pump (N·m·s/rad), J_M is the moment of inertia of the motor (N·m·s^2/rad) and J_L refers to the moment of inertia of the pump (N·m·s^2/rad).

The load torque, T_{LOAD} is determined as follows [10]:

$$T_{LOAD} = \frac{\rho g H_{PUMP} Q_{PUMP}}{W_{PUMP}\eta} \tag{12}$$

Where ρ refers to the density of stock (kg/m^3), g represents the gravitational acceleration constant (9.81 m/s^2), H_{PUMP} is the pump head (m), Q_{PUMP} represents the flow from the pump (m^3/s), W_{PUMP} is the speed of the pump (rad/s) and η refers to the pump efficiency (fraction).

Using pump characteristics curves the net head of stock and corresponding efficiency of the fan pump at different operating points (speed, flow) can be calculated. Figure 11 illustrates pump characteristic curves of a centrifugal fan pump supplied by Ahlstrom [11]. This specific pump is referenced since it pertains to a secondary centrifugal pump used at a local paper mill (Cascades Fines Papers Group Thunder Bay Inc.), which supplies stock to a traditional headbox. Equations (13) and (14) can be used to mathematically determine the relationship between head of stock and pump efficiency with respect to different combinations of pump speeds and volumetric flow rates [10,12].

$$H_{PUMP} = aW_{PUMP}^2 + bW_{PUMP}Q_{PUMP} - cQ_{PUMP}^2 + d \tag{13}$$

$$\eta = \frac{\frac{e_1 Q_{PUMP}}{W_{PUMP}} + e_2\left(\frac{Q_{PUMP}}{W_{PUMP}}\right)^2}{100} \tag{14}$$

Using the method of least squares the parameters a, b, c, d, e_1 and e_2 are determined. A summary of these parameters required to generate the pump characteristic curves presented in Figure 11 are found in Table 1.

Coefficient	Value
a ($m \cdot s^2/rad^2$)	5.50×10^{-3}
b ($s^2/(m^2 \cdot rad)$)	5.50×10^{-2}
c (s^2/m^5)	11.3
d (m)	3.8×10^{-2}
e_1 ($\% \cdot rad/m^3$)	14558.0
e_2 ($\% \cdot rad^2/m^6$)	-6.011×10^5

Table 1: Summary of Coefficients Required For Figure 11

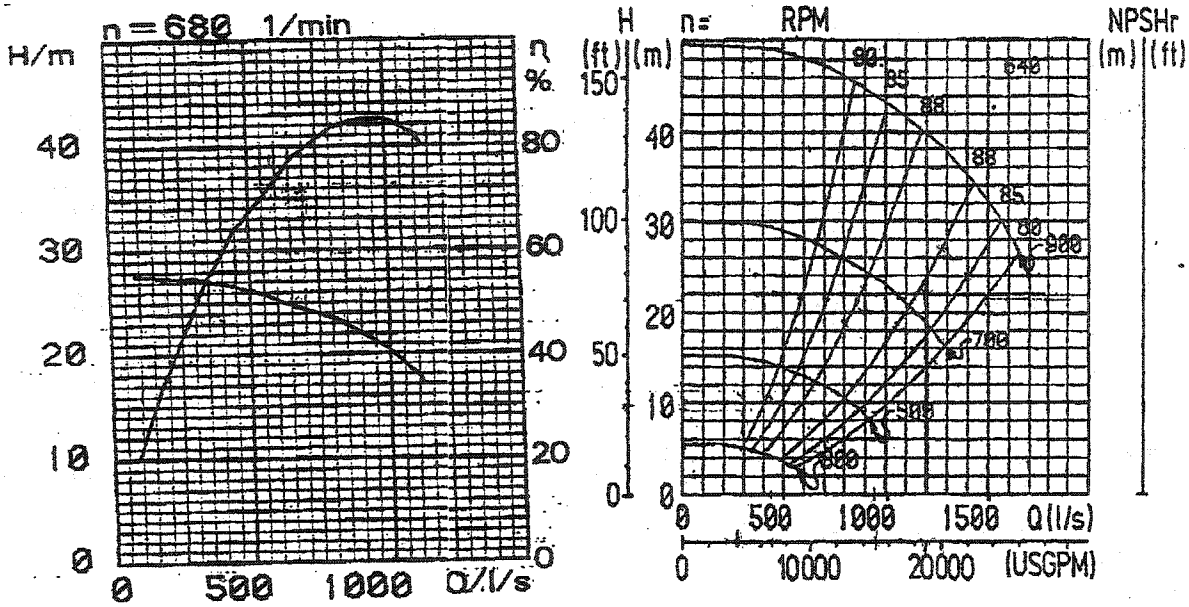

Figure 11: Pump Characteristic Curves for a Centrifugal Fan Pump (Ahlstrom)

2.4 Dynamic Model of a Traditional Headbox and Approach System

A schematic diagram of the piping network from the fan pump to the traditional headbox was illustrated in Figure 7. The flow of stock to the headbox distributor, Q_{INT} is the difference between the flow of stock into the primary pressure screen, Q_{PUMP} and the flow rejected by the screens, Q_{REJECT}. With Q_{REJECT} expressed as a ratio of the flow rate from the pump, Q_{INT} is given as:

$$Q_{INT} = Q_{PUMP} - Q_{REJECTS} = Q_{PUMP}(1 - R_R) \tag{15}$$

Where R_R refers to the reject ratio of the pressure screen (fraction). Q_{INT}, Q_{PUMP} and $Q_{REJECTS}$ have units of m^3/s. The change in flow from the fan pump can be derived from a force balance around the control volume from fan pump to headbox slice opening as is shown in Equation (16).

$$\frac{dQ_{PUMP}}{dt} = g\left[\frac{A}{L}\right]\left[H_{PUMP} - H_{STATIC} - H_{LIP} - f_1 Q_{INT}^{\ 2}\right] \tag{16}$$

Where A/L refers to the effective area/length ratio of the control volume (m), g is the gravitational acceleration constant (9.81 m/s^2), H_{PUMP} is the total head generated by the fan pump (m), H_{STATIC} represents the difference in elevation between the headbox and fan pump (m), H_{LIP} is the total head at the slice (m), f_1 is the head loss coefficient (s^2/m^5), and Q_{INT} refers to the

"accepts" flow from the primary pressure screen (m^3/s). The complete derivation of Equation (16) is found in Appendix A.1.

The actual flow that enters the headbox, $Q_{HEADBOX}$ is the difference between Q_{INT} and the flow which is re-circulated to the white-water silo, $Q_{RECIRCULATION}$ that is required to maintain a negligible pressure difference across the distributor (Equation (17)).

$$Q_{HEADBOX} = Q_{INT} - Q_{RECIRCULATION} \tag{17}$$

The stock that is re-circulated is determined as follows:

$$Q_{RECIRCULATION} = Q_{INT} R_{RECIRCULATION} \tag{18}$$

Where $R_{RECIRCULATION}$ represents the fraction of the flow of stock into the distributor that is re-circulated back into the white-water silo. Using Bernoulli's equation the flow of stock through the headbox slice opening, Q_{LIP} is given as:

$$Q_{LIP} = A_{LIP}\alpha\sqrt{\frac{2P_{LIP}}{\rho}} \tag{19}$$

Where Q_{LIP}, A_{LIP}, α, P_{LIP} and ρ represent the volumetric flow of stock through the slice (m^3/s), the open area of the headbox slice (m^2), the discharge coefficient of the slice channel, the total pressure at slice (Pa) and the density of stock (kg/m^3) respectively.

The total pressure at the slice, P_{LIP} is the summation of the air pressure in the air pad and the hydrostatic head due to the presence of stock above the slice as is shown in Equation (20).

$$P_{LIP} = P_{AIRPAD} + \rho g L_{STOCK} \tag{20}$$

Where P_{AIRPAD} refers to the air pressure in the air pad (Pa) and L_{STOCK} represents the level of stock above the slice opening (m). The rate of change of the stock level with respect to time is dependent on the flow of stock in and out of the headbox as is presented in Equation (21).

$$\frac{dL_{STOCK}}{dt} = \frac{Q_{HEADBOX} - Q_{LIP}}{A_{HEADBOX}} \tag{21}$$

Where $Q_{HEADBOX}$ refers to the flow of stock into the headbox (m^3/s), Q_{LIP} represents the flow of stock out through the slice channel (m^3/s) and $A_{HEADBOX}$ refers to the cross sectional area of the headbox (m^2). As the stock level varies, the air pad volume above the stock also changes. The differential equation that relates changes in air pad volume to changes in stock level is stated as:

$$\frac{dV_{AIRPAD}}{dt} = -A_{HEADBOX}\frac{dL_{STOCK}}{dt} \tag{22}$$

Where V_{AIRPAD} represents the volume of the air pad (m^3). In the air-cushioned headbox, air pressure within the air pad is regulated by an air supply and air discharge line. The ideal gas law is used to determine the change in the number of moles of air in this air pad, as defined by Equation (23).

$$\frac{dN_{AIRPAD}}{dt} = \frac{(P_{AIRPAD} + P_{ATM})[Q_{AIR_{IN}} - Q_{AIR_{OUT}}]}{RT_{AIRPAD}} \quad (23)$$

Where N_{AIRPAD} represents the moles of air in the air pad at any time t, (kg mole), P_{AIRPAD} is the air pressure in the air pad (Pa), P_{ATM} is the atmospheric pressure (Pa) and R is the universal gas constant (8314 m^3 Pa/kg mole·K), T_{AIRPAD} is the average absolute temperature of air in the air pad (K) and $Q_{AIR,IN}$, $Q_{AIR,OUT}$ represents the flow of air in and out of the air pad (m^3/s) respectively. The airflow through the air supply ($Q_{AIR,IN}$) and air discharge ($Q_{AIR,OUT}$) valves can be determined using the Universal Gas Sizing Equation by Fisher [13]. The equation as it appears in the reference paper with the appropriate conversion to S.I. units is shown in Equation (24).

$$Q_{AIR} = 7.87\text{x}10^{-6}\sqrt{\frac{520}{G_{AIR}T_{AIRPAD}}}C_g P_1 \sin\left[\frac{3417}{C_1}\sqrt{\frac{\Delta P}{P_1}}\right]_{DEG} \quad (24)$$

Where Q_{AIR} is the flow of air in or out of the air pad (m^3/s), G_{AIR} refers to the specific gravity of air (for air = 1.0), C_g is the gas sizing coefficient, P_1 is the inlet pressure to the valve (psia), ΔP is the pressure difference across each valve (psia), C_V refers to the liquid sizing coefficient and C_1 represents the quotient C_g/C_V. The constant $7.87\text{x}10^{-6}$ is used to convert from units of ft^3/hr to m^3/s. The term C_g is used to predict the flow through a valve based on its physical size or flow area. C_1 is a numerical indicator of the recovery capabilities of the valve. The typical range of possible values of C_1 is 16-37 [13]. The sine function is used to predict critical flow. The only stipulation for using this equation is that the sine angle is limited from 0 to 90 degrees since any larger angle would incorrectly indicate a reduction in flow.

Using the ideal gas law, the rate of change of pressure with respect to time in the air pad (assuming $\Delta T_{AIRPAD} \approx 0$) is determined as follows:

$$\frac{dP_{AIRPAD}}{dt} = \frac{RT_{AIRPAD}}{V_{AIRPAD}}\frac{dN_{AIRPAD}}{dt} - \frac{(P_{AIRPAD} + P_{ATM})}{V_{AIRPAD}}\frac{dV_{AIRPAD}}{dt} \quad (25)$$

A change in air pressure can be attributed to a change in the net flow of air in or out of the air pad or as a result of a change in the air pad volume.

2.5 Dynamic Model of a Weir Headbox and Approach System

The weir headbox is unique in that the attenuator element is placed directly above the equalization chamber as illustrated in Figure 8. The attenuator element is placed as close to the slice as possible to minimize the effect of any pressure pulsations that may arise [4]. Micro-turbulence is created by the presence of a perforated plate after the equalization chamber. This prevents fibre flocculation, thereby providing better sheet formation but also adds to the flow resistance within the headbox. The resistance created by the presence of the perforated plates was factored into Equation (16) by the term f_1.

In 1981 improvements were made to the design of the weir headbox to accommodate a wider range of paper grades and production rates. As a result of the changes, the headbox could now handle paper basis weights of 30 – 120 g/m^2 and achieve a maximum speed of 1400 m/min (4620 FPM) [4].

The approach system for the weir headbox presented in Figure 8 is identical to that of the traditional headbox shown in Figure 7. As a result the flow equations (Equations (15-19)) of the previous section also apply to the weir headbox. Some changes are required due to the presence of an overflow weir. Consequently the total pressure at the slice, P_{LIP} is the summation of the air pressure in the air pad, P_{AIRPAD} and the hydrostatic head created by the presence of stock on the approach side of the weir, L_{EQUAL}.

$$P_{LIP} = P_{AIRPAD} + \rho g L_{EQUAL} \tag{26}$$

The change in stock level before the weir is determined as follows:

$$\frac{dL_{EQUAL}}{dt} = \frac{\left[Q_{HEADBOX} - Q_{LIP} - Q_{WEIR}\right]}{A_{EQUAL}} \tag{27}$$

Where A_{EQUAL} is the cross-sectional area of the headbox above the weir (m^2) and Q_{WEIR} refers to the volumetric flow of stock over the weir (m^3/s). The volumetric flow of stock over a rectangular weir, Q_{WEIR} can be estimated using the modified Francis weir formula as stated in Equation (28) [14]. This equation only applies if $L_{EQUAL} > L_{WEIR}$, else Q_{WEIR} is equal to zero.

$$Q_{WEIR} = 0.415\left[W_{HBX} - 0.2\left[L_{EQUAL} - L_{WEIR}\right]\right]\left[L_{EQUAL} - L_{WEIR}\right]^{1.5}\sqrt{2g} \tag{28}$$

Where W_{HBX} is the width of the headbox (m) and L_{WEIR} refers to the height of the weir (m). The flow of stock that goes over the weir is typically no more than 5% of the flow entering the headbox. The excess stock that flows over the weir is discharged through a pipe located at the base of the headbox. A manual valve restricts the flow through this pipe, but it (percent opening) is not varied during normal operation. The flow through this valve, $Q_{DISHARGE}$ can be determined using the Fisher valve sizing equation for liquids (S.I. units) [13].

$$Q_{DISCHARGE} = 7.52x10^{-5} C_V \sqrt{H_{TOTAL}} \tag{29}$$

Where $Q_{DISCHARGE}$ is the flow through the headbox discharge valve (m^3/s), C_V refers to the valve discharge coefficient ($USGPM/psi^{1/2}$), H_{TOTAL} represents the total head at the valve opening (m) and the constant $7.52x10^{-5}$ is a conversion factor. The derivation of Equation (29) is provided in Appendix A.2. The total head (H_{TOTAL}) is the summation of the piezometric and the hydrostatic head that is given as:

$$H_{TOTAL} = L_{STOCK} + H_{S2} + \frac{P_{AIRPAD}}{\rho g} \tag{30}$$

Where H_{S2} is the elevation difference between the bottom of the headbox and the discharge valve (m) and L_{STOCK} refers to the level of stock after the weir (m). The rate of change of the stock level over time after the weir is determined by the difference between stock that goes over the weir and stock that exits via the discharge line.

$$\frac{dL_{STOCK}}{dt} = \frac{[Q_{WEIR} - Q_{DISCHARGE}]}{A_{HEADBOX}} \tag{31}$$

Where $A_{HEADBOX}$ represents the cross-sectional area of the headbox after the weir (m).

The change in air pressure above the stock is similar to the traditional headbox except for a slight modification that is required as a result of two independent stock levels before and after the weir. Therefore the change in air pad volume is given as:

$$\frac{dV_{AIRPAD}}{dt} = -A_{EQUAL}\frac{dL_{EQUAL}}{dt} - A_{HEADBOX}\frac{dL_{STOCK}}{dt} \tag{32}$$

The rate of change in the number of moles of air in the air pad, the flow of air through the air supply / air discharge line and the rate of change in air pad pressure over time can be calculated using Equations (23-25).

2.6 Dynamic Model of a Hydraulic Headbox and Approach System

A typical piping diagram of a hydraulic headbox was presented in Figure 6. The hydraulic headbox was designed to replace the traditional headbox, where the objective was to eliminate the presence of the large pond and rectifier rolls. A replacement for the rectifier rolls that would create a high scale of micro-turbulence while not plugging with fibres was required as part of the new headbox design. The preliminary replacement was fine mesh screens but this was found to rapidly plug with fibres [15]. As a result horizontal converging plates known as Converflo Sheets were installed. The length and spacing of these sheets differ for each headbox but the important design criteria is that the wake generated by the sheets produces very fine scale turbulence [15]. The design of the hydraulic headbox also enables higher stock consistencies implying a reduction in the white-water drainage required on the forming section [15].

The hydraulic headbox has proven in operation to provide excellent sheet formation provided that an external attenuator is installed prior to the headbox distributor to dampen out stock surges [16]. Figure 12 illustrates different styles of attenuators that are in use today [17]. As a result of the presence of the attenuator, two control volumes are created in the stock approach system to the headbox. Control volume *1* refers to the piping section from the fan pump to the base of the attenuator. Control volume *2* refers to the piping section from the base of the attenuator to the base of the headbox. The "accepts" or internal flow, Q_{INT} is calculated using Equation (15).

The rate of change of flow from the fan pump, Q_{PUMP} presented in Equation (33) can be derived in a similar fashion to Equation (16) (Appendix A.1) except that the force balance is around control volume *1* as outlined previously.

$$\frac{dQ_{PUMP}}{dt} = g\left(\frac{A}{L}\right)_1 \left[H_{PUMP} - H_{INT} - H_{S2} - f_1 Q_{INT}^{\ 2}\right] \tag{33}$$

Where H_{INT} is the head of stock at the base of the attenuator (m), H_{S2} refers to the elevation difference between the fan pump and the attenuator (m), f_1 represents the head loss coefficient (s^2/m^5) for control volume *1*, and $(A/L)_1$ refers to the effective area to length ratio of control volume *1*. From a force balance around control volume *2*, the rate of change of flow through the slice, Q_{LIP} can be determined using Equation (34).

$$\frac{dQ_{LIP}}{dt} = g\left(\frac{A}{L}\right)_2 \left[H_{INT} - H_{LIP} - f_2 Q_{LIP}^{\ 2}\right] \tag{34}$$

Where $(A/L)_2$ is the effective area to length ratio of control volume 2 (m), f_2 refers to the head loss coefficient for control volume 2 (s^2/m^5) and H_{LIP} represents the head of stock at the slice (m). Since Q_{LIP} is not easily measured, Equation (34) is expressed in terms of a change in head of stock rather than a change in flow. The rate of change of the head of stock with respect to time can be determined using Equation (35). A complete derivation of Equation (35) is found in Appendix A.3.

$$\frac{dH_{LIP}}{dt} = \frac{\sqrt{2gH_{LIP}}}{A_{LIP}\alpha}\left(\frac{A}{L}\right)_2\left[H_{INT} - H_{LIP} - 2gf_2H_{LIP}\left(A_{LIP}\alpha\right)^2\right] \tag{35}$$

Where A_{LIP} refers to the headbox slice opening area (m^2) and α is the discharge coefficient of the slice channel (dimensionless).

The remaining differential equations will depend on the type of attenuator used. Since in this thesis report a surge tank attenuator was used in simulations that are to follow, the equations that pertain to this type of attenuator are considered in the next section. Equations were also developed for the air chamber attenuator shown in Figure (12) but since this was not included in any simulations, it is presented separately in Appendix B.

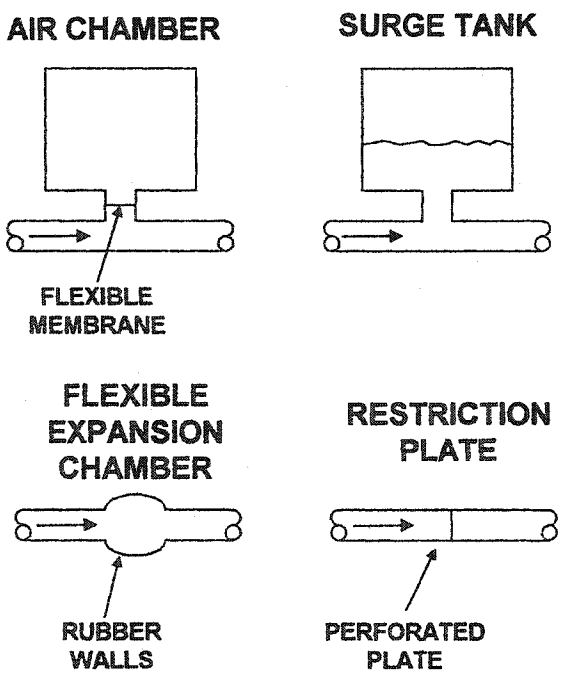

Figure 12: Different Styles of Attenuators

2.7 Model of a Surge Tank Attenuator

A surge tank attenuator is shown in Figure 13. It should be noted that there is no solid membrane separating the air / stock interface. In addition the air pressure built up inside the vessel is self-regulating with no air supply or air exhaust line. To model the gas portion of the attenuator, it is assumed that the following adiabatic gas law is obeyed [18].

$$PV^N = K_{ATT} \tag{36}$$

Where K_{ATT} refers to the attenuator gas constant (Pa $(m^3)^N$), P is the absolute pressure of gas in the attenuator (Pa), N is the polytrophic exponent (1.2 for air) and V represents the gas volume that is present (m^3).

The attenuator gas constant, K_{ATT} can be calculated by knowing that the pressure in the attenuator is atmospheric when there is no stock inside the attenuator. As the attenuator fills with stock, a constant mass of air is trapped and the pressure varies as the stock height changes. Equation (36) is modified to reflect the actual dimensions of the attenuator and to express the pressure in terms of gauge rather than absolute as presented in Equation (37).

$$\left[P_{ATT} + P_{ATM}\right]\left[A_{ATT} Level_{GAS}\right]^N = K_{ATT} \tag{37}$$

Where P_{ATT} refers to the gauge air pressure (Pa), P_{ATM} is the atmospheric pressure (Pa), A_{ATT} is the cross-sectional area of the attenuator (m^2) and $Level_{GAS}$ represents the gas level in the attenuator (m). Equation (37) is then rearranging to yield Equation (38) that relates how the height of gas in the attenuator varies with pressure.

$$Level_{GAS} = \left[\frac{1}{A_{ATT}}\right]\left[\frac{K_{ATT}}{P_{ATT} + P_{ATM}}\right]^{\frac{1}{N}} \tag{38}$$

The rate of change of the air pressure inside the attenuator can then be determined by taking the derivative of pressure with respect to time in Equation (38). In addition the rate of change of the gas level is determined by the rate of change of stock level in the attenuator. A complete derivation of Equation (39) that relates how the stock level and air pressure in the attenuator are related is presented in Appendix A.4.

$$\frac{dP_{ATT}}{dt} = \left[\frac{Q_{INT} - Q_{RECIRCULATION} - Q_{LIP}}{A_{ATT}}\right]\left[\frac{NK_{ATT}}{Level_{GAS}^{N+1} A_{ATT}^{N}}\right] \tag{39}$$

The head of stock at the base of the attenuator, H_{INT} can then be determined by the summation of the gas pressure and the hydrostatic pressure within the attenuator.

$$H_{INT} = \frac{P_{ATT}}{\rho g} + \left(H_{ATT} - Level_{GAS}\right) \pm H_{ORIFICE} \tag{40}$$

Where H_{ATT} represents the height of the attenuator (m), H_{INT} is the total head of stock inside the attenuator (m), and $H_{ORIFICE}$ refers to the head loss through the attenuator orifice plate (m). The equivalent head loss created by the presence of the attenuator could be modeled as an orifice plate that can be derived using Bernoulli's equation [19].

$$\left|H_{ORIFICE}\right| = \frac{1}{2g}\left[1 - \left[\frac{A_0}{A_1}\right]^2\right]\left[\frac{Q_{INT} - Q_{RECIRCULATION} - Q_{LIP}}{C_D A_0}\right]^2 \tag{41}$$

Where A_0, A_1 and C_D represents the total area of the holes in the orifice plate (m^2), the cross-sectional area of the pipe section into the attenuator (m^2) and the discharge coefficient of the attenuator orifice plate respectively. The sign of $H_{ORIFICE}$ is determined by the direction of flow through the orifice plate.

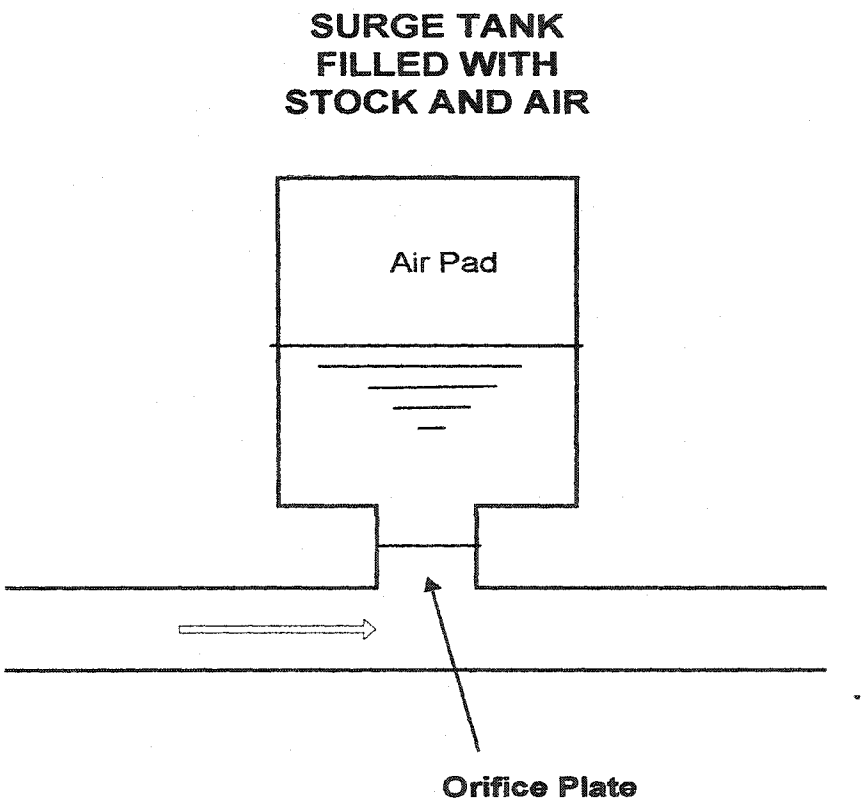

Figure 13: Surge Tank Attenuator

2.8 Stock Consistency Model

The rate of change of consistency over time could be determined using the analogy of a continuous stir tank reactor (CSTR). In a CSTR it is assumed that the contents of the tank are well mixed and that the volumetric flow rates in and out are constant. In the case of the headbox, the piping section from the fan pump to the pressure screen (Vol_1), the pressure screen (Vol_2), and the pressure screen to and including the headbox (Vol_3), are considered to be individual control volumes. For the three control volumes listed, a mass balance around each section determines the accumulation of fibre. The rate of change of the stock consistency over time in Vol_1 is given as:

$$\frac{dC1}{dt} = \frac{Q_{PUMP}(C0 - C1)}{Vol_1} \tag{42}$$

Where $C0$ and $C1$ represent the consistency of stock entering the fan pump and entering the pressure screen (%) respectively. Vol_1 refers to the control volume from the fan pump to the pressure screen (m^3). In a similar manner the change in stock consistency exiting the "accepts" stream of the pressure screen, $C2$ is determined. The flow of stock exiting via the pressure screen "rejects" stream is calculated as a fraction of the flow into the pressure screen (i.e. Q_{PUMP} x reject ratio). The consistency of the "rejects" stream is the product of the fibre distribution coefficient, R_C and the consistency of the feed stream, $C1$. R_R refers to the reject ratio, which represents the portion of stock that is removed via the "rejects" stream of the pressure screen.

$$\frac{dC2}{dt} = \frac{Q_{PUMP}C1 - Q_{PUMP}R_R R_C C1 - Q_{INT}C2}{Vol_2} \tag{43}$$

The change in consistency from the "accepts" stream of the pressure screen to the headbox slice is determined as follows:

$$\frac{dC3}{dt} = \frac{Q_{INT}(C2 - C3)}{Vol_3} \tag{44}$$

Where $C3$ refers to the consistency of stock exiting the headbox slice (%) and Vol_3 represents the control volume from the pressure screen "accepts" stream to the headbox slice (m^3).

Using the average stock consistency around each control volume, the average viscosity of stock can be determined using the following equation [20]:

$$\mu_{AVG} = 0.0015 C_{AVG}^{3.1} \tag{45}$$

Where C_{AVG} and μ_{AVG} represent the average consistency (%) and average viscosity (Pa s) of the stock around each control volume respectively. The empirical relationship given in Equation (45) was developed for semi-bleached kraft (SBK) pulp at a temperature of 20 °C, and a consistency range of 1 to 12.6%. Since the consistency range is well above the normal operating conditions (0.5 – 0.7%) extrapolation is required. The exponential curve generated by Equation (45) is extended to 0% (pure water). A third order polynomial equation is then used to predict the viscosity of stock from 0% to 12% as is presented below.

$$\mu_{AVG} = 2.1\text{x}10^{-3}\ C_{AVG}^{\ 3} - 2.6\text{x}10^{-3}\ C_{AVG}^{\ 2} + 3.7\text{x}10^{-3}\ C_{AVG} + 1.005x10^{-3} \quad (46)$$

The effect of temperature on viscosity can be approximated using Andrade's equation, which is given as [21]:

$$\mu = E\exp\left(\frac{F}{T}\right) \quad (47)$$

Where T is the absolute temperature (Kelvin), E and F are constants for Andrade's Equation and μ refers to the stock viscosity (Pa·s). It is assumed that the effect of temperature changes on stock viscosity follows the same trend as that of pure water. Using data available on pure water, the constants E and F from Equation (47) are determined as $1.805\text{x}10^{-6}$ and 1856.7 respectively. Assuming that a change in stock viscosity is the same as a change in viscosity of water for a given temperature change then the stock viscosity corrected for temperature variations is given as:

$$\mu_{AVG,C} = \mu_{AVG,20} - 1.805x10^{-6}\left[\exp\left[\frac{1856.7}{293}\right] - \exp\left[\frac{1856.7}{T}\right]\right] \quad (48)$$

Where $\mu_{AVG,C}$ and $\mu_{AVG,20}$ refers to the average stock viscosity (Pa·s) at temperature T and at the reference temperature respectively. The stock viscosity is used to calculate the Reynolds number that is used to calculate the friction factor obtained by either the Moody Chart or the Colebrook Equation [21]. Once the friction factor is known then major and minor head losses from the fan pump to the headbox can be approximated using Darcy's equation [21].

CHAPTER 3

Headbox Simulations

3.1 Introduction

Simulations pertaining to the hydraulic, traditional and weir headboxes were performed at total head operating points of 60, 75 and 90 kPa. This translates to jet velocities of approximately 640, 716, and 792 m/min respectively. Through computer simulations the operating characteristics of each headbox are revealed. A summary of the model parameters referenced in Equations (2-48) is found in Table 2. Descriptions of the variables listed in Table 2 are located in the nomenclature section at the back of the thesis.

Borland C++ source code was created to simulate each headbox model. A fixed-step, fourth-order Runge-Kutta integration algorithm with an integration time step of 0.02 seconds was selected to evaluate the values of the state variables at each time step. It was determined that the solutions to the differential equations would agree up to a maximum integration time step of 0.1 seconds. A summary of the state (x), input (u), and output (y) variables required for each headbox model in vector notation (^{T} denotes transpose) are given as follows:

hydraulic headbox: $x = [H_{LIP}, P_{ATT}, Q_{PUMP}, W_{PUMP}, I_A, C1, C2, C3]^T$

$$u = [V_A]$$

$$y = [P_{LIP}]$$

traditional headbox: $x = [L_{STOCK}, P_{AIRPAD}, Q_{PUMP}, W_{PUMP}, I_A, C1, C2, C3]^T$

$$u = [Cg, V_A]^T$$

$$y = [L_{STOCK}, P_{LIP}]^T$$

weir headbox: $x = [L_{EQUAL}, P_{AIRPAD}, L_{STOCK}, Q_{PUMP}, W_{PUMP}, I_A, C1, C2, C3]^T$

$$u = [Cg, V_A]^T$$

$$y = [L_{STOCK}, P_{LIP}]^T$$

The output behaviour of each headbox variable to a sinusoidal input will be presented by frequency responses. The frequency response is evaluated by determining the magnitude and angle of the complex number formed by substituting $s = jw$ into a transfer function. A transfer function between an input-output pairing is calculated by taking the ratio of the Laplace transform of the output variable to the Laplace transform of the input variable of the linearized model. A commercially available software program named EASY5™ developed by *The Boeing*

Company was utilized to generate frequency response plots directly from the differential equations of each headbox model. The C++ source code was linked to EASY5™ via a user defined Fortran module available in the EASY5™ environment.

EASY5™ is best described as a "graphical user based software program used to model, analysis, and design dynamic systems characterized by differential, difference and algebraic equations" [22]. Similar to the Simulink environment from MATLAB™, EASY5™ uses functional blocks to build-up systems of equations. In addition an assortments of analysis tools are available to perform non-linear simulations, generate frequency response plots and state-space models [22]. The future use of the frequency responses generated by EASY5™ is to validate the headbox models by comparing model and experimental data by the time-invariant frequency response.

The analog PI controller equations with output limits (0-100%) as implemented in EASY5™ and used in the standalone C++ code are given as follows [22]:

$$\begin{aligned}
\frac{dERI(t)}{dt} &= K_I\left[\left(R(t)-S_1(t)\right)-K_L\left(S_2(t)-100\%\right)\right], \quad if\ S_2(t) > 100\% \\
\frac{dERI(t)}{dt} &= K_I\left(R(t)-S_1(t)\right), \qquad\qquad if\ 0\% \le S_2(t) \le 100\% \\
\frac{dERI(t)}{dt} &= K_I\left[\left(R(t)-S_1(t)\right)-K_L\left(S_2(t)-0\%\right)\right], \quad if\ S_2(t) < 0\% \\
S_2(t) &= ERI(t)+K_C\left[R(t)-S_1(t)\right]
\end{aligned} \tag{49}$$

Where *ERI(t)* refers to the integrated error signal (%), *R(t)* represents the set-point of the control variable (%), $S_1(t)$ and $S_2(t)$ are the controller feedback and output variables (%). K_C and K_I refer to the feedback gain (%/%) and integral control gain (sec.$^{-1}$) respectively. K_L represents the limiter gain (dimensionless) that prevents the controller output from exceeding the range 0-100%.

For the air-cushioned headboxes where 2- PI controllers are necessary to provide both pressure and level control, Ziegler-Nichols tuning rules were applied to both loops in a trial and error approach. This approach is required as a result of interaction between control loops. To run the weir headbox, level control must be on at all times to prevent the headbox from overfilling with stock.

Fine-tuning of both PI controllers was accomplished simultaneously using the downhill simplex method. The performance criterion which was minimized was the Integrated Absolute Error (IAE). This method is outlined in detail in the next section.

From open-loop frequency responses that are to follow at the three operating points, the responses will be close to one another. As a result an operating point of 75 kPa was selected to optimize the control response since it should give adequate performance at the other two operating points. A summary of the controller gains determined for each headbox using a combination of Ziegler-Nichols closed-loop tuning rules and final optimization using the downhill simplex method is provided in Table 3.

Determining the poles of the closed-loop transfer function can access the local stability of the linearized closed-loop headbox models. Using EASY5™ the closed-loop poles at the three operating points with the controller settings presented in Table 3 can be calculated. A summary of the closed-loop poles calculated for each headbox are found in Tables 4A-4C. From Tables 4A-4C it is apparent that the linearized closed-loop systems are locally stable since all the listed poles have negative real parts. The significance of some of the poles having imaginary parts is that the closed-loop response will exhibit oscillatory behaviour.

The steady-state values of the state variables as well as the level and pressure controller outputs at total pressure operating points of 60, 75 and 90 kPa are presented in Tables 5A-5C. It is observed that for all headboxes as the total pressure operating point increases, the pressure controller output (%), which manipulates the applied armature voltage of the DC motor increases. As a result the armature current (I_A), the speed of the pump (W_{PUMP}) and the corresponding volumetric pump discharge (Q_{PUMP}) all increase.

For the air-cushioned headboxes the level controller maintains the stock level at a constant value. The level controller output (%) decreases since the air-bleed valve closes just enough to maintain the new higher total pressure operating point.

There is no change in stock consistency in any of the control volumes since the conditions of the stock entering the fan pump were not changed. In actuality an increase in the production speed would also require a change in stock consistency in order to maintain the same paper basis weight. Basis weight control, which is part of the complete paper machine control system, was not included in the headbox models.

The values of the state variables in Tables 5A-5C will represent the starting points of the time-domain step responses to be presented in upcoming plots. In addition these values are required for the state-space models since the state-space models generated by EASY5™ are expressed in terms of deviation variables such that the following relationship exists:

$$DeviationVariable = x' = x - x_S \tag{50}$$

Where x_S represents the initial steady-state values.

Table 2: Summary of Model Parameters

(See nomenclature section for parameter details)

Variable Name	Headbox Type		
	Hydraulic	Traditional	Weir
$a\ (m \cdot s^2/rad^2)$	5.50×10^{-3}	5.50×10^{-3}	6.10×10^{-3}
$A_O\ (m^2)$	0.192	----------	----------
$A_1\ (m^2)$	0.427	----------	----------
Air Supply Pressure (Pa)	----------	1.10×10^5	1.10×10^5
$A_{LIP}\ (m^2)$	5.7525×10^{-2}	5.7525×10^{-2}	8.10×10^{-2}
$A_{ATT}\ (m^2)$	0.657	----------	----------
$A_{EQUAL}\ (m^2)$	----------	----------	0.675
$A_{HEADBOX}\ (m^2)$	----------	3.55	1.0
α *(dimensionless)*	0.98	0.98	0.98
P_{ATM} *(Pa)*	101325.0	101325.0	101325.0
$b(s^2/(m^2 \cdot rad))$	5.5×10^{-2}	5.5×10^{-2}	6.3×10^{-3}
$B_{TOTAL}\ (N \cdot m \cdot s/rad)$	5.0	5.0	5.0
C0 (%)	0.61	0.61	0.61
$c\ (s^2/m^3)$	11.3	11.3	10.18
C_D *(dimensionless)*	0.75	----------	----------
$C1_{DIS}$ *(dimensionless)*	----------	32.4	32.4
$C1_{SUP}$ *(dimensionless)*	----------	32.4	32.4
Cg_{DIS} *(dimensionless)*	----------	1400.0	1400.0
Cg_{SUP} *(dimensionless)*	----------	1000.0	1000.0
$C_V\ (USGPM/psi^{1/2})$	----------	----------	205.0
d (m)	3.8×10^{-2}	3.8×10^{-2}	-0.4675
$e_1\ (\% \cdot rad/m^3)$	14588	14588	14588
$e_2\ (\% \cdot rad^2/m^6)$	-6.011×10^5	-6.011×10^5	-6.011×10^5

Variable Name	Headbox Type		
	Hydraulic	Traditional	Weir
$f1\ (s^2/m^3)$	2.5143	3.2	3.2
$f2\ (s^2/m^3)$	3.77	----------	----------
G	1.006	1.006	1.006
G_{AIR}	1.0	1.0	1.0
G_{RATIO}	1.25	1.25	1.25
$H_{ATT}\ (m)$	1.158	----------	----------
$H_{HBX}\ (m)$	----------	1.1856	----------
$H_{S2}\ (m)$	----------	----------	1.85
$H_{STATIC}\ (m)$	8.079	8.079	9.7
$J_{TOTAL}\ (Nms^2/rad)$	87.5	87.5	87.5
$K_A\ (ohm)$	0.01	0.01	0.01
$K_{ATT}\ (Nm^{1.6})$	7.302×10^4	----------	----------
$K_B\ (V's/rad)$	5.0	5.0	5.0
$L_A\ (henry)$	0.988×10^{-3}	0.988×10^{-3}	0.988×10^{-3}
$L_{SPAN}\ (m)$	----------	1.0	0.5
$L_{WEIR}\ (m)$	----------	----------	0.30
$N\ (dimensionless)$	1.2	----------	----------
$P_{SPAN}\ (Pa)$	1.10×10^5	1.10×10^5	1.10×10^5
$R_A\ (ohm)$	0.0188	0.0188	0.0188
$RC_{RATIO}\ (fraction)$	1.53	1.53	1.53
$RR\ (fraction)$	0.065	0.065	0.06
$RecR\ (fraction)$	0.10	0.10	0.10
$Slice\ Height\ (m)$	0.015	0.015	0.015
$T_{AIRPAD}\ (^oC)$	20.0	20.0	20.0
$T_{STOCK}\ (^oC)$	40.0	40.0	40.0
$W_{HBX}\ (m)$	3.835	3.835	5.40
$V_{MAX}\ (V)$	600.0	600.0	600.0
$Vol_1\ (m^3)$	2.0028	2.0028	2.0028
$Vol_2\ (m^3)$	17.9	17.9	17.9
$Vol_3\ (m^3)$	2.356	5.361	2.636
$V_{AIRPAD}\ (m^3)$		2.17	2.22
$V_{HEADBOX}\ (m^3)$	----------	5.175	2.5
$A/L\ (m)$	----------	1.27×10^{-2}	1.27×10^{-2}
$A/L_1\ (m)$	1.74×10^{-2}	----------	----------
$A/L_2\ (m)$	4.72×10^{-2}	----------	----------

Table 3: PI Controller Gains

Headbox Type	Pressure Loop			Level Loop		
	K_C (% / %)	K_I (sec.$^{-1}$)	K_L	K_C (% / %)	K_I (sec.$^{-1}$)	K_L
Hydraulic	0.31	0.635	50.0	----------	----------	-----
Traditional	0.75	0.4	50.0	6.7	1.12	50.0
Weir	0.913	0.49	50.0	1.54	0.34	50.0

Table 4A: Summary of Closed-Loop Poles for Hydraulic Headbox Model

Total Pressure Operating Point		
60 kPa	**75 kPa**	**90 kPa**
-3.82×10^{-2}	-4.27×10^{-2}	-4.68×10^{-2}
-0.290	-0.325	-0.355
-0.365	-0.408	-0.447
$-1.19 \pm 4.27i$	-1.22	-1.24
-1.20	$-1.30 \pm 4.27i$	$-1.38 \pm 5.27i$
$-4.94 \pm 20.7i$	$-5.02 \pm 20.7i$	$-5.12 \pm 20.7i$
-9.84	-11.1	-12.3

Table 4B: Summary of Closed-Loop Poles for Traditional Headbox Model

Total Pressure Operating Point		
60 kPa	**75 kPa**	**90 kPa**
-3.8×10^{-2}	-4.27×10^{-2}	-4.68×10^{-2}
$-0.226 \pm 0.146i$	$-0.252 \pm 0.126i$	$-0.281 \pm 9.73\times10^{-2}i$
-0.29	-0.32	-0.355
-0.365	-0.408	-0.447
-0.47	-0.512	-0.52
$-0.90 \pm 1.727i$	$-0.99 \pm 1.81i$	$-1.1 \pm 1.91i$
$-4.83 \pm 20.6i$	$-4.86 \pm 20.55i$	$-4.89 \pm 20.52i$

Table 4C: Closed-Loop Poles for Weir Headbox Model

Total Pressure Operating Point		
60 kPa	**75 kPa**	**90 kPa**
-5.64×10^{-2}	-6.31×10^{-2}	-6.90×10^{-2}
$-0.328 \pm 8.39 \times 10^{-2} i$	$-0.326 \pm 6.10 \times 10^{-2} i$	$-0.333 \pm 2.65 \times 10^{-2} i$
-0.429	-0.479	-0.524
-0.537	-0.60	$-0.632 \pm 1.10i$
$-0.712 \pm 0.919i$	$-0.615 \pm 1.02i$	-0.656
$-3.19 \pm 1.34i$	$-3.24 \pm 1.88i$	$-3.46 \pm 2.08i$
$-4.94 \pm 20.48i$	$-4.99 \pm 20.44i$	$-5.02 \pm 20.40i$

Table 5A: Hydraulic Headbox Steady-State Values

Variable	Pressure Operating Point		
	60 kPa	**75 kPa**	**90 kPa**
H_{LIP} *(m)*	6.08	7.60	9.12
P_{ATT} *(Pa)*	65523.0	82296.0	99156.0
Q_{PUMP} (m^3/s)	0.732	0.818	0.896
W_{PUMP} *(rad/s)*	61.1	65.7	70.0
I_A *(A)*	417.7	486.6	555.1
C1 (%)	0.610	0.610	0.610
C2 (%)	0.588	0.588	0.588
C3 (%)	0.588	0.588	0.588
Pressure Controller Output (%)	64.2	69.2	73.8

Table 5B: Traditional Headbox Steady-State Values

Variable	Pressure Operating Point		
	60 kPa	75 kPa	90 kPa
Level Set-Point (m)	0.50	0.50	0.50
L_{STOCK} *(m)*	0.50	0.50	0.50
P_{AIRPAD} *(Pa)*	55066.0	70066.0	85066.0
Q_{PUMP} *(m^3/s)*	0.732	0.818	0.896
W_{PUMP} *(rad/s)*	59.9	64.39	68.5
I_A *(amp)*	405.9	471.7	537.3
C1 (%)	0.610	0.610	0.610
C2 (%)	0.588	0.588	0.588
C3 (%)	0.588	0.588	0.588
Level Controller Output (%)	87.7	68.4	50.5
Pressure Controller Output (%)	63.0	67.8	72.2

Table 5C: Weir Headbox Steady-State Values

Variable	Pressure Operating Point		
	60 kPa	75 kPa	90 kPa
Level Set-Point (m)	0.06	0.06	0.06
L_{STOCK} *(m)*	0.06	0.06	0.06
L_{EQUAL} *(m)*	0.326	0.328	0.330
P_{AIRPAD} *(Pa)*	56778.0	71762.0	86747.0
Q_{PUMP} *(m^3/s)*	1.08	1.20	1.31
W_{PUMP} *(rad/s)*	71.8	77.6	83.0
I_A *(amp)*	625.9	739.5	853.1
C1 (%)	0.61	0.61	0.61
C2 (%)	0.588	0.588	0.588
C3 (%)	0.588	0.588	0.588
Level Controller Output (%)	85.3	66.4	48.5
Pressure Controller Output (%)	75.7	81.9	87.7

3.2 Optimization of Controller Gains Using the Downhill Simplex Method

Tuning for MIMO systems like the air-cushioned headboxes depends on the extent of interaction between loops. When interaction between loops is minimal then each loop can be tuned independently using methods that apply to single-input, single-output (SISO) systems.

When strong interaction between loops exists then tuning of both loops must occur simultaneously [23]. As a result each controller contributes to the overall stability and performance of the system.

To reduce the effort required in determining a set of controller parameters that satisfies stability and performance criteria, a trial and error method is used [23]. As an initial estimate of controller parameter values, single-loop values were used with a level of conservatism. Performance optimization can then occur using a random search such as the downhill simplex method provided by Nelder and Mead [24]. With respect to applying the downhill simplex method to aid in controller optimization, the points of the simplex are the Proportional and Integral gains of the PI controllers. The cost function to be minimized is the Integrated Absolute Error (IAE). The error to be minimized is the difference between the controlled variable, *CV(t)* and the set-point, *SP(t)* which is stated as follows:

$$IAE = \int_0^\infty |SP(t) - CV(t)|dt \tag{51}$$

The method is extended to the MIMO case by the addition of weighting factors α and β that are used to emphasize the importance of one control variable to the other. Equation (52) is used to calculate the IAE for a 2 x 2 MIMO system to ensure that both controlled variables track their set-points.

$$IAE = \int_0^\infty \left(\alpha|SP_1(t) - CV_1(t)| + \beta|SP_2(t) - CV_2(t)|\right)dt \tag{52}$$

Where the subscripts *1* and *2* represent the set-point and control variables of loops *1* and *2* respectively. To simplify the optimization procedure, limitations on the control action were not considered in the IAE performance criterion. In practice constraints on the control response would be required.

For the MIMO case the selection of the initial controller tuning parameters could be determined using Ziegler-Nichols closed-loop tuning rules [23]. The combined parameters for both controllers form one point of the simplex. The remaining points of the initial simplex are determined by the following equation:

$$P_i = P_0 + \delta U_i \tag{53}$$

Where P_i refers to the i'th point of the simplex, P_0 is the initial point of the simplex, δ refers to the weighting factor and U_i represents the i'th unit vectors.

The downhill simplex method is applied to the system in the time domain by applying a periodic set-point change to one of the control loops. At the end of each period the IAE is calculated. The algorithm will calculate a new set of controller parameters that will then be applied to the simulated system. Once an "optimal" set of controller parameters is found the local stability of the closed-loop system is determined by evaluating the closed-loop poles. The closed-loop poles presented in Table 4A-4C were evaluated using a feature in EASY5™, which determines the eigenvalues of the system from the Jacobian matrix "A".

With respect to optimal tuning parameters for headbox control, the emphasis is placed on the pressure loop for the air-cushioned headboxes. Level control is also important in maintaining the total head at the slice. Therefore a reasonable weighting must be placed on level control. For the simulations that are to follow a weighting factor ratio of 2:1 (pressure loop weighting : level loop weighting) was selected.

In summary since different weightings of α and β will influence the control performance of both loops, tuning will be a compromise between pressure control and level control [25]. Since small variations in level are not as critical as small variations in total head, it is important that level control be not too "tight" considering that total head control will be more sensitive to disturbances [26]. The reason is that total head at the slice determines the stock velocity to the wire.

3.3 Headbox Responses to a Set-Point Change in Total Head

The response of the hydraulic, traditional, and weir headbox to a ±1% set-point change in total pressure (1100 Pa) is presented in Figures 14-16 respectively. To incorporate three different operating points (60 kPa, 75 kPa, 90 kPa) on one graph, each of the state variables are expressed in terms of deviations from steady-state. The steady-state values of each state variable and the steady-state values of the PI controller outputs are found in Tables 5A-5C.

The closed-loop response of the hydraulic headbox to a ±1% set-point change in total pressure is presented in Figures 14A-14C. From Figure 14A it is shown that with the PI controller gains used (Table 3) the hydraulic headbox gives an underdamped response. Furthermore the response to a downward pressure change is a mirror image of the response of the system to an upward change.

In approximately 4 seconds a 1% change in total head is reached. The average peak percent overshoot for the three operating points is approximately 5.5%. Also the response of the headbox at three different operating points is similar. This reinforces that operating at 60 and 90 kPa with PI controller gains selected for the 75 kPa operating point does not hamper the closed-loop performance.

From a plot of the pressure controller output (%), it is observed that for an upward pressure set-point change of 1%, the change in controller output required to bring about this pressure change varies. This is attributed to the non-linear equations that pertain to the fan pump/DC motor combination as presented in Equations (2-14) and visualized through the fan pump characteristic curves (Figure 11). Since the pressure controller output represents the applied armature voltage (V_A) of the DC motor scaled in terms of percent of voltage span (0 – 600 V), by simply multiplying by the gain 6V/% converts the controller output to a voltage signal. As a result the process closed-loop steady-state gain $V_A(s)$ to $P_{LIP}(s)$ are 499 Pa/V, 535 Pa/V and 569 Pa/V for operating points of 60, 75 and 90 kPa respectively.

Figures 14B-14C illustrate the behaviour of the remaining state variables to a change in total head. As expected as the armature voltage increases the speed of the pump and the corresponding pump discharge increase. Also the sudden change in voltage causes the armature current to spike (+75 A) and then eventually dampen out to a new steady-state.

From Figure 14C it is evident that the response of the pressure in the attenuator air pad (P_{ATT}) is underdamped and follows the same pattern observed for the total head response. It is similar to that of the total head response except that the process closed-loop steady-state gain $V_A(s)$ to $P_{ATT}(s)$ are 554 Pa/V, 595 Pa/V and 633 Pa/V for operating points of 60, 75 and 90 kPa respectively. The explanation for the differences in the steady-state gains of $V_A(s)$ to $P_{LIP}(s)$ and $V_A(s)$ to $P_{ATT}(s)$ is as a result of head losses from the attenuator to the headbox.

Since stock consistency is not influenced by changes in total head, no simulations are provided for the state variables *C1*, *C2* and *C3*. Consistency variations in the approach piping to the headbox could only occur if either the stock consistency fed to the fan pump or the operating conditions of the pressure screen change. Stock consistency variations are considered a disturbance to the pressure loop since changes in consistency effect viscosity, which in turn impact head losses. Stock consistency is included in the headbox models but its effect was not explored in this thesis.

Through simulations it is apparent that the simple design of the hydraulic headbox enables it to quickly change operating conditions thereby reducing the amount of off-grade paper that is generated. In addition the absence of a stock level means that only one PI controller is required to manage total head. As a result from Bernoulli's equation the jet velocity that emerges from the headbox is directly proportional to the square root of the total head generated from the fan pump less any head losses.

The closed-loop response of the traditional headbox to a ±1% set-point change in total pressure is presented in Figures 15A-15C. Using the optimized level and pressure PI controller gains presented in Table 3, the response of the pressure loop illustrated in Figure 15A is underdamped. The average peak percent overshoot for the three operating points is approximately 12.3%. For an upward set-point change in total head, approximately 12 seconds are required for the controlled pressure to obtain its new set-point. In contrast for a downward total head set-point change approximately 13 seconds are required. This is approximately 3 times longer than it took the hydraulic headbox to achieve the same pressure set-point change. The difference can be attributed to the presence of a stock level (Figure 7) that is also controlled. Interaction between the pressure and level control loops is evident by the deviation in the stock level shown in Figure 15A. Given that the span of the level controller is 0-1.0 m, a 1% change in total head varies the stock level by approximately 0.38%, 0.35% and 0.32% for operating points of 60, 75 and 90 kPa respectively. For the traditional headbox the level set-point is not changed during normal operation and is typically set at just above the height of the rotating rectifier rolls to ensure that they are complete submerged. Based on information provided by the local paper mill operating this style of headbox, the level set-point is fixed at 0.5 m.

Although level control is of secondary importance as compared to total head control, since pressure determines the jet velocity out of the headbox slice, the stock level must also be controlled within reasonable limits. The reason is that stock level is controlled by manipulation of the bleed valve position, which affects the air pressure in the air pad. The contribution of the actual stock level to the total head is only 4905 Pa (assuming level set-point of 0.5m), which is approximately 5% to 8% of the total head for the operating points being simulated. The reason why total head and not level is controlled by the manipulation of the applied armature voltage of the DC motor is that only the fan pump can deliver stock to the headbox. This control strategy is best explained through Figure 15B. To increase the total pressure at the slice, the pressure

controller output (%) increases. As the armature voltage increases from Figure 15C the armature current, pump speed and pump discharge flow rate all increase. As a result of the increase in stock flow to the headbox, the stock level in the headbox temporarily increases. Since the stock level is maintained at a specific set-point, the level controller responds by decreasing the bleed valve position. This results in an increase in the air pad pressure (Figure 15B) since the air supply valve position is fixed. The increase in air pad pressure causes the total head to increase. That in turn boosts the flow velocity from the headbox. Since the slice opening is held constant during the total head change, the stock discharge rate from the headbox slice must also increase. This implies that the stock level will eventually return to its set-point and the flow of stock into and out of the headbox will equal one another. From Figure 15A the time that it takes for the stock level to return to its set-point for a positive and negative total head set-point change is approximately 18 and 25 seconds respectively.

Given that the pressure controller span 0-100% represents the voltage span of 0-600V, the closed-loop steady-state gains $V_A(s)$ to $P_{LIP}(s)$ are calculated as 512 Pa/V, 548 Pa/V and 586 Pa/V at total pressure operating points of 60, 75 and 90 kPa respectively. This is comparable to what was calculated for the hydraulic headbox.

The closed-loop response of the weir headbox to a ±1% set-point change in total pressure is presented in Figures 16A-16C. From Figure 16A it is observed that with the level and pressure PI controller gains used (Table 3) the response of the pressure loop is underdamped. The settling time is approximately 10 seconds for a positive and negative total head set-point change. The average peak percent overshoot at each operating point is approximately 8.8%. Also illustrated is the response of the stock level before and after the weir. Like the traditional headbox, stock level is controlled by manipulation of the bleed valve. Recalling from Figure 8, the level that is controlled is that which is after the weir.

The backside of the weir receives approximately 5% of the flow that enters the headbox. The total head at the slice is a summation of the small hydraulic head before the weir and the air pad pressure. The stock level before the weir contributes approximately 5.3%, 4.3% and 3.6% of the total head for operating points of 60, 75 and 90 kPa respectively. From Figure 16A interaction between the pressure and level loops is illustrated by the deviation in the stock level before and after the weir. The stock level set-point is set at 0.06 m with a level sensor span of 0-0.5m. As a result the stock level after the weir deviates from its set-point by approximately

2.3%, 2.1% and 1.9% for a ±1% change in total head at operating points of 60, 75 and 90 kPa respectively. This is on average 6 times greater than the observed level deviation of the traditional headbox. This is a result of the significantly smaller surface area and liquid capacitance of the weir headbox. Consequently a small change in stock flow to the headbox appears as a much larger level deviation in the weir headbox as compared to the traditional headbox.

The stock levels before and after the weir requires approximately 10 seconds to return to steady-state. Since the stock level before the weir is self-regulating, the disturbance of the hydrostatic head on the total head is minimal as compared to that exhibited by the traditional headbox.

Figure 16B illustrates the response of the level and pressure controllers to a change in total head. The responses are similar to that of the traditional headbox. From the steady-state values presented in Table 5C it was shown that as the total head operating point increases the level controller output (%) decreases which implies that the bleed valve is being closed. Like the traditional headbox, level is changed by the manipulation of the bleed valve position but that is where the similarities end. Stock that goes over the weir is removed via a discharge line at the base of the headbox (Figure 8). The control position of the valve on the discharge line is fixed.

The total head above the discharge valve governs the flow leaving the headbox. As a result when the bleed valve closes and the air pad pressure increases, the flow leaving through the discharge line increases. At the same time the elevation in air pad pressure affects the pressure loop. The pressure controller responds to the disturbance by decreasing its output as shown in Figure 16B. The outcome is a drop in pump speed, pump discharge and armature current as presented in Figure 16C. Consequently the amount of flow over the weir is decreased which means the stock level will eventually return to its set-point. From these figures it is clear that for the weir headbox, pressure control is not possible unless level control is present.

The closed-loop steady-state gain $V_A(s)$ to $P_{LIP}(s)$ was calculated as 413 Pa/V, 420 Pa/V and 450 Pa/V for operating points of 60, 75 and 90 kPa respectively. The slight differences in the steady-state gains indicate the non-linear behaviour of the process resulting from the dynamics of the fan pump. The values are slightly lower than that determined for the other two headboxes as a result of differences in the fan pump parameters.

Interaction between the level and pressure loops for the traditional and weir headboxes is also demonstrated by the response of each headbox to a set-point change in stock level. A stock level change of 1% was simulated and the response of the pressure and level loops recorded in Figures 17 and 18 for the traditional and weir headbox respectively. As a result of a larger emphasis placed on the pressure loop, the settling time of the level loop is approximately double that of the pressure loop. From Figures 17 and 18, it is shown that the level response for both headboxes is underdamped. In addition the stock level settling times for the traditional and weir headboxes are approximately 22 and 18 seconds respectively. The weir headbox is capable of responding to level changes quicker than the traditional headbox as a result of the physical differences in size and stock capacity.

An increase in stock level causes the total head at the slice to decrease but the change is negligible (<0.5%). The pressure loop of both air-cushioned headboxes restricts the performance of the level loop. As a result to improve the performance of the level loop so that stock level deviations are minimized for total head set-point changes, an alteration to the control strategy is required. The simplest way to modify the existing control structure without major modifications is through the use of decouplers as described in an upcoming chapter.

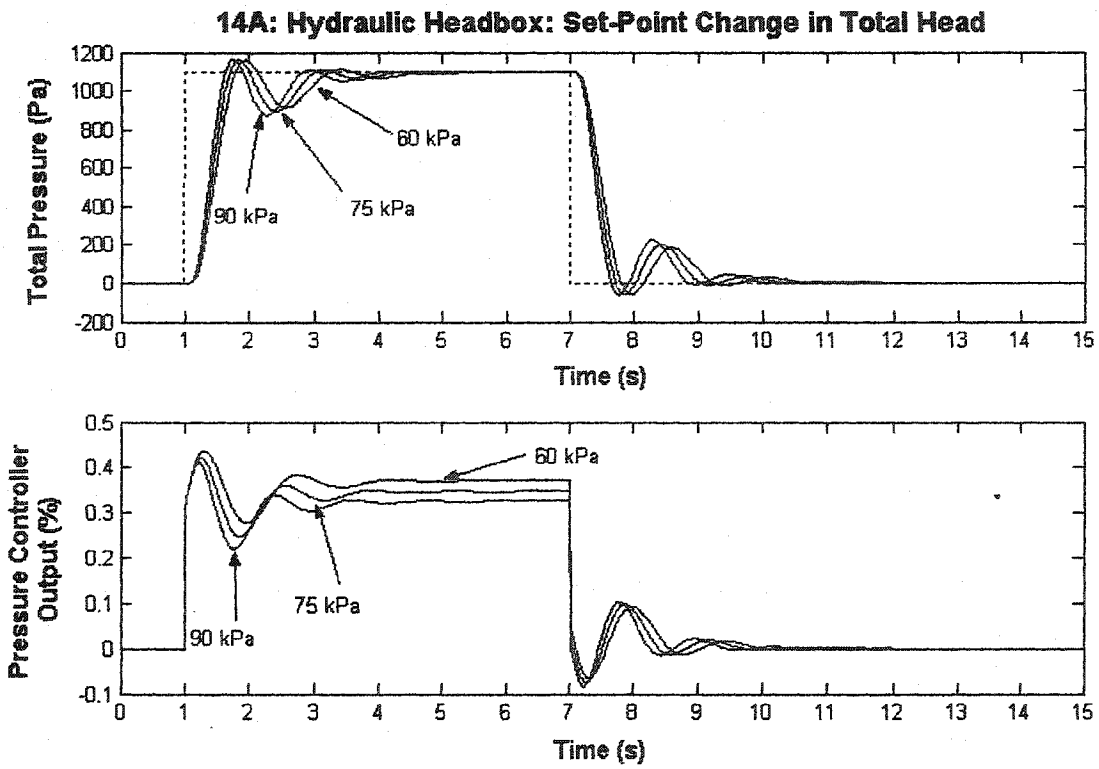

Figure 14B: Hydraulic Headbox: Set-Point Change in Total Head

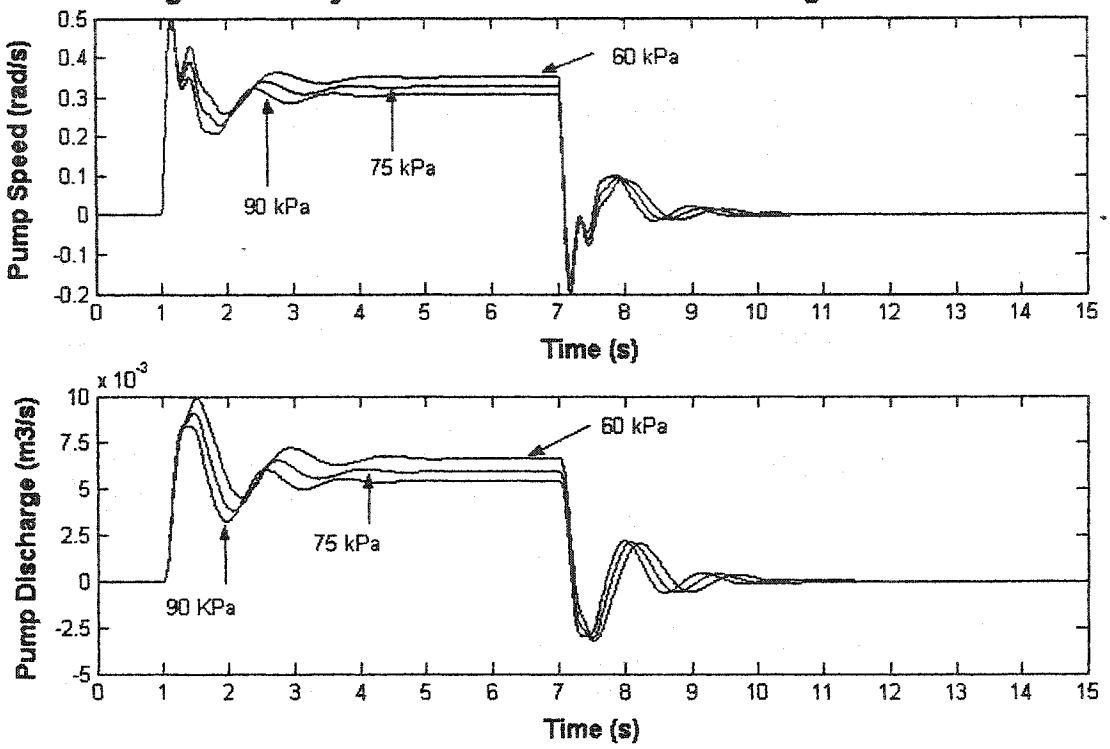

Figure 14C: Hydraulic Headbox: Set-Point Change in Total Head

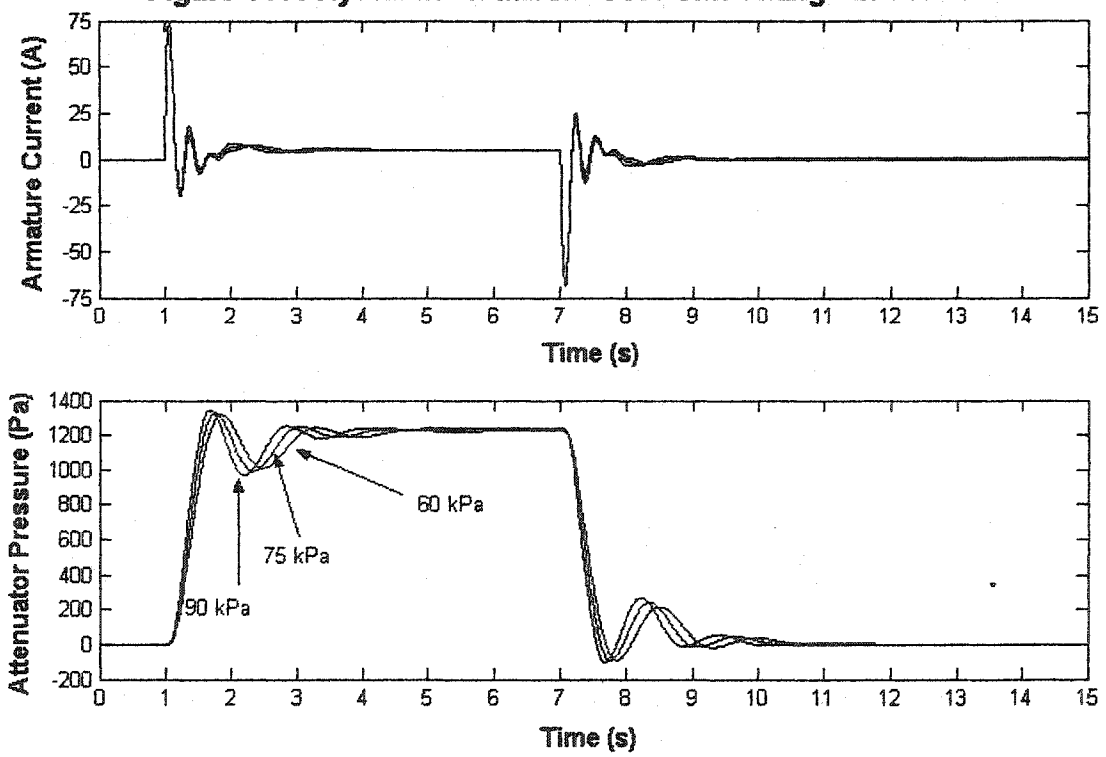

Figure 15A: Traditional Headbox: Set-Point Change in Total Head

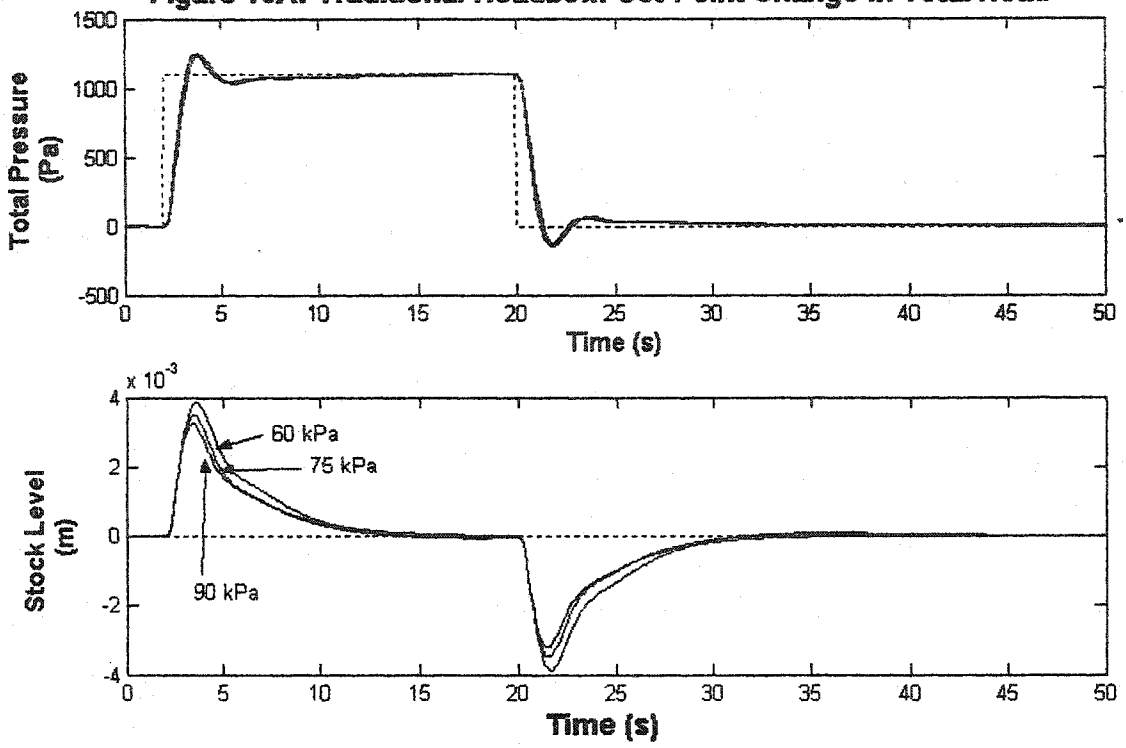

Figure 15B: Traditional Headbox: Set-Point Change in Total Head

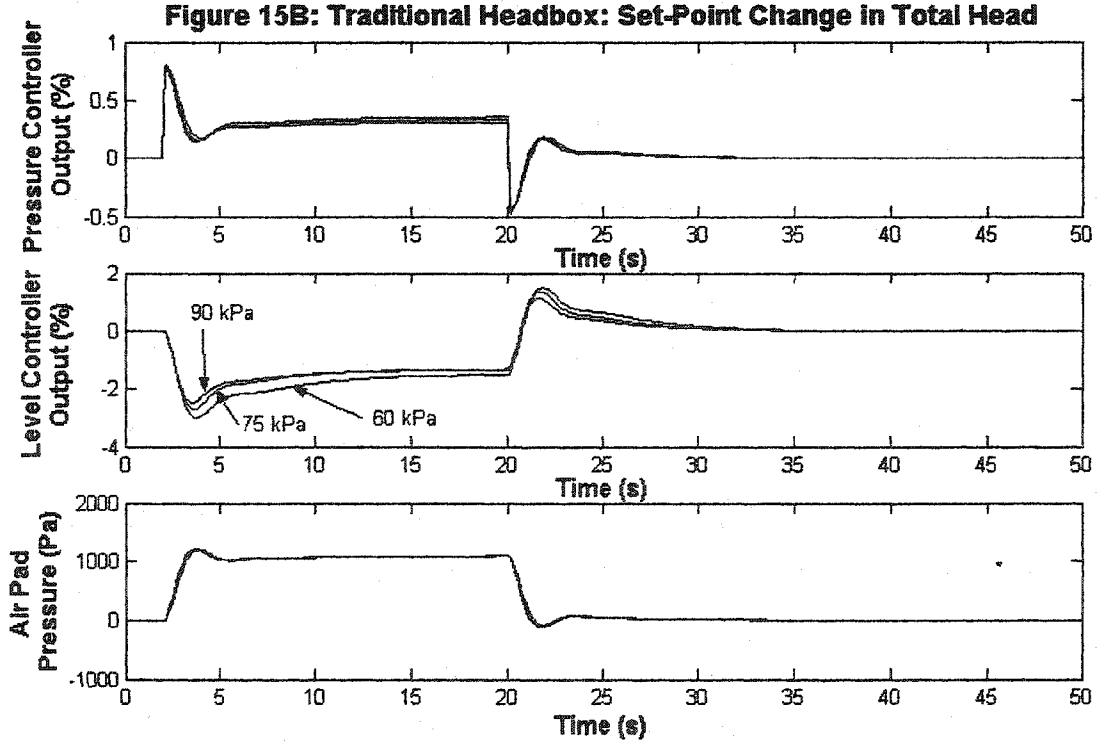

Figure 15C: Traditional Headbox: Set-Point Change in Total Head

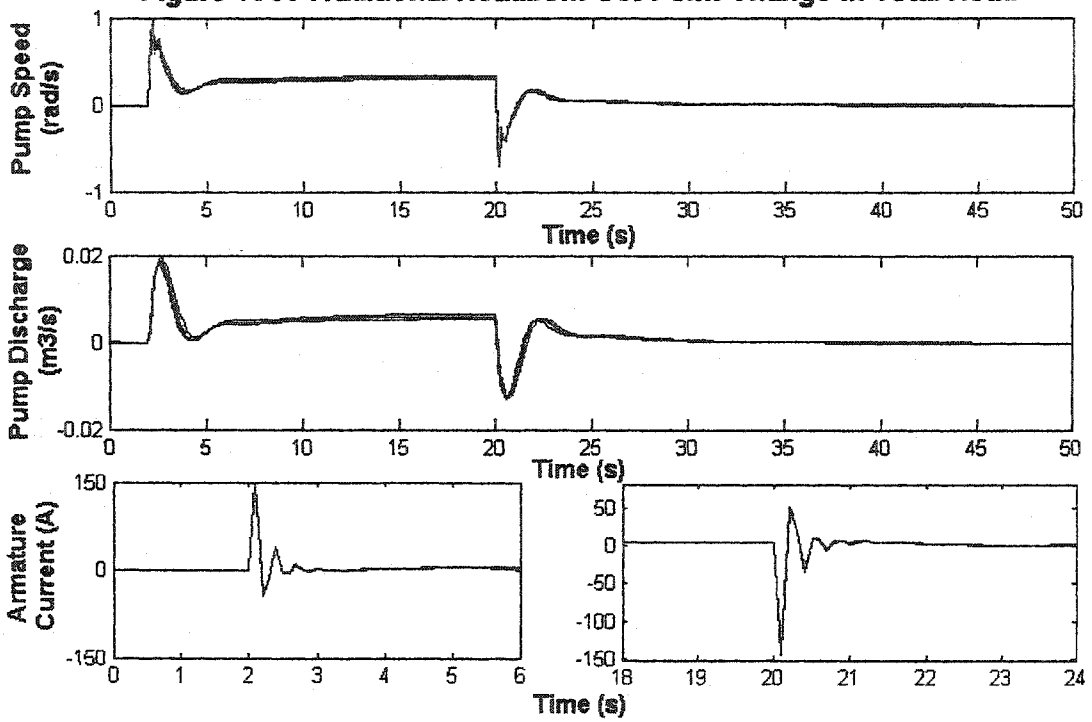

Figure 16A: Weir Headbox: Set-Point Change in Total Head

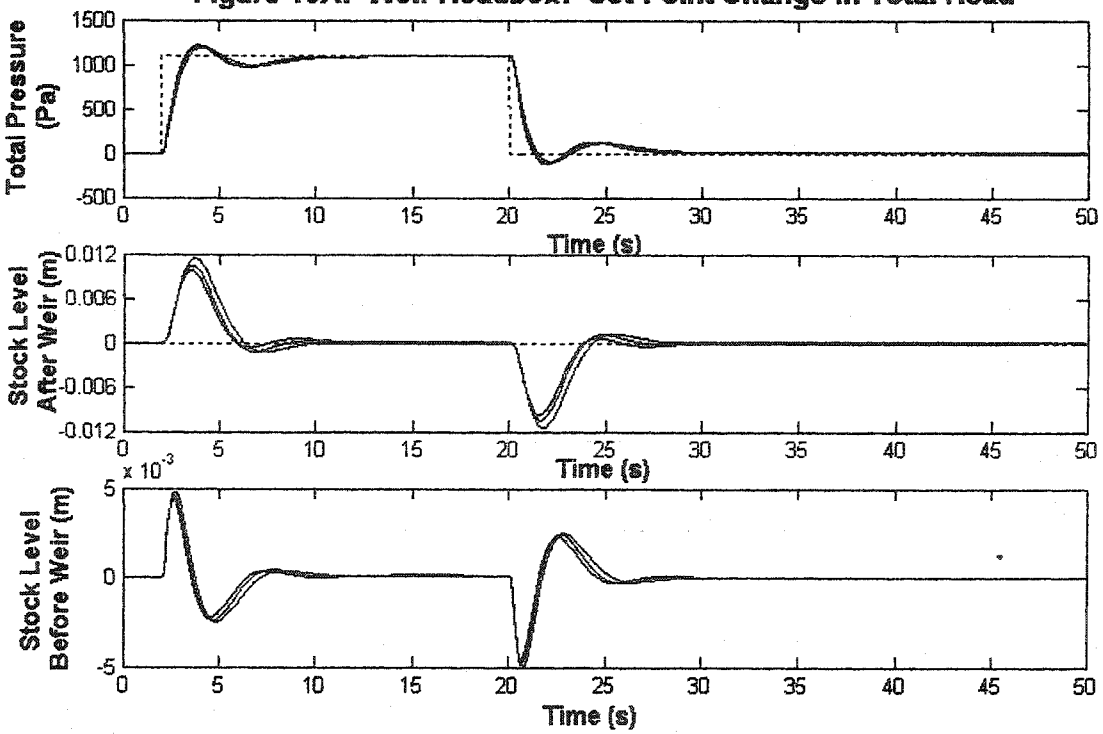

Figure 16B: Weir Headbox: Set-Point Change in Total Head

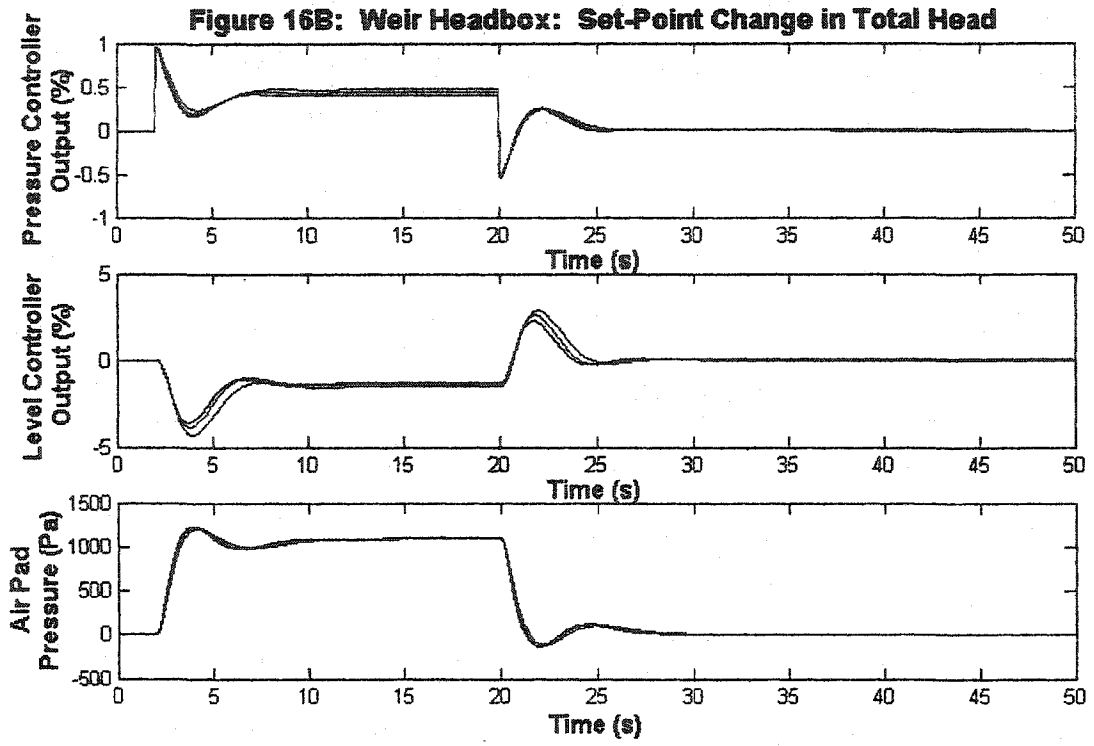

Figure 16C: Weir Headbox: Set-Point Change in Total Head

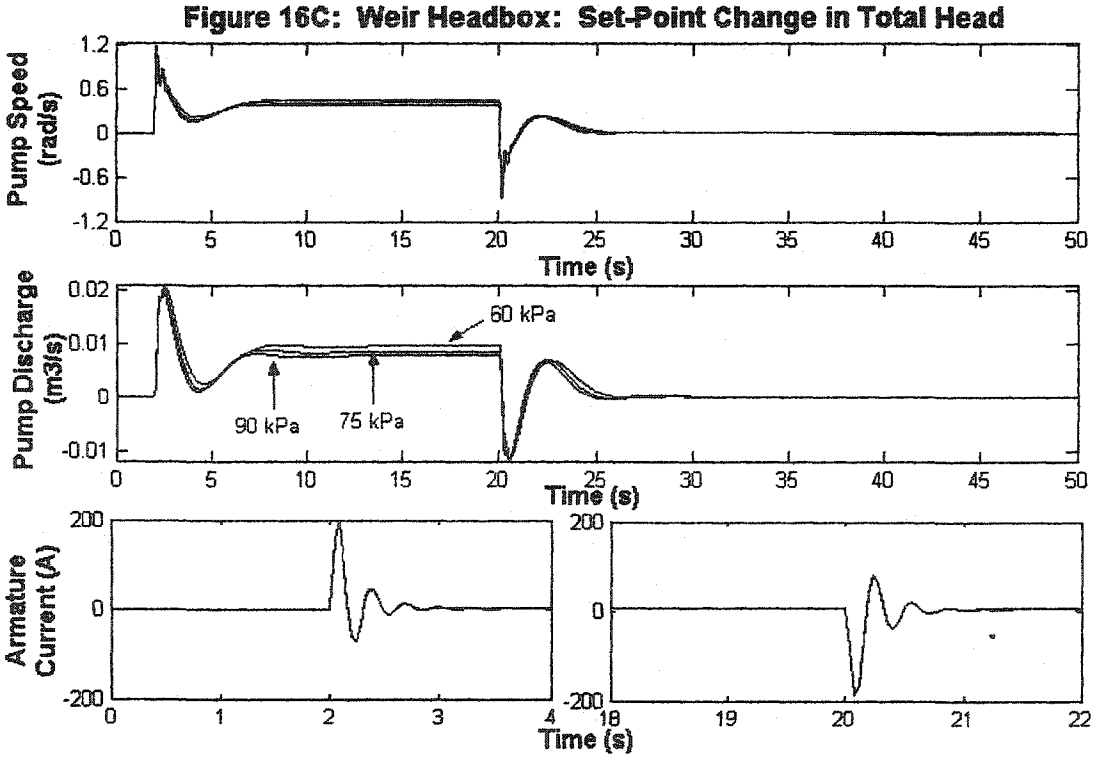

Figure 17: Traditional Headbox: Set-point Change in Stock Level

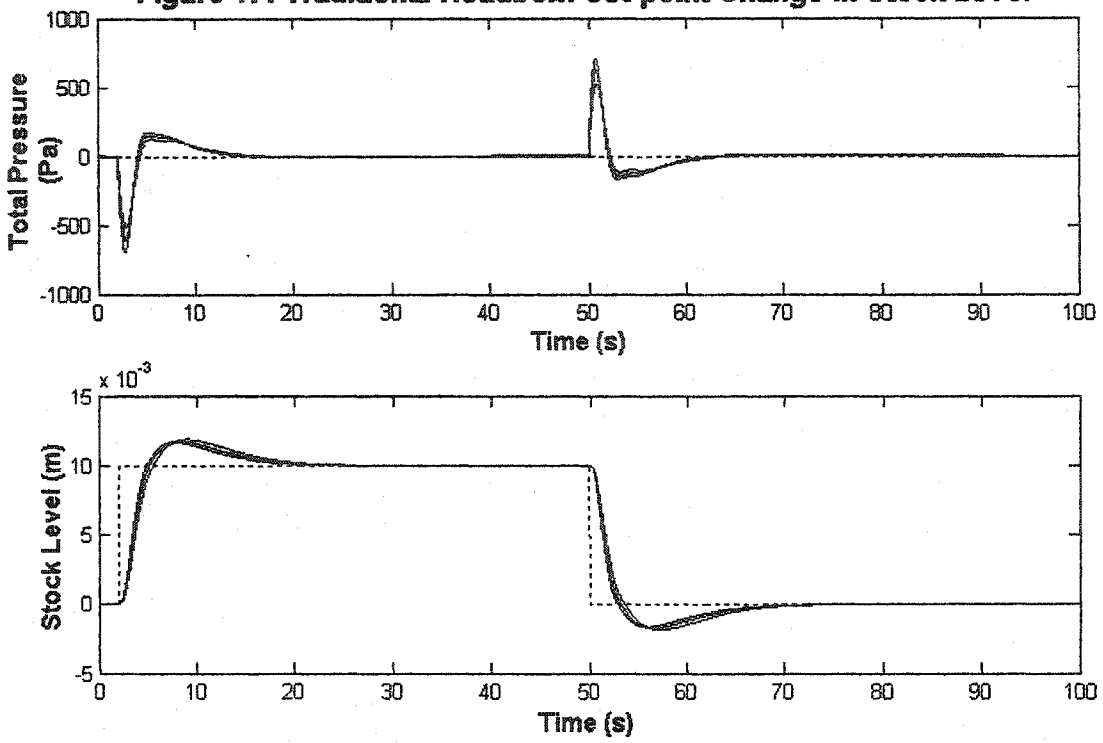

Figure 18: Weir Headbox: Set-Point Change in Stock Level

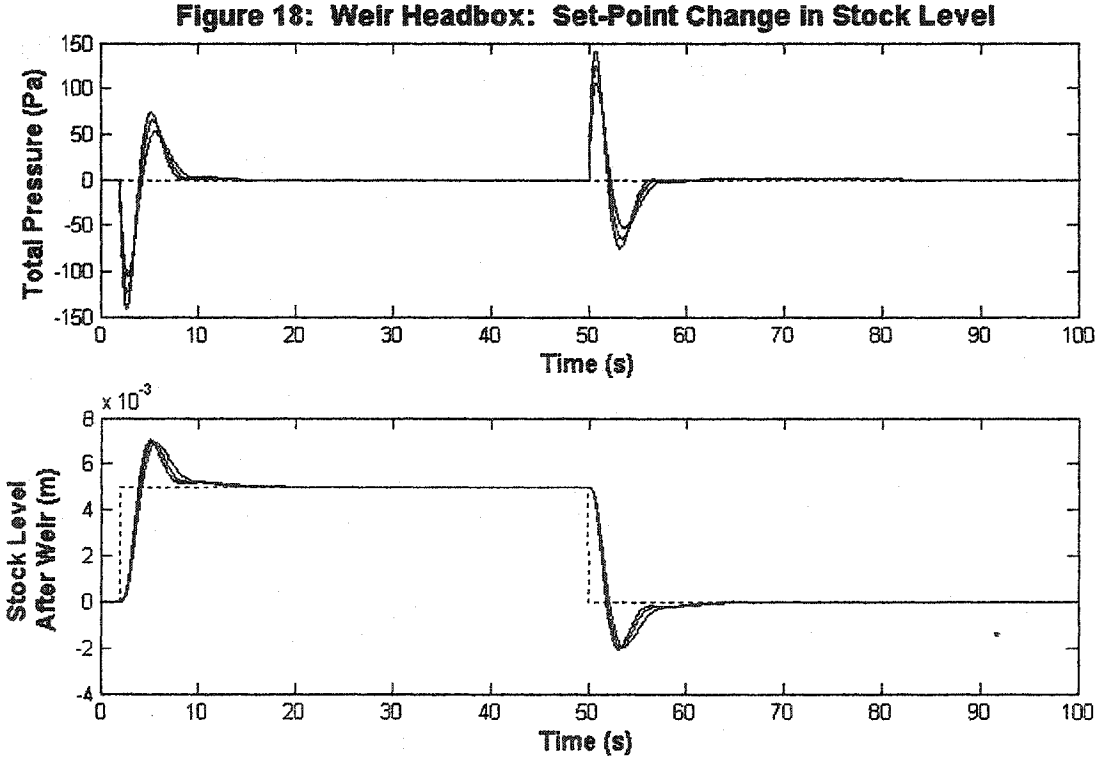

3.4 Closed-Loop Frequency Responses of the Headbox Models

The dynamics of each headbox is best illustrated through the frequency response. With the aid of EASY5™, the closed-loop frequency responses were quickly determined. The input and output variables pictured in each frequency response are scaled in terms of percent of sensor span. The sensor gain 100 %/110000 Pa was used to convert from a pressure to a percent signal. Similarly for the level loop, sensor gains of 100%/1.0 m and 100%/0.5 m were used for the traditional and weir headboxes respectively.

Figure 19 depicts the closed-loop frequency, *total pressure set-point(s)* to *total pressure(s)* for the hydraulic headbox. This shows that the PI controller will track its set-point for frequencies up to 0.3 rad/s. For frequencies greater than this the set-point is changing faster than what the feedback controller can handle thereby making it ineffective. At a frequency of 5 rad/s a resonant peak exists. This explains the underdamped response observed in Figure 14.

The air-cushioned headbox is considered a 2 x 2 MIMO system since there are two input variables (stock level and pressure set-points) and two output variables (stock level, total head) that are regulated. As a result four closed-loop frequency responses, $T_{ij}(s)$ can be determined which relate one set-point j to one output i. Using this notation $T_{11}(s)$ refers to the closed-loop frequency response of the *total pressure set-point(s)* to the *total pressure(s)*. $T_{22}(s)$ relates the *stock level set-point(s)* to the control variable *stock level(s)*. The remaining transfer functions, $T_{12}(s)$ and $T_{21}(s)$ relate the *stock level set-point(s)* to *total pressure(s)* and the *total pressure set-point(s)* to the *stock level(s)* respectively.

From Figures 20 and 21 it is shown that both the level and pressure controllers of the traditional headbox will track their set-points. The bandwidth of the pressure controller is 0 to 0.3 rad/s whereas for the level loop the bandwidth at best is only 0 to 0.08 rad/s. Even though the frequency responses at the three operating points are slightly different, the bandwidths are the same.

Interaction between the level and pressure loops of the traditional headbox is best illustrated through Figures 22 and 23. In both figures the classic frequency response of a SISO feedback control variable to a disturbance is observed. This implies that at low frequencies the feedback controller will attenuate disturbances that result from changes in the other control loop. Disturbances at higher frequencies are also attenuated not due to the feedback controller but as a result of the disturbance time constant being much larger than the disturbance period [23]. At

intermediate frequencies the feedback controllers performance is hampered and in some cases the possibility exists that the disturbance is amplified. The peaks that are observed for each plot indicate this occurrence. The location of the transition points, which define the plateau region at these intermediate frequencies coincide fairly closely with the corner frequencies depicted in Figures 20 and 21. At a frequency of 1.5 rad/s, which is approximately the location of the peaks for both Figures 22 and 23, the closed-loop gains $T_{12}(s)$ and $T_{21}(s)$ have average values of –1 dB and –8 dB respectively. Therefore a 1% change in level or pressure set-points cause the other loops control variable to deviate by 0.89% (980 Pa) and 0.4% (0.004 m) respectively.

The closed-loop frequency responses pertaining to the weir headbox are found in Figures 24-27. Figures 24 and 25 illustrate that both level and pressure controllers will track their set-points at frequencies below 0.06 rad/s and 0.15 rad/s respectively. For frequencies between 0.7 rad/s and 2.0 rad/s the pressure loop exhibits resonance with the peak located at approximately 1.1 rad/s. Compared to the values obtained for the traditional headbox the bandwidth of the level controllers are fairly close (difference of 0.02 rad/s), whereas the pressure controller bandwidth is reduced by approximately 0.15 rad/s.

Similar to the traditional headbox, interaction between control loops pertaining to the weir headbox is observed through Figures 26 and 27. The basic shapes of these curves are similar to that found in Figures 22 and 23 except that for the weir headbox, the pressure loop has a stronger effect on the level loop. From Figures 26 and 27 a resonant peak can be found at approximately 1.2 rad/s. At this frequency the average closed-loop gains $T_{12}(s)$ and $T_{21}(s)$ are calculated as –12.0 dB and 11.0 dB respectively. This implies that at this frequency a 1% change in either the level or pressure set-points would alter the other loops control variable by 0.25% (276 Pa) and 3.5% (0.018 m). The deviations in the level loop caused by changes to the pressure loop of the weir headbox are approximately 9 times greater than the level deviations of the traditional headbox. This is a consequence of the differences in the capacitance of the two headboxes.

The objective of reducing the influence that the pressure loop has on the level loop as observed through the closed-loop gain $T_{21}(s)$, can be accomplished by the addition of one-way decoupling as is discussed in a separate chapter.

From the closed-loop frequency responses it was discovered that the maximum bandwidth (±1dB) that can be achieved by our pressure loop feedback controllers was 2.0 rad/s.

As a result our headbox models are limited to surge flow models that can predict the response of the system for frequencies below 10 rad/s. At intermediate frequencies (10 rad/s –60 rad/s) the design of the headbox and the proper functioning of pulsation damping systems become important for disturbance rejection [16].

Figure 19: Hydraulic Headbox Closed-Loop Freq. Resp.
Total Pressure Set-Point(s) to Total Pressure(s)

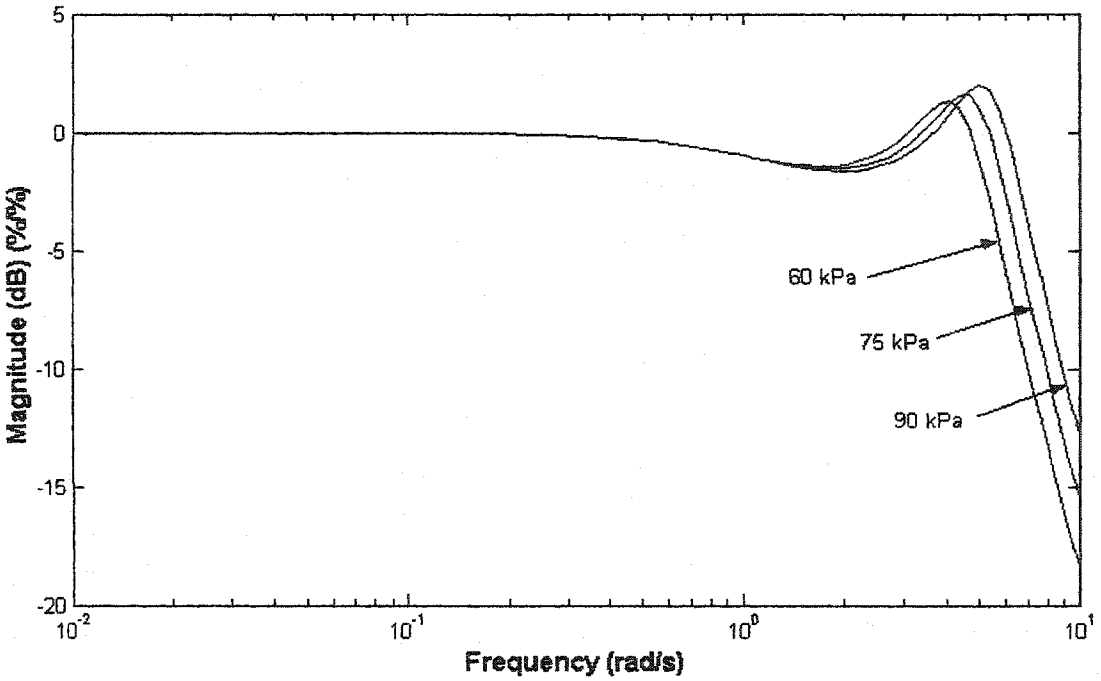

Figure 20: Traditional Headbox Closed-Loop Freq. Resp.
T11(s): Total Pressure Set-Point(s) to Total Pressure(s)

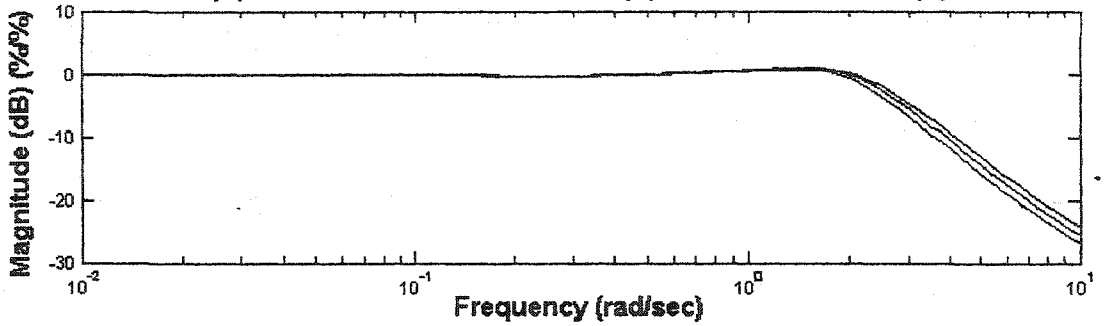

Figure 21: Traditional Headbox Closed-Loop Freq. Resp.
T22(s): Stock Level Set-Point(s) to Stock Level(s)

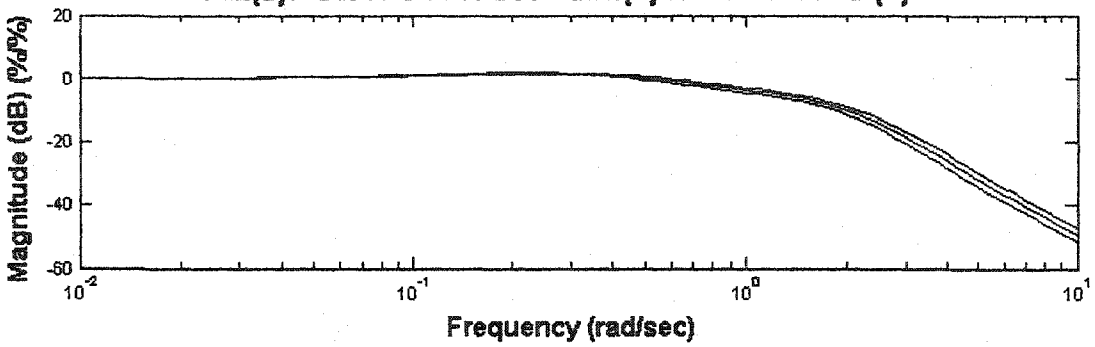

Figure 22: Traditional Headbox Closed-Loop Freq. Resp.
T12(s): Stock Level Set-Point(s) to Total Pressure(s)

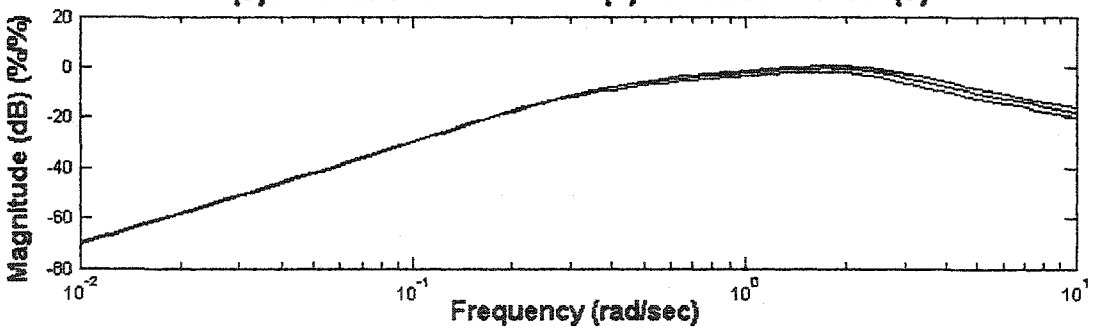

Figure 23: Traditional Headbox Closed-Loop Freq. Resp.
T21(s): Total Pressure Set-Point(s) to Stock Level(s)

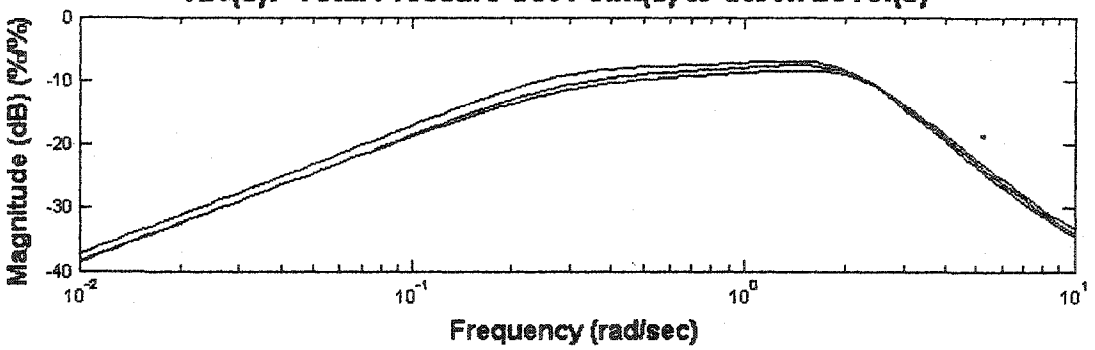

Figure 24: Weir Headbox Closed-Loop Freq. Resp.
T11(s): Total Pressure Set-Point(s) to Total Pressure(s)

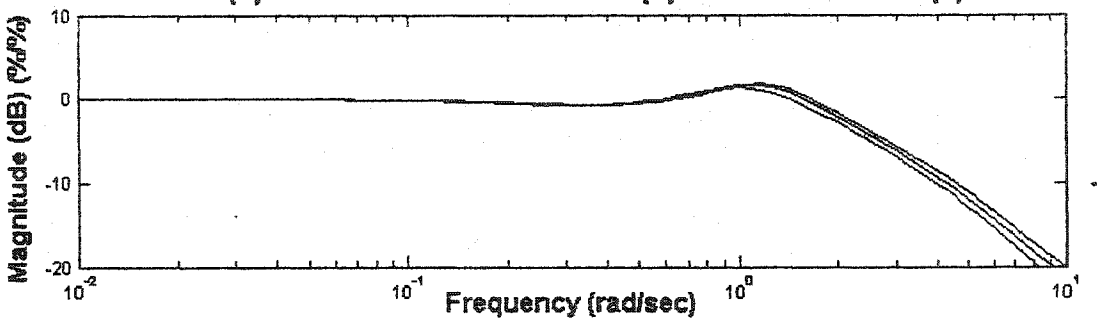

Figure 25: Weir Headbox Closed-Loop Freq. Resp.
T22(s): Stock Level Set-Point(s) to Stock Level(s)

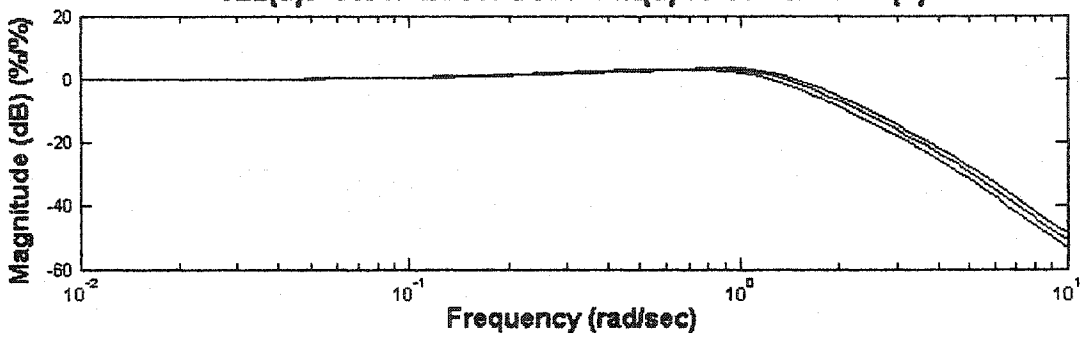

Figure 26: Weir Headbox Closed-Loop Freq. Resp.
T12(s): Stock Level Set-Point(s) to Total Pressure(s)

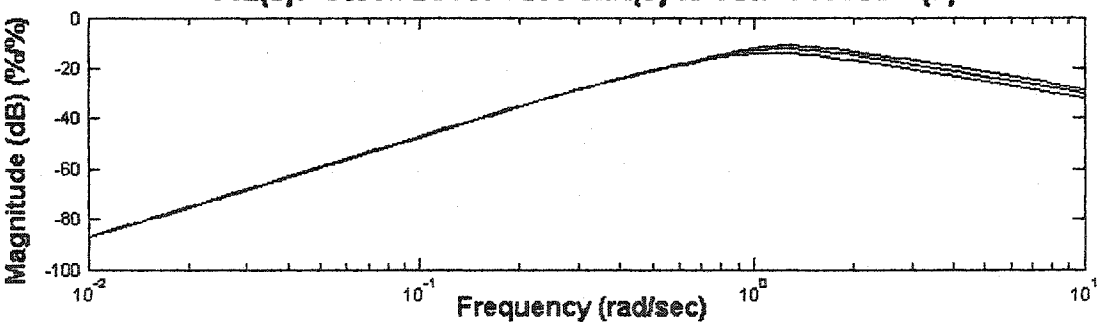

Figure 27: Weir Headbox Closed-Loop Freq. Resp.
T21(s): Total Pressure Set-Point(s) to Stock Level(s)

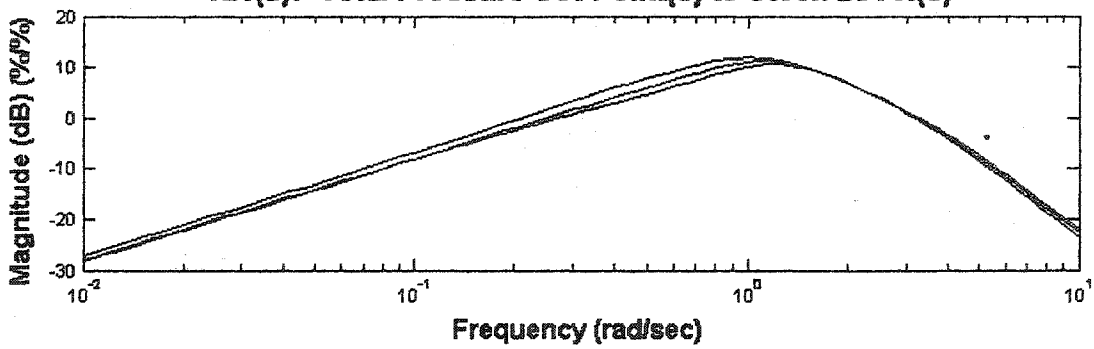

3.5 Open-loop Frequency Responses of the Headbox Models

Open-loop frequency responses pertaining to the three headboxes at operating points of 60, 75, and 90 kPa are found in Figures 28 to 35. The open-loop frequency responses were determined mathematically from the closed-loop frequency responses as outlined in Appendix A.5. The input and output variables have been scaled in terms of percent of controller span (0-100%) and sensor span (0-110000 Pa, traditional headbox level sensor span 0-1.0 m, weir headbox level sensor span 0-0.5 m).

For all three headboxes the input variables refer to the output of the controller(s) in terms of a percent of span. The output of the pressure controller refers to the applied armature voltage (0-600 V) whereas the output of the level controller represents the position of the air bleed valve (0- 100%). The output variables are the total pressure and stock level in percent of span.

With the air-cushioned headboxes the notation that is used is that $G_{11}(s)$ represents the effect that the armature voltage has on the total pressure and $G_{22}(s)$ represents the effect that the bleed valve has on the stock level. The cross gain $G_{12}(s)$ refers to the effect that the bleed valve has on the total pressure and $G_{21}(s)$ represents the effect that the armature voltage has on the stock level.

Figure 28 illustrates the open-loop response of the hydraulic headbox. It is shown that the dynamics of the system change at different operating points, as a result of the operating characteristic of the fan pump. The open-loop gain $V_A(s)$ to $P_{LIP}(s)$ at 60, 75 and 90 kPa are 482 Pa/V, 522 Pa/V and 555 Pa/V at frequencies below 2.0 rad/s. These values are similar to what was obtained directly from the closed-loop step response plots (Figure 14A, 14B).

The open-loop frequency response of the traditional headbox is presented in Figures 29 to 32. The large frequency range was used to fully illustrate the stock level behaviour. Included in each of these figures is a single dotted line, which represents the frequency response that would result by assuming that the air pad volume is constant and is not affected by stock level changes. This was accomplished by setting the derivative term dV_{AIRPAD}/dt found in Equation (25) to zero. This was included because some literature models have incorrectly omitted this term, which has a significant stabilizing affect.

From Figure 29 the strong effect that the fan pump has on the total pressure through the process gain $G_{11}(s)$ ($V_A(s)$ to $P_{LIP}(s)$) is observed. At low frequencies the average open-loop gain $G_{11}(s)$ for pressure operating points of 60, 75 and 90 kPa are 511 Pa/V, 547 Pa/V and 586 Pa/V.

By varying the armature voltage, the speed and discharge flow rate of the fan pump change. With the bleed valve in a fixed position (level controller on manual) an increase in stock flow rate to the headbox appears as a significant increase to the stock level. The strong effect that the fan pump has on the stock level is clearly demonstrated in Figure 32 where at low frequencies the process gain $G_{21}(s)$ has an average steady-state value of 30.5 dB (33.5 %/% → 0.0558 m/V). Since at low frequencies the air pad pressure remains relatively constant, the increase in stock level adds to the total head at the slice. This explains why the fan pump has a strong effect on the total head. Using the steady-state gains calculated above at an operating point of 75 kPa an armature voltage increase of 1 V would at low frequencies cause the level to increase by 0.0558 m, which translates to a pressure increase of 547 Pa. This corresponds directly with the steady-state open-loop gain of $G_{11}(s)$ that was determined to be 547 Pa/V at low frequencies.

Differences associated with assuming that the air pad volume is constant or not are observed in Figures 29 and 32 at frequencies greater than 1.0×10^{-2} rad/s for the process gains $G_{11}(s)$ and $G_{21}(s)$. These differences are noticeable at high frequencies since quick changes in the stock level acts to either compress or expand the air in the air pad depending on if the stock level is increasing or decreasing. The air pad effectively contributes to dynamic lead in this frequency region.

Figure 30 illustrates the strong effect that the bleed valve has on the stock level ($G_{22}(s)$). The process gain decreases with increasing frequency with a slope of –20 dB/decade. The strong influence of the bleed valve on the stock level is a result of the discharge flow rate out of the headbox, which depends on the total head above the slice.

Figure 31 shows that at very low frequencies the effect of the bleed valve on the total head ($G_{12}(s)$) is extremely small (steady-state value of ≈ –102 dB). The reason is that at low frequencies the increase in stock level caused by the opening of the bleed valve (Figure 30) is sufficient enough to completely compensate for the decrease in air pad pressure. At intermediate frequencies (1.0×10^{-2} to 1.0 rad/s) the bleed valve has a more significant influence on total head. If the air pad volume is assumed constant, the gain $G_{12}(s)$ calculated at the peak location has an open-loop value of –3.2 dB (0.69 %/% → 761 Pa/%). The open-loop gain $G_{12}(s)$ is decreased to –14.2 dB (0.19 %/% → 214 Pa/%) by assuming that the stock level influences the air pad volume.

The open-loop responses of the weir headbox are presented in Figures 33 to 36. At low frequencies the effect of the fan pump on the total head ($G_{11}(s)$) is weak. In contrast at frequencies between 1.0 x 10^{-3} and 1.0 rad/s the effect is strong. For these frequencies the average open-loop gain of $G_{11}(s)$ is approximately 4.5 dB (1.68 %/% → 307 Pa/V) compared to a value of –21.5 dB (0.084 %/% → 15.4 Pa/V) at frequencies below 1.0 x 10^{-5} rad/s. Unlike the traditional headbox where the strong effect of the fan pump on the total pressure was attributed entirely to stock level changes, with the weir headbox at very low frequencies the level before the weir does not change enough to contribute to an increase in total head. On the other hand the fan pump has a strong effect on the stock level after the weir as illustrated in Figure 36. At low frequencies the process gain $G_{21}(s)$ ($V_A(s)$ to $L_{STOCK}(s)$) is approximately 65.1 dB (1799 %/% → 1.50 m/V). This is approximately 27 times larger (comparing gains in engineering units, m/V) than the value calculated for the traditional headbox. The large difference is a result of the smaller liquid capacitance, lower cross sectional area of the weir headbox. Consequently the effect that the stock level has on the air pad pressure tends to be larger than that determined for the traditional headbox. As a result at frequencies above 1.0 x 10^{-4} rad/s the effect of the fan pump on the total head is strong as a consequence of the strong effect the after weir level has on the air pad pressure. In Figure 33 it is shown that by assuming that the air pad volume is not constant the open-loop gain $G_{11}(s)$ increases by approximately 26 dB. The positive phase angle illustrated in Figure 33 at low frequencies is due to the presence of a derivative term (dV_{AIRPAD}/dt) on the right side of Equation (25), which contributes positive phase (derivative lead).

The strong effect of the bleed valve on the stock level ($G_{22}(s)$) is observed in Figure 34. At low frequencies the process gain $G_{22}(s)$ has an average value of 55.6 dB (603 %/% → 3.0 m/%). The reason for the strong effect is that the bleed valve controls the flow rate of stock through the headbox slice and the stock discharge line. At frequencies between 2.0 x 10^{-3} and 0.1 rad/s the phase angle is approximately -90^0 which indicates integrating characteristics. As a result when the flow over the weir is different than the flow exiting through the discharge valve, the rate at which the stock level changes will depend on the differences in flow.

Figure 35 illustrates that at frequencies below 2.0 x 10^{-4} rad/s the bleed valve has a strong effect on the total head ($G_{12}(s)$). In contrast with the traditional headbox the effect of the bleed valve on the total head was determined to be weak. With the traditional headbox if the air bleed

valve were opened, the air pad pressure would suddenly drop but the increase in stock level would eventually make up the pressure difference thereby keeping the total pressure constant. This is not possible with the weir headbox because of the presence of the weir. At low frequencies the process gain $G_{12}(s)$ has an average value of –2.7 dB (0.73 %/% → –806 Pa/%). The process gain is negative since an increase in the bleed valve position at low frequencies causes a decrease in the total pressure. This could also be determined by looking at the phase angle, which is less than -180^0. In Figure 35 it is illustrated that by assuming that the air pad volume changes, the open-loop gain $G_{12}(s)$ is reduced by approximately 12 dB at frequencies between 1.0×10^{-2} and 0.2 rad/s.

Figure 28: Hydraulic Headbox Open-Loop Freq. Resp.
Pressure Controller Output(s) to Total Pressure(s)

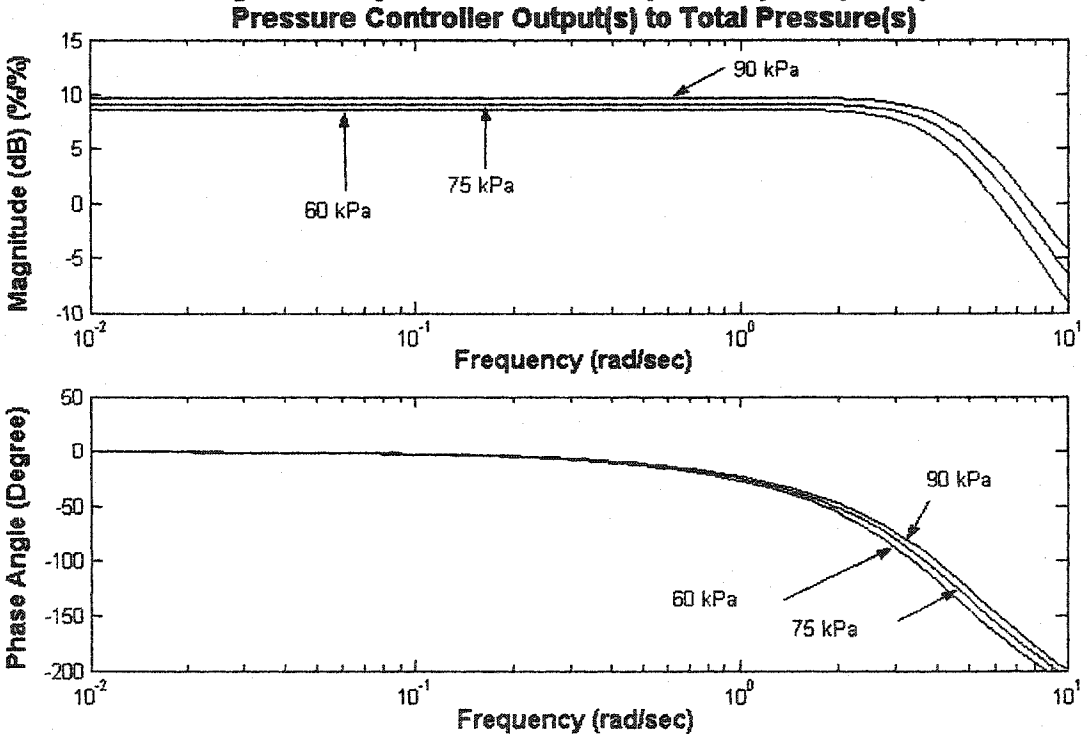

Figure 29: Traditional Headbox Open-Loop Freq. Resp.
G11(s): Pressure Controller Output(s) to Total Pressure(s)

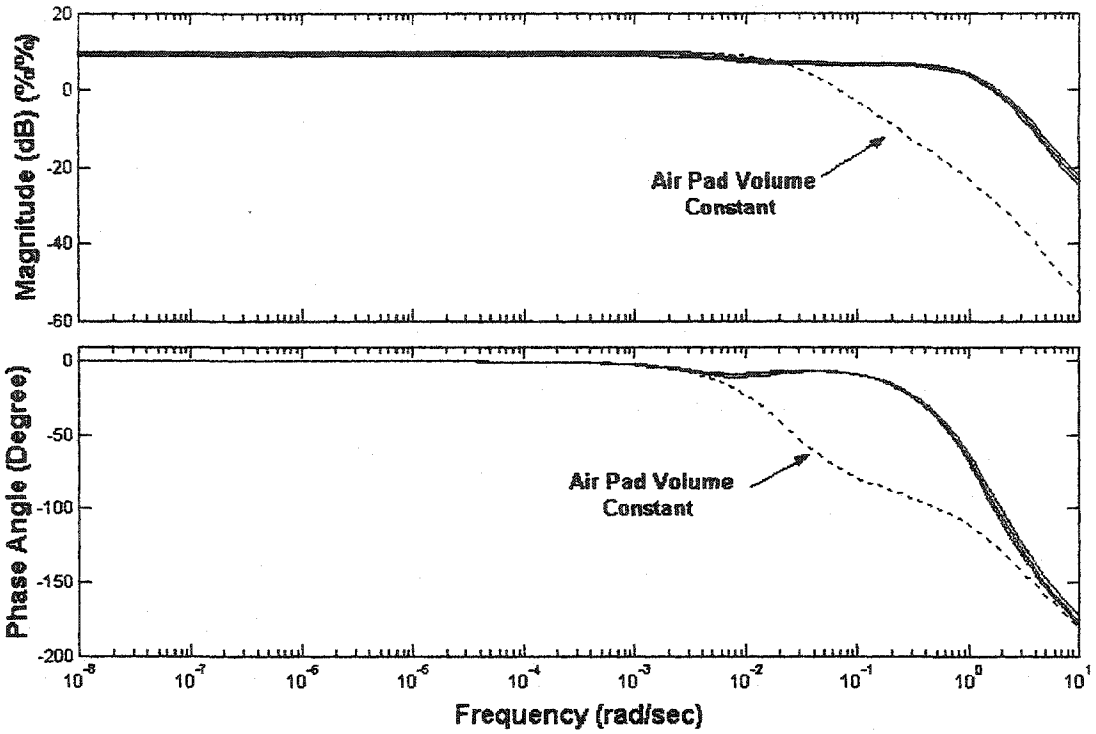

Figure 30: Traditional Headbox Open-Loop Freq. Resp.
G22(s): Stock Level Controller Output(s) to Stock Level(s)

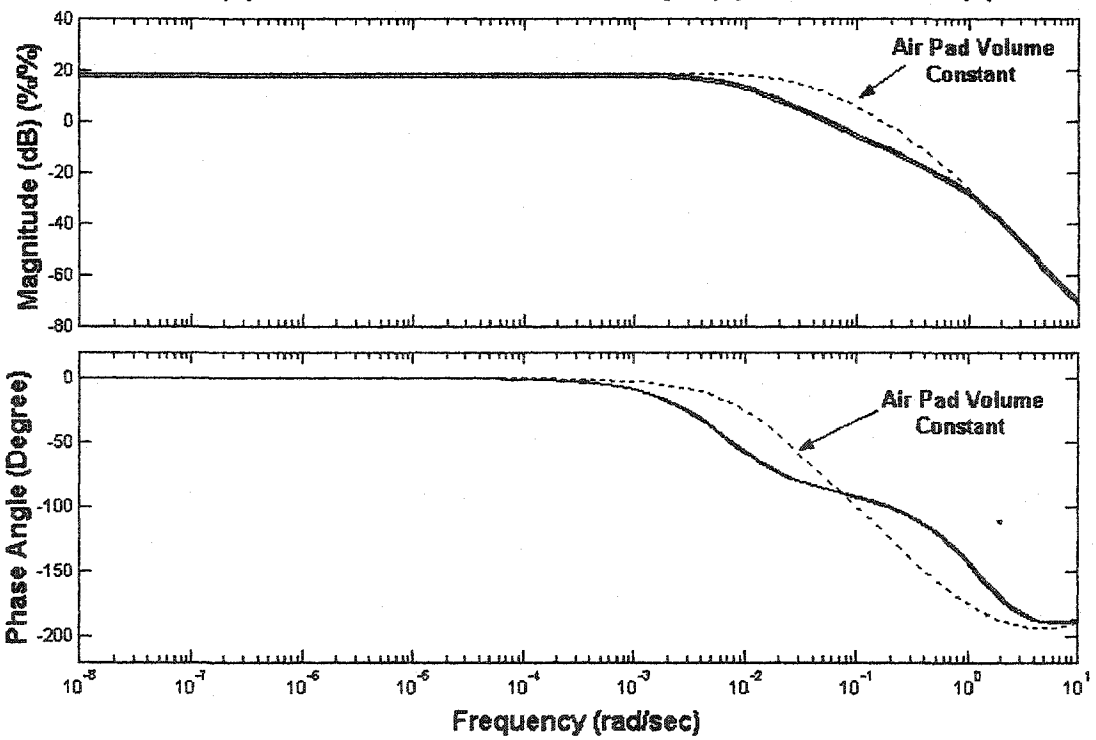

Figure 31: Traditional Headbox Open-Loop Freq. Resp.
G12(s): Stock Level Controller Output(s) to Total Pressure(s)

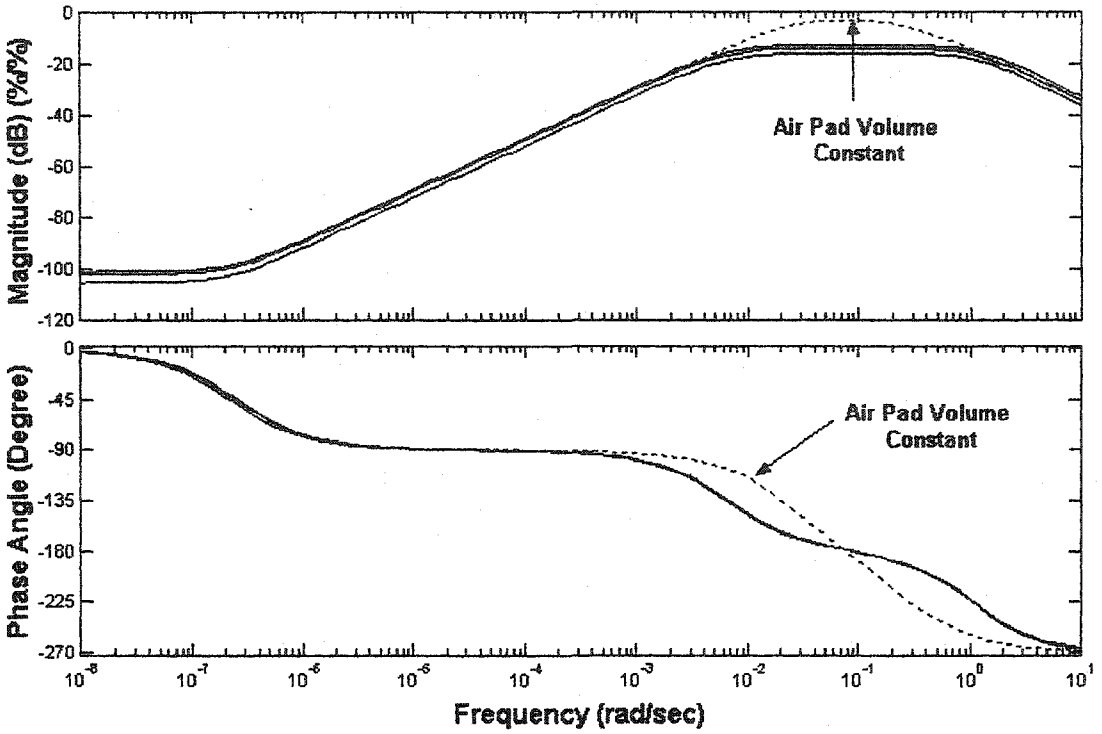

Figure 32: Traditional Headbox Open-Loop Freq. Resp.
G21(s): Pressure Controller Output(s) to Stock Level(s)

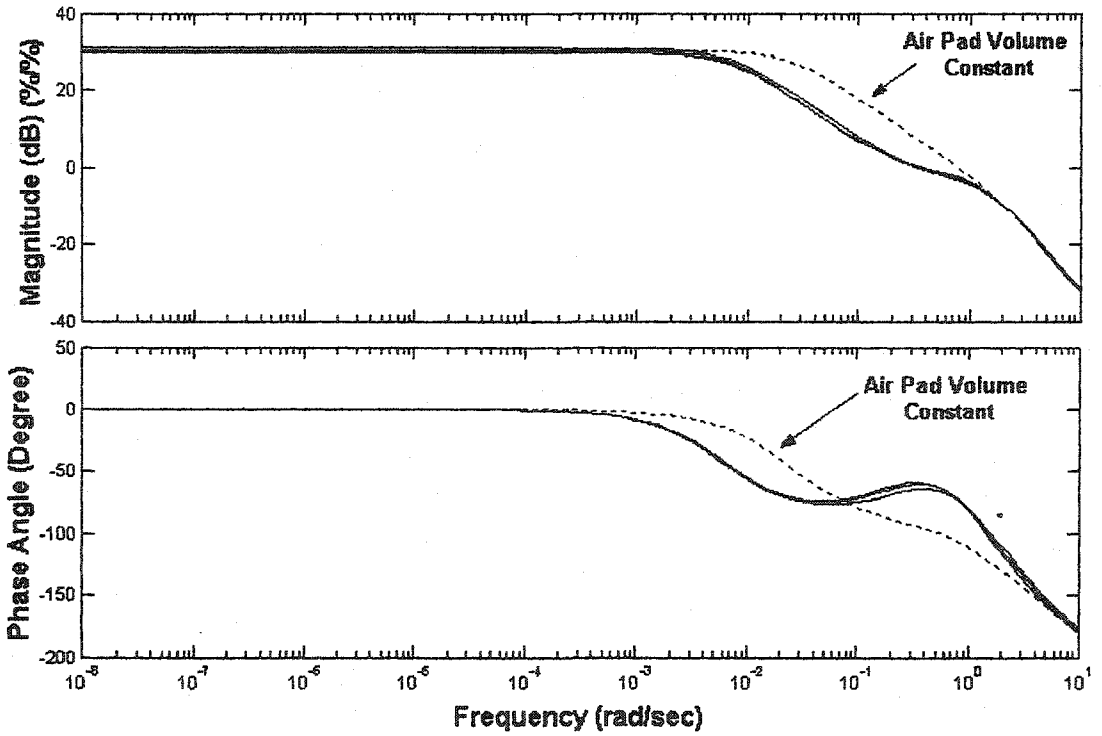

Figure 33: Weir Headbox Open-Loop Freq. Resp.
G11(s): Pressure Controller Output(s) to Total Pressure(s)

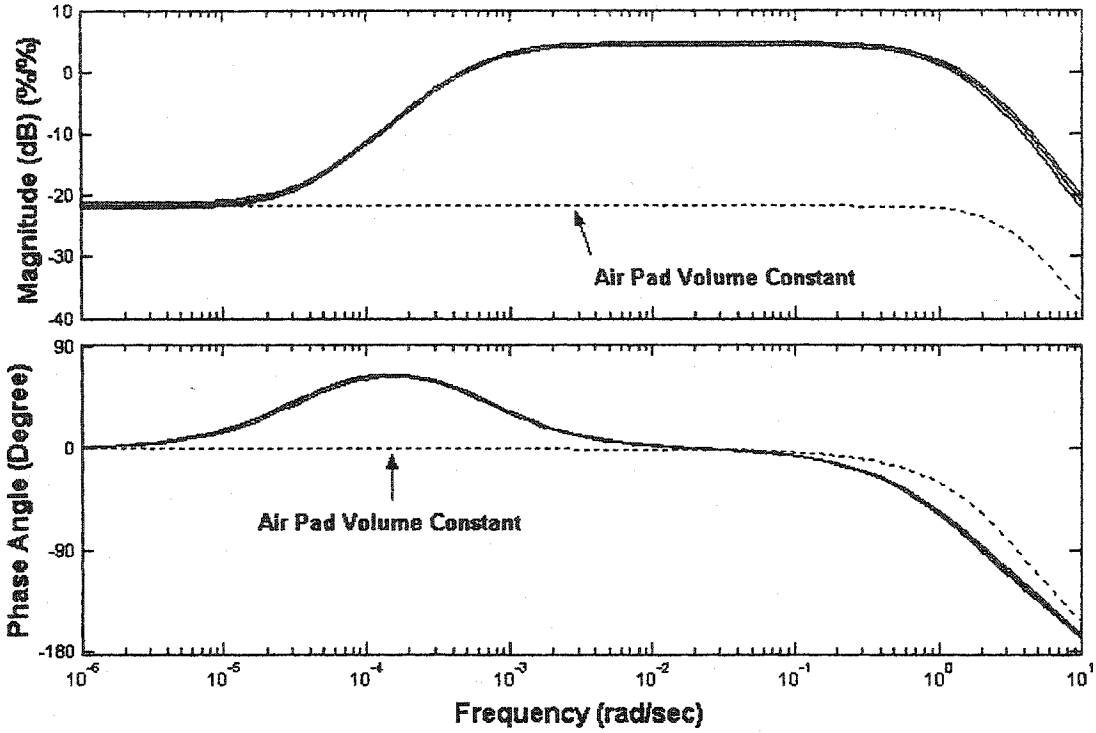

Figure 34: Weir Headbox Open-Loop Freq. Resp.
G22(s): Stock Level Controller Output(s) to Stock Level(s)

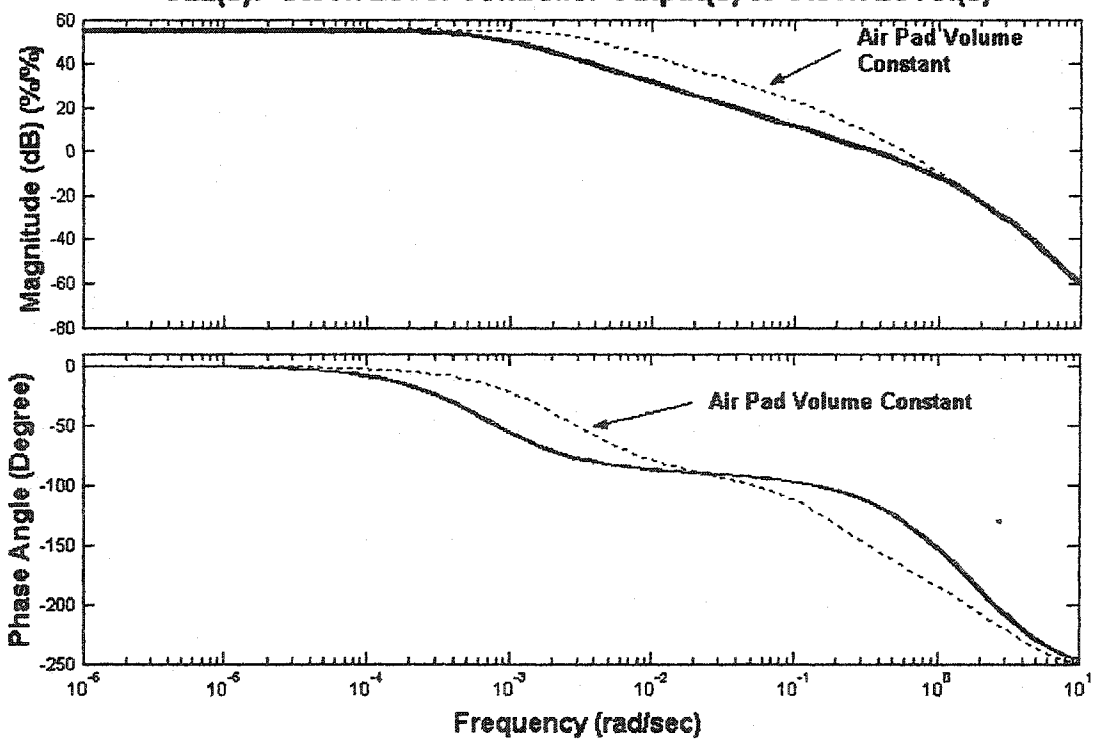

Figure 35: Weir Headbox Open-Loop Freq. Resp.
G12(s): Stock Level Controller Output(s) to Total Pressure(s)

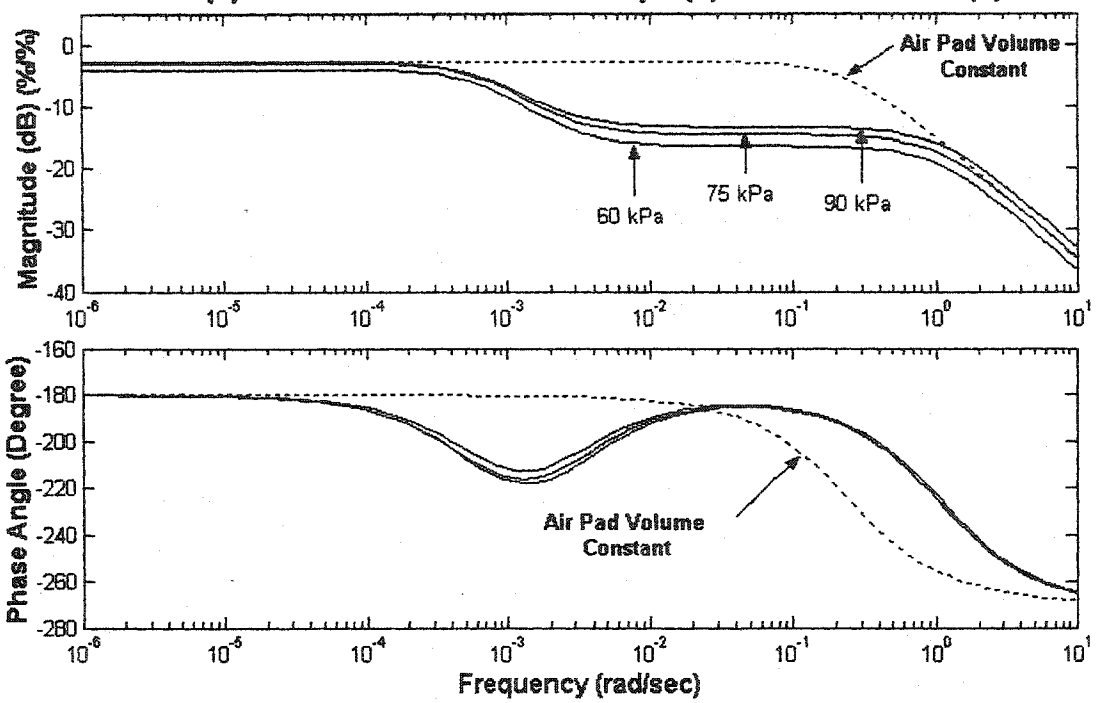

Figure 36: Weir Headbox Open-Loop Freq. Resp.
G21(s): Pressure Controller Output(s) to Stock Level(s)

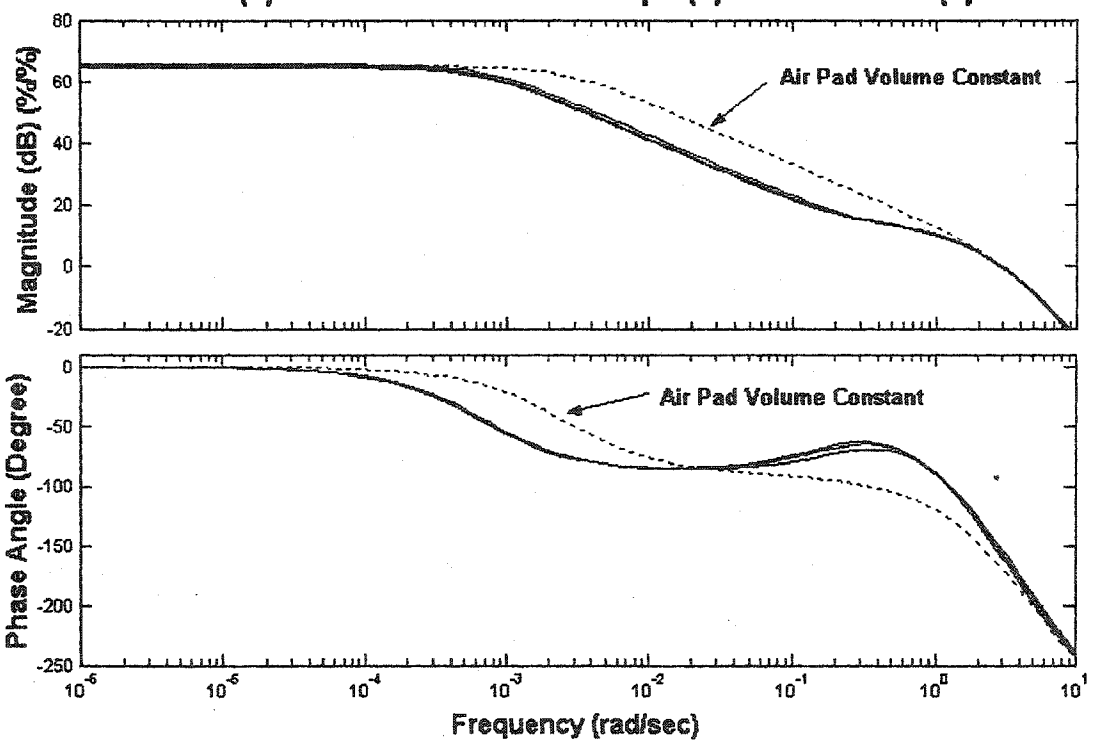

CHAPTER 4

Headbox State-Space Models

4.1 Introduction to State-Space Models

State-space models generated by EASY5™ for the hydraulic, traditional and weir headboxes at an operating point of 75 kPa are provided in this section. The state-space models enable the linearized headbox models to be simulated quickly on commercially available software such as MATLAB™. The non-linear system of equations for each headbox can be expressed in state-space form as follows:

$$\begin{aligned} \dot{x} &= Ax + Bu \\ y &= Cx + Du \end{aligned} \tag{54}$$

Where $\dot{x}$ refers to an n-dimensional state vector, y is a k-dimensional output vector and u refers to an m-dimensional input vector. A, B, C and D refer to the system stability matrix (n x n), system input matrix (n x m), system output matrix (k x n) and system feed through matrix (k x m) respectively [22]. The elements of A, B, C and D are determined from the non-linear headbox differential equations which are functions of the state variables (x), the inputs (u) and time (t). At steady-state (x_o, u_o) the elements of A, B, C and D are determined using Equations (55-58) [22]:

$$A_{ij} = \left.\frac{\partial f_i(x,u,t)}{\partial x_j}\right|_{\substack{X=X_o \\ U=U_o}} \tag{55}$$

$$B_{ij} = \left.\frac{\partial f_i(x,u,t)}{\partial u_j}\right|_{\substack{X=X_o \\ U=U_o}} \tag{56}$$

$$C_{ij} = \left.\frac{\partial y_i}{\partial x_j}\right|_{\substack{X=X_o \\ U=U_o}} \tag{57}$$

$$D_{ij} = \left.\frac{\partial y_i}{\partial u_j}\right|_{\substack{X=X_o \\ U=U_o}} \tag{58}$$

To verify that the state-space models generated by EASY5™ are correct, C++ source code was created to linearize the differential equations pertaining to each headbox model. To calculate the partial derivatives expressed in these equations, at steady-state the initial value of

the derivative vector ($\dot{x}_{INITIAL}$) is calculated ($\dot{x}_{INITIAL} \approx 0$). The first column of matrix A for example is then determined by perturbing the first state variable by a small amount, λ (1% or less) and then recalculating the derivative vector ($\dot{x}$) after the perturbation. Subtracting the derivative vector before and after the perturbation and then dividing the difference by λ calculates the first estimate of the partial derivatives (i.e. ($\dot{x}_{INITIAL}$ - $\dot{x}$)/λ). The partial derivatives are then recalculated using half the perturbation size (i.e. $\lambda=\lambda/2$). The root mean squared error (rms) between the first and second approximation is calculated. If the rms is less than a specified tolerance level ($1.0\text{x}10^{-6}$ was selected) the algorithm proceeds to the next state variable. If it is not than the procedure is repeated by halving the perturbation size until the rms is less than the tolerance level.

To calculate matrix B a similar approach is used except that the input variables are perturbed one at a time instead of the state variables. Matrix C is determined by simply placing coefficients in the cells of matrix C which when multiplied by the state vector (x) will generate the desired output variables (y). The coefficients of matrix D are all zero since there is no direct relationship between the input and output variables.

The state-space models could then be used to calculate the open or closed-loop frequency responses. In this thesis all the frequency responses generated by EASY5™ were verified in this manner.

4.2 Hydraulic Headbox State-Space Model

The elements of the state, input and output vectors x, u and y expressed in terms of deviations variables (δ) for the hydraulic headbox are stated as follows:

$\delta x = [\delta H_{LIP}$ (m), δP_{ATT} (Pa), δQ_{PUMP} (m^3/s), δW_{PUMP} (rad/s), δI_A (A), $\delta C1$ (%), $\delta C2$ (%), $\delta C3$ (%)$]^T$

$\delta u = [\delta$*Pressure Controller Output* (%)$]$

$\delta y = [\delta P_{LIP}$ (Pa)$]$

The matrices of Equation (54) determined using EASY5™ for the hydraulic headbox at an operating point of 75 kPa are:

$$A = \begin{bmatrix} -11.85 & 1.07x10^{-3} & 3.26x10^{-2} & 0 & 0 & 0 & 0 & 0 \\ -2.39x10^{4} & 1.87x10^{-3} & 4.44x10^{5} & 0 & 0 & 0 & 0 & 0 \\ 6.93x10^{-6} & -1.79x10^{-5} & -3.458 & 0.1308 & 0 & 0 & 0 & 0 \\ 0 & 0 & -15.83 & -0.7831 & 6.97x10^{-2} & 0 & 0 & 0 \\ 0 & 0 & 0 & -6326 & -8.907 & 0 & 0 & 0 \\ 0 & 0 & 0 & 0 & 0 & 0.4084 & 0 & 0 \\ 0 & 0 & 2.40x10^{-7} & 0 & 0 & 4.12x10^{-2} & -4.27x10^{-2} & 0 \\ 0 & 0 & 0 & 0 & 0 & 0 & 0.3246 & -0.3246 \end{bmatrix}$$

$$B = \begin{bmatrix} 0 & 0 & 0 & 0 & 6073 & 0 & 0 & 0 \end{bmatrix}^T$$

$$C = \begin{bmatrix} 9869 & 0 & 0 & 0 & 0 & 0 & 0 & 0 \end{bmatrix}$$

$$D = \begin{bmatrix} 0 \end{bmatrix}$$

Figure 37 illustrates the open-loop (no controller present) step response of the linearized hydraulic headbox model to a 1% change in the armature voltage of the variable speed DC motor (pressure controller output (%)). It is observed that the response is underdamped with a settling time of approximately 2 seconds. In addition the step response from the linearize model is identical to the response obtained from the non-linear model.

A 1% change in the output of the pressure controller translates to a change in armature voltage of 6.0 V (6 V/%). This causes the total pressure at the slice to increase by 3100 Pa. Therefore the steady-state gain $V_A(s)$ to $P_{LIP}(s)$ is 516.7 Pa/V, which is comparable to that determined from the non-linear step response.

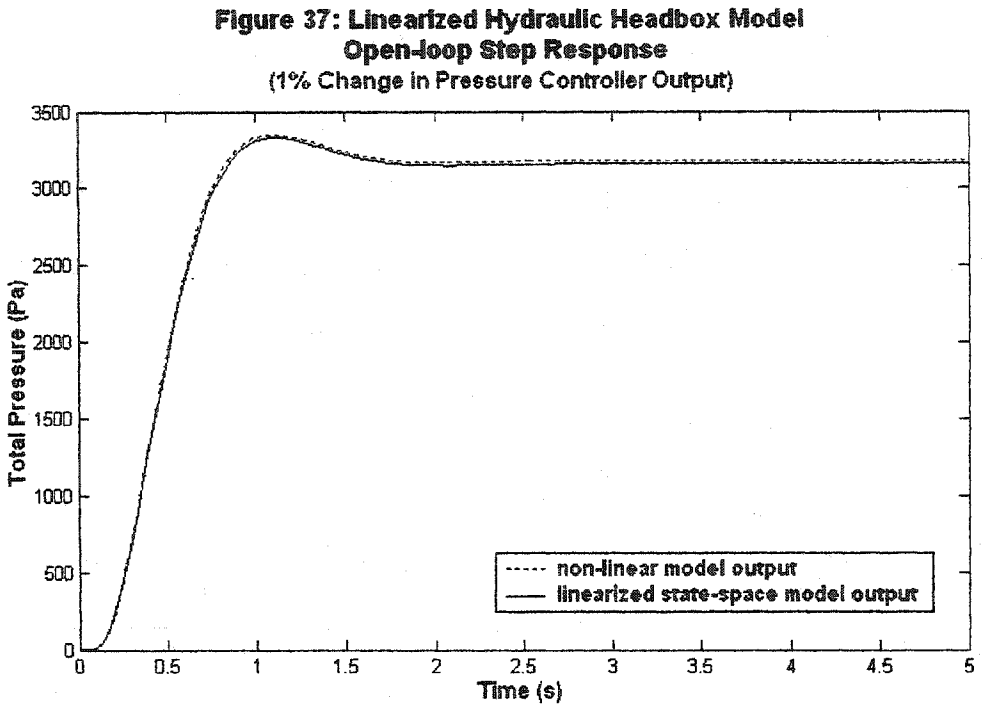

4.3 Traditional Headbox State-Space Model

The elements of the state, input and output vectors x, u and y expressed in terms of deviations variables (δ) for the traditional headbox are stated as follows:

$\delta x = [\delta L_{STOCK}\,(\text{m}),\ \delta P_{AIRPAD}\,(\text{Pa}),\ \delta Q_{PUMP}\,(\text{m}^3/\text{s}),\ \delta W_{PUMP}\,(\text{rad/s}),\ \delta I_A\,(\text{A}),\ \delta C1\,(\%),\ \delta C2\,(\%),\ \delta C3\,(\%)]^T$

$\delta u = [\delta \textit{Level Controller Output}\,(\%),\ \delta \textit{Pressure Controller Output}\,(\%)]^T$

$\delta y = [\delta L_{STOCK}\,(\text{m}),\ \delta P_{LIP}\,(\text{Pa})]^T$

The matrices of Equation (54) determined using EASY5™ for the traditional headbox at an operating point of 75 kPa are:

$$A = \begin{bmatrix} -1.28x10^{-2} & -1.29x10^{-6} & 0.2368 & 0 & 0 & 0 & 0 & 0 \\ -3579 & -0.61 & 6.65x10^{4} & 0 & 0 & 0 & 0 & 0 \\ -0.1249 & -1.27x10^{-5} & -2.585 & 9.36x10^{-2} & 0 & -7.75x10^{-4} & -8.47x10^{-4} & -8.47x10^{-4} \\ 0 & 0 & -15.59 & -0.771 & 6.97x10^{-2} & 0 & 0 & 0 \\ 0 & 0 & 0 & -6326 & -8.907 & 0 & 0 & 0 \\ 0 & 0 & 0 & 0 & 0 & -0.4084 & 0 & 0 \\ 0 & 0 & 0 & 0 & 0 & 4.12x10^{-2} & -4.27x10^{-2} & 0 \\ 0 & 0 & 0 & 0 & 0 & 0 & 0.3246 & -0.3246 \end{bmatrix}$$

$$B = \begin{bmatrix} 0 & 0 \\ -204.9 & 0 \\ 0 & 0 \\ 0 & 0 \\ 0 & 6073 \\ 0 & 0 \\ 0 & 0 \\ 0 & 0 \end{bmatrix} \qquad C = \begin{bmatrix} 1 & 0 & 0 & 0 & 0 & 0 & 0 & 0 \\ 9869 & 1 & 0 & 0 & 0 & 0 & 0 & 0 \end{bmatrix} \qquad D = \begin{bmatrix} 0 & 0 \\ 0 & 0 \end{bmatrix}$$

Figures 38 and 39 illustrate the open-loop (no controllers present) step response of the traditional headbox to a 1% change in the bleed valve position and the armature voltage (level and pressure controller outputs) respectively. In both figures it appears that there is a discontinuity in the initial total pressure transient response. If the time scale were expanded around this location there would not be a discontinuity. From Figures 38 and 39 it is also shown that the response from the linearized model is a good approximation of the non-linear response for both the level and pressure loops.

The large settling times presented in Figures 38 and 39 are a consequence of both PI controllers being placed in manual during the step changes. From Figure 38 it is observed that a 1% increase in the bleed valve position causes the stock level to increase by 0.0825 m and the total pressure to initially decrease by 210 Pa but then eventually return to initial steady-state value. The difference between the pressure increase due to the increase in stock level (0.0825 m of stock translates to 809 Pa) and the total pressure recovered after the opening of the bleed valve represents the change in the air pad pressure (210 Pa - 809 Pa = -599 Pa).

Figure 39 shows that for a 1% change in the armature voltage (pressure controller output (%)), which implies a voltage increase of 6 V, both the stock level and total pressure increase by 0.333 m and 3290 Pa respectively. Therefore the steady-state gain $V_A(s)$ to $P_{LIP}(s)$ is 548 Pa/V and $V_A(s)$ to $L_{STOCK}(s)$ is 0.056 m/V. The stock level rises as a result of the flow rate to the headbox increasing as a consequence of an increase in the armature voltage.

In the absence of feedback controllers, the strong effect of the fan pump on the stock level and total pressure and the weak effect of the bleed valve on total pressure are presented. This was also discovered through the open and closed-loop frequency responses.

Figure 38: Linearized Traditional Headbox Model
Open-Loop Step Response
(1% Change in Stock Level Controller Output)

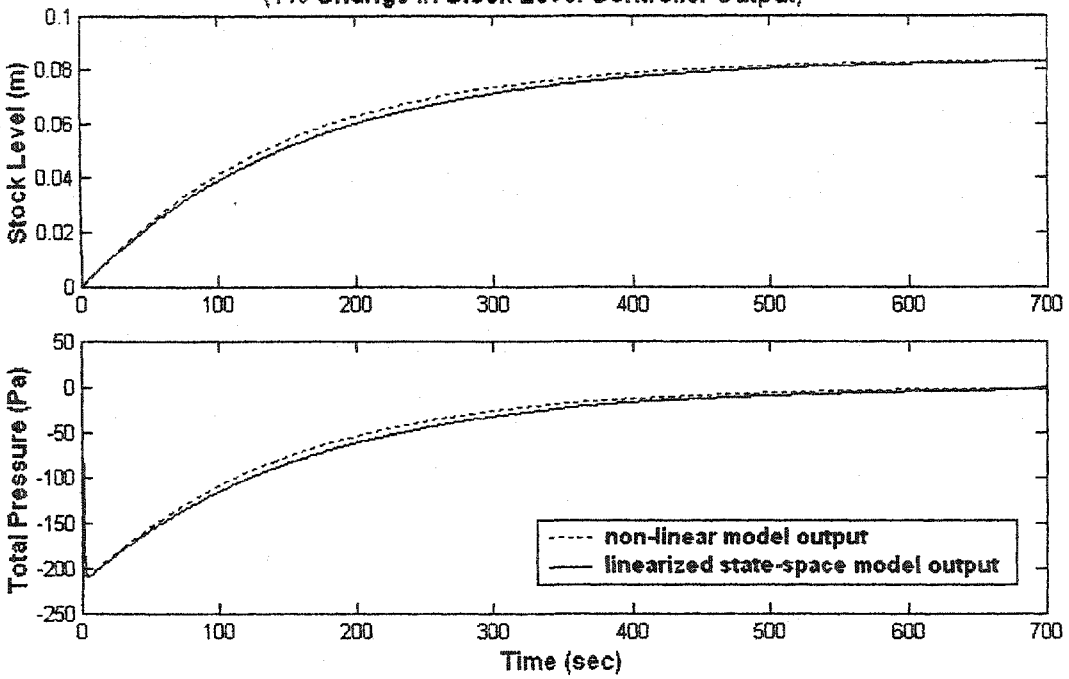

Figure 39: Linearized Traditional Headbox Model
Open-Loop Step Response
(1% Change in Pressure Controller Output)

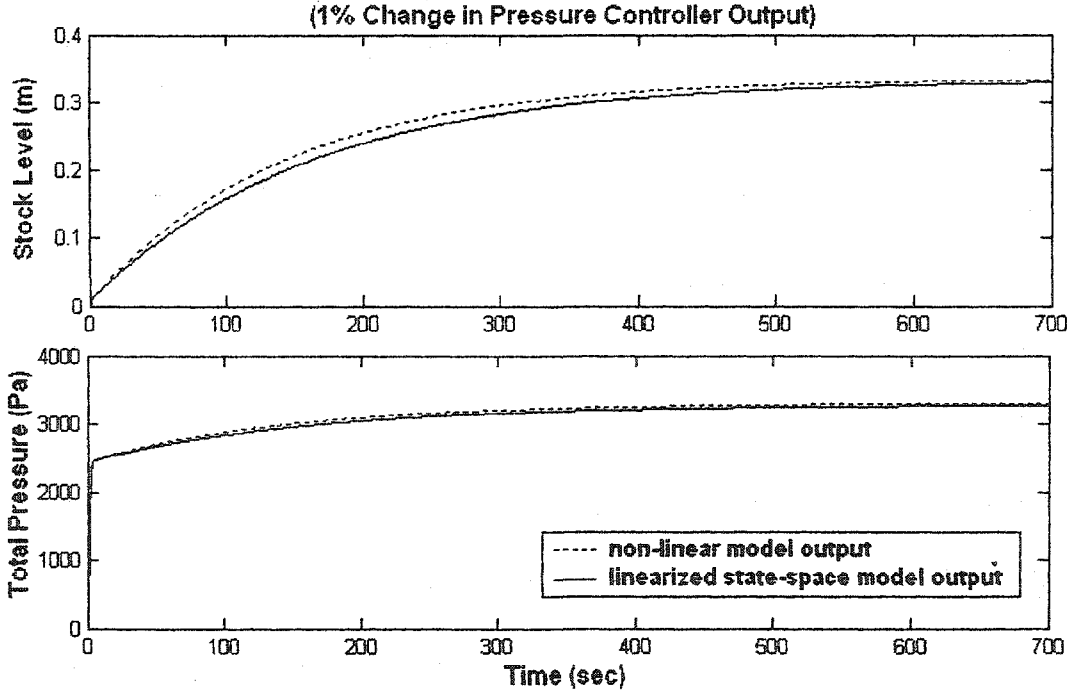

4.4 Weir Headbox State-Space Model

The elements of the state, input and output vectors x, u and y expressed in terms of deviations variables (δ) for the weir headbox are stated as follows:

$\delta x = [\delta L_{EQUAL}\,(\text{m}),\ \delta P_{AIRPAD}\,(\text{Pa}),\ \delta L_{STOCK}\,(\text{m}),\ \delta Q_{PUMP}\,(\text{m}^3/\text{s}),\ \delta W_{PUMP}\,(\text{rad/s}),\ \delta I_A\,(\text{A}),\ \delta C1\ (\%),$
$\delta C2\,(\%),\ \delta C3\,(\%)]^{\text{T}}$

$\delta u = [\delta \textit{Level Controller Output}\ (\%),\ \delta \textit{Pressure Controller Output}\ (\%)]^{\text{T}}$

$\delta y = [\delta L_{STOCK}\,(\text{m}),\ \delta P_{LIP}\,(\text{Pa})]^{\text{T}}$

The matrices of Equation (54) determined using EASY5™ for the weir headbox at an operating point of 75 kPa are:

$$A = \begin{bmatrix} -3.787 & 0 & 0 & 1.253 & 0 & 0 & 0 & 0 & 0 \\ -4975 & -0.77 & -198.7 & 6.60x10^{4} & 0 & 0 & 0 & 0 & 0 \\ 2.49 & 0 & -2.55x10^{-3} & 0 & 0 & 0 & 0 & 0 & 0 \\ -0.127 & -1.27x10^{-5} & 0 & -3.93 & 0.1185 & 0 & -1.21x10^{-3} & -1.32x10^{-3} & -1.32x10^{-3} \\ 0 & 0 & 0 & -18.7 & -1.01 & 6.92x10^{-2} & 0 & 0 & 0 \\ 0 & 0 & 0 & 0 & -6326 & -8.91 & 0 & 0 & 0 \\ 0 & 0 & 0 & 0 & 0 & 0 & -0.60 & 0 & 0 \\ 0 & 0 & 0 & 0 & 0 & 0 & 6.09x10^{-2} & -6.31x10^{-2} & 0 \\ 0 & 0 & 0 & 0 & 0 & 0 & 0 & 0.479 & -0.479 \end{bmatrix}$$

$$B = \begin{bmatrix} 0 & 0 \\ -205 & 0 \\ 0 & 0 \\ 0 & 0 \\ 0 & 0 \\ 0 & 6073 \\ 0 & 0 \\ 0 & 0 \\ 0 & 0 \end{bmatrix} \qquad C = \begin{bmatrix} 0 & 0 & 1 & 0 & 0 & 0 & 0 & 0 & 0 \\ 9869 & 1 & 0 & 0 & 0 & 0 & 0 & 0 & 0 \end{bmatrix} \qquad D = \begin{bmatrix} 0 & 0 \\ 0 & 0 \end{bmatrix}$$

Figures 40 and 41 illustrate the open-loop (no controllers present) step response of the linearized weir headbox model at an operating point of 75 kPa. Similar to the traditional headbox the discontinuity that is present for the total pressure loop is due to the selected time

scale. In both figures the initial transient response of the linear model matches that of the non-linear model. Discrepancies between the final steady-state values predicted by the linear and non-linear models are due to the presence of the overflow weir.

A 0.03% increase in the bleed valve position increases the stock level by approximately 0.09 m and decreases the total pressure by 24 Pa as illustrated in Figure 40. Compared to the traditional headbox, the level deviation without control is significant for a bleed valve change of only 0.03%. As the air pad pressure decreases, the accumulation of stock in the headbox increases since the rate of stock flow through the discharge line decrease. In addition the deviation in stock level is large as a consequence of the small cross sectional area of the headbox. A 1% change in the bleed valve position would cause the headbox to flood with stock.

The open-loop step response of the weir headbox to a 0.01% change in the pressure controller output (0.06 V) is presented in Figure 41. This causes the stock level to increase by 0.09 m and the total pressure at the slice to increase by 2.0 Pa. The size of the pressure controller output step change was changed to 0.01% so that the stock level that results from the change does not violate the headbox model (i.e. $L_{STOCK} \leq L_{WEIR}$).

Unlike the traditional headbox which once at steady-state could tolerate small changes in the input variables while both controllers are on manual without adversely effecting the control variables, the weir headbox requires at least level control. Therefore during significant grade changes, the pressure controller is usually in manual to protect the fan pump from damage, while the level controller is on automatic to prevent large deviations in stock level.

Figure 40: Linearized Weir Headbox Model
Open-Loop Step Response
(0.03% Change in Stock Level Controller Output)

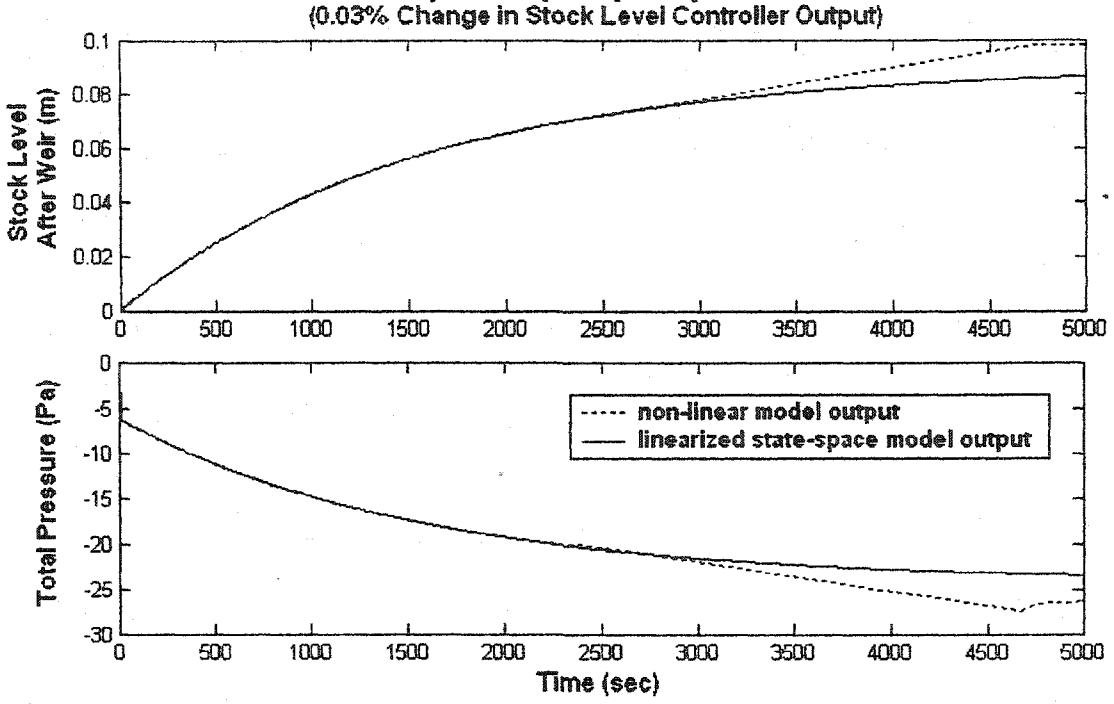

Figure 41: Linearized Weir Headbox Model
Open-Loop Step Response
(0.01% Change in Pressure Controller Output)

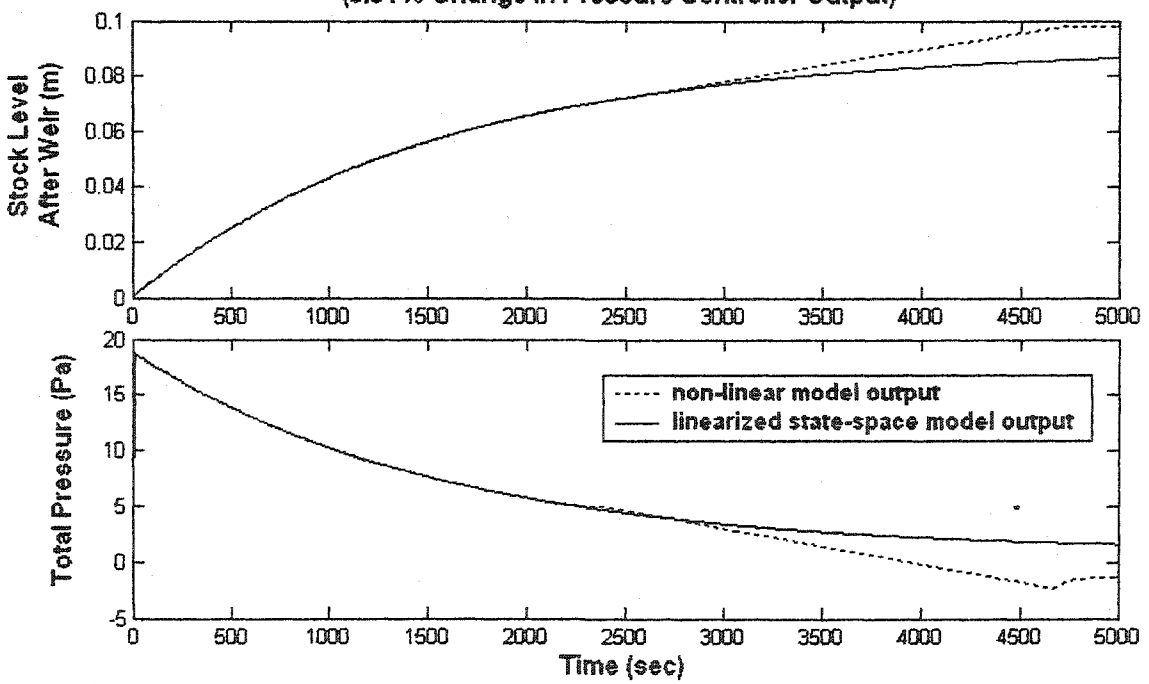

CHAPTER 5

Improving Headbox Control Through Decoupling

5.1 Introduction to Multivariable Control

The problem with the air-cushioned headbox is the issue of interaction between the level and pressure loops. The block diagram presented in Figure 42 is used to visualize the process transfer function input-output pairings that exist for the air-cushioned headbox. From Figure 42 $G_{11}(s)$ is the transfer function that relates the armature voltage, $V_A(s)$ to the total pressure at the slice $P_{LIP}(s)$. The relationship between the air-bleed valve position, $Cg(s)$ and the stock level $L_{STOCK}(s)$ is given by $G_{22}(s)$. Interaction between control loops is observed by the presence of the process gains $G_{12}(s)$ and $G_{21}(s)$. Where $G_{12}(s)$ relates the air-bleed valve position, $Cg(s)$ to the total pressure at the slice, $P_{LIP}(s)$ and $G_{21}(s)$ relates the armature voltage $V_A(s)$ to the controlled stock level $L_{STOCK}(s)$. Mathematically the relationship between input and output variables with one disturbance $D(s)$ as shown in Figure 42, can be represented in matrix form as follows [23]:

$$\begin{bmatrix} CV_1(s) \\ CV_2(s) \end{bmatrix} = \begin{bmatrix} G_{11}(s) & G_{12}(s) \\ G_{21}(s) & G_{22}(s) \end{bmatrix} \begin{bmatrix} MV_1(s) \\ MV_2(s) \end{bmatrix} + \begin{bmatrix} G_{d1}(s) \\ G_{d2}(s) \end{bmatrix} D(s) \tag{59}$$

If N number of disturbances are considered for a 2 x 2 system than $D(s)$ becomes a vector with elements $D_1(s), D_2(s) \ldots D_N(s)$ and vector $G_d(s)$ becomes a matrix with size 2 x N.

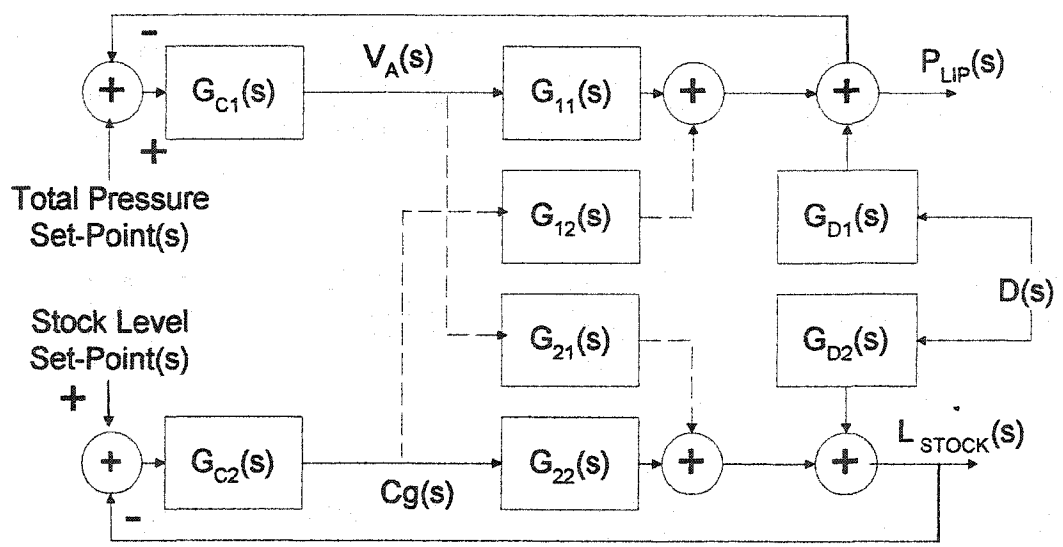

Figure 42: Block Diagram of a 2 x 2 MIMO System With Interaction

5.2 The Relative Gain Array

The Relative Gain Array (RGA) developed by Bristol (1966) and extended by Shinskey (1988) and McAvoy (1983) [23] can be used to quantitatively measure the degree of interaction. The RGA is the ratio of the open-loop to closed-loop gains of the system expressed in matrix form as is shown in Equation (60).

$$\lambda_{ij} = \frac{\left(\frac{\partial CV_i}{\partial MV_j}\right)_{OTHER\ LOOPS\ OPEN}}{\left(\frac{\partial CV_i}{\partial MV_j}\right)_{OTHER\ LOOPS\ CLOSED}} \tag{60}$$

Where λ_{ij} refers to the RGA element row i, column j, CV_i is the control variable ($P_{LIP}(s)$, $L(s)$) and MV_j represents the manipulated variable ($V_A(s)$, $Cg(s)$). If the steady-state gains K_{11}, K_{12}, K_{21} and K_{22} relating to process transfer functions $G_{11}(s)$, $G_{12}(s)$, $G_{21}(s)$, $G_{22}(s)$ respectively are known at a specific operating point, then the first element λ_{11} ($V_A(s)$ to $P_{LIP}(s)$) for a 2 x 2 system is determined as follows:

$$\lambda_{11} = \frac{1}{1 - \frac{K_{12}K_{21}}{K_{11}K_{22}}} \tag{61}$$

Since the columns and rows of the RGA must sum to 1.0, for a 2 x 2 system the RGA is simply:

$$RGA = \begin{array}{c|cc} & MV_1 & MV_2 \\ \hline CV_1 & \lambda_{11} & 1-\lambda_{11} \\ CV_2 & 1-\lambda_{11} & \lambda_{11} \end{array} \tag{62}$$

From Equation (61) it is shown that if either K_{12} or K_{21} were small or zero then λ_{11} would approach 1.0 meaning that no interaction exists and the process gain is unaffected by the other control loops [23]. As a result the greater the deviation that the relative gain is from 1.0 (either greater than or less than 1.0), the larger the interaction that exists. The relative gain array values can be used to suggest the best possible loop pairing that will achieve the best possible performance.

To access the frequency dependency on the RGA, Witcher and McAvoy (1977) concluded that this could be accomplished by replacing the steady-state gains by their corresponding transfer functions [23]. The magnitude of the RGA at different frequencies can be calculated using Equation (63) by making the substitution $s = jw$.

$$\lambda_{11}(s) = \frac{1}{1 - \dfrac{G_{12}(s)G_{21}(s)}{G_{11}(s)G_{22}(s)}} \tag{63}$$

From an analysis of the dynamic models pertaining to the pressurized headboxes, it is apparent that determination of the transfer functions $G_{11}(s) - G_{22}(s)$ would be quite difficult. To determine the transfer functions experimentally both controllers are placed on manual, a bump test on one of the input variable (armature voltage, bleed valve position) is performed and the response of the two output variables recorded.

For most systems a First-Order-Plus-Dead-Time (FOPDT) transfer function as given in Equation (64) could be used to approximate the dynamics of the system.

$$\frac{Y(s)}{X(s)} = \frac{K_P e^{-\theta s}}{\tau s + 1} \tag{64}$$

Where $Y(s)$ and $X(s)$ represent the output and input variables. Kp, τ and θ refer to the steady-state gain, process time-constant and process dead-time respectively.

The coefficients pertaining to Equation (64) could be determined from the process reaction curve using a graphical technique provided by Ziegler and Nichols (1942) or by statistical model identification methods [23]. The problem with the above procedure is that in some cases a FOPDT model is not able to approximate the dynamics of the system over a large range of frequencies. In addition by temporarily opening the closed-loop and obtaining the open-loop responses directly could result in the open-loop response containing low-frequency disturbances. Also in most processes it is not possible to arbitrarily place both or even one controller on manual to obtain the required process information. As a result the solution is to obtain the open-loop transfer functions $G_{11}(s) - G_{22}(s)$ from the closed-loop transfer functions $T_{11}(s) - T_{22}(s)$. The elements of the closed-loop transfer function matrix $T(s)$ relate the set-point $R(s)$ to the corresponding process control variable $CV(s)$. For a simple single-input, single-output (SISO) system the open-loop transfer function $G(s)$ can be determined from the closed-loop and controller transfer functions, $T(s)$ and $C(s)$ respectively as follows:

$$G(s) = \frac{T(s)}{1 - T(s)} \frac{1}{C(s)} \tag{65}$$

Expanding the idea of the SISO system to the multiple-input, multiple-output (MIMO) system, the open-loop transfer functions are determined using Equation (66) [27].

$$G(s) = \left[I - T(s)\right]^{-1} T(s)\left[C(s)\right]^{-1}$$

$$\Downarrow \tag{66}$$

$$\begin{bmatrix} G_{11}(s) & G_{12}(s) \\ G_{21}(s) & G_{22}(s) \end{bmatrix} = \left[\begin{bmatrix} 1 & 0 \\ 0 & 1 \end{bmatrix} - \begin{bmatrix} T_{11}(s) & T_{12}(s) \\ T_{21}(s) & T_{22}(s) \end{bmatrix}\right]^{-1} \begin{bmatrix} T_{11}(s) & T_{12}(s) \\ T_{21}(s) & T_{22}(s) \end{bmatrix} \begin{bmatrix} C_1(s) & 0 \\ 0 & C_2(s) \end{bmatrix}^{-1}$$

A complete explanation of how to obtain Equation (66) is provided in Appendix A.5.

The process gains $G_{11}(s)$ to $G_{22}(s)$ can then be used to quantitatively measure the degree of interaction between the pressure and level loops using the frequency dependent relative gain outlined in Equation (63). Figure 43 depicts the interaction that exists between feedback control loops. From Equation (62) it is found that the relative gain array element $\lambda_{11}(s)$ relates the manipulated to control variable pairings of the DC motor armature voltage to the total pressure at the slice ($V_A(s)$ to $P_{LIP}(s)$) and the air bleed valve position to the stock level ($Cg(s)$ to $L_{STOCK}(s)$). From Figure 43 it is shown that at the lowest frequency plotted the magnitude of $\lambda_{11}(s)$ is approximately 1.0 and 0.038 for the traditional and weir headboxes respectively.

For the traditional headbox a relative gain of 1 would indicate that at frequencies below 1.0×10^{-3} rad/s there is no interaction between the level and pressure control loops. As a result a change in $V_A(s)$ would only be transmitted to $P_{LIP}(s)$ through the process gain $G_{11}(s)$ [23]. A relative gain of 1 doesn't exclude the possibility of one-way interaction where one of the manipulated variables affects the other loops controlled variable. From Equation (63) it is shown that if the product $G_{12} \times G_{21}$ were small than the relative gain would approach 1. From the open-loop frequency responses (Figures 31, 32, 35 and 36) it was determined that it is G_{12} (*bleed valve(s) to total pressure(s)*) that causes the product $G_{12} \times G_{21}$ to be small. The relative gain array also indicates that the appropriate loop pairing as illustrated in Figure 42 is being used since the preferred pairing occurs when $\lambda_{11} \rightarrow 1$ [23].

For the weir headbox a relative gain of only 0.038 at low frequencies would indicate strong interaction between the pressure and level control loops. The relative gain also suggests that the loop pairing illustrated in Figure 42 is inappropriate. In contrast at intermediate frequencies (1.0×10^{-3} to 1.0 rad/s) the relative gain is approximately 0.74. At this point although interaction between control loops still exists, the loop pairing illustrated in Figure 42 is now possible. Regardless of the value of λ_{11} this loop pairing is used because only the fan pump can supply stock to the headbox. The downside is that total head control will not work unless level control is on with this loop pairing.

As a result of interaction between control loops, tuning of both loops must occur simultaneously as conducted in this thesis. One-way decoupling is a way of improving the closed-loop performance of the level loop by the introduction of decoupler D_{21} that adjusts the bleed valve position appropriately to compensate for the effects of interaction through the process gain G_{21}.

Figure 43: Relative Gain Element h11(s) at Various Frequencies

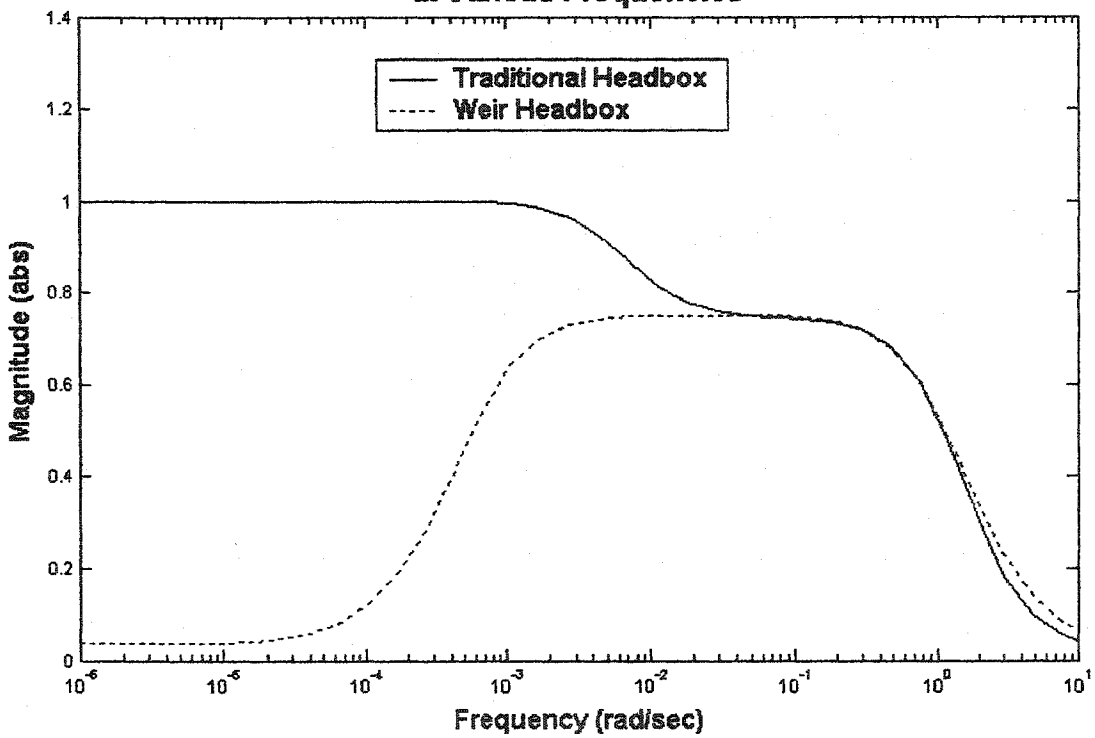

5.3 Improving Multi-loop Control by Decoupling

For MIMO systems where unfavourable interaction restricts the control performance that can be obtained in each SISO loop, interaction that limits the effectiveness of each control loop can be reduced through decoupling. Decoupling uses the concepts developed for feedforward control and extends them to the MIMO system. With the addition of feedforward control, the feedback controller output is adjusted to compensate for disturbances that may enter and upset the system. Figure 44 illustrates the modified 2 x 2 MIMO system with 2-way decoupling present.

With decoupling in the MIMO case, each loop is considered to be a potential disturbance on the other loop. Performing a RGA as discussed previously could assess the justification for the addition of decouplers. In the case of implementing decoupling to improve headbox control, an extra correction signal minimizes level deviations resulting from changes in total head control [28]. As a result quicker total head set-point changes will be possible since stock level deviations that limit how fast a total head change can occur will be decreased.

Although in principle it is possible for decoupling to completely eliminate unfavourable interaction, improper use of decoupling could lead to loop instability and performance degradation. As a result one-way rather than two-way decoupling is the preferred choice in industrial applications. The decoupler that isolates the most important control variable and improves its performance will be solely implemented.

In the case of the air-cushioned headbox, D_{21} is required since it should reduce the interaction imposed on the level loop by the pressure loop through $G_{21}(s)$ as shown in Figure 44. The ideal decoupling transfer function $D_{21}(s)$ can be calculated directly from the open-loop process gains as follows [22]:

$$D_{21}(s) = -\frac{G_{21}(s)}{G_{22}(s)} \tag{67}$$

Process gains $G_{21}(s)$ and $G_{22}(s)$ are obtained from the closed-loop transfer functions $T_{11}(s)$, $T_{12}(s)$, $T_{21}(s)$ and $T_{22}(s)$ using Equation (66).

Equation (67) was used to calculate the theoretical decoupling frequency response $D_{21}(s)$ presented in Figures 45-46 for the traditional and weir headboxes. The lead / lag compensator presented in Equation (68) was used to approximate the ideal decoupling frequency response.

$$D_{21}(s) = -\frac{G_{21}(s)}{G_{22}(s)} = -K\frac{1+\tau_{LEAD}s}{1+\tau_{LAG}s} \tag{68}$$

Where K refers to the lead / lag compensator steady-state gain, τ_{LEAD} refers to the numerator time constant (sec.) and τ_{LAG} represents the denominator time constant (sec.). A lead / lag compensator is preferred for practical applications since it is easy to program on a DCS and has only 3 parameters to tune.

Equations (69) and (70) are the lead/lag decoupler transfer function ($D_{21}(s)$) used to approximate the ideal decoupler frequency responses of the traditional and weir headboxes respectively.

$$\textit{Traditional headbox: } D_{21}(s) = -3.98\frac{1+4.0s}{1+0.8s} \tag{69}$$

$$\textit{Weir headbox: } D_{21}(s) = -3.04\frac{1+4.25s}{1+0.85s} \tag{70}$$

The steady-state gain K was determined by the gain of the ideal decoupler at the lowest frequency presented in Figure 46. The decoupler time constant τ_{LEAD} was obtained by approximating the corner frequency of the ideal decoupler frequency response. To limit derivative amplification and actuator wear, the lag time constant τ_{LAG} is calculated from τ_{LEAD} by the following equation:

$$5.0\,\tau_{LAG} \geq \tau_{LEAD} \tag{71}$$

Figures 45 and 46 illustrate the lead / lag decoupler frequency responses superimposed on the ideal decoupler frequency response for the traditional and weir headboxes respectively. It is shown that at frequencies below 0.1 rad/s the lead/lag compensator is similar to the ideal decoupler frequency response for both headboxes. To better fit the ideal decoupler frequency response at frequencies above 0.1 rad/s, the ratio between lead to lag time constants would have to be increased to approximately $10\,\tau_{LAG} \geq \tau_{LEAD}$. With the decoupler transfer function presented in Equations (69) and (70), a +1% step change in the pressure controller output (input to decoupler D_{21}) causes the output of the decoupler to initially deviate by approximately –19.9 % and –15.2 % respectively.

With the lead / lag compensator applied as shown in Figure 44 the closed-loop frequency response that can be expected for the traditional headbox is presented in Figure 47. With the lead/lag compensator a reduction in the closed-loop gain $T_{21}(s)$ is observed for the frequency range plotted. Similar results are observed in Figure 48 for the closed-loop frequency response pertaining to the weir headbox with one-way decoupling. For both headboxes a slight increase in the total pressure closed-loop bandwidth and the absence of a resonant peak is illustrated with the addition of $D_{21}(s)$. This implies that the response of the pressure loop to a pressure set-point change shouldn't be underdamped. In addition at frequencies above 1.0 rad/s a reduction in the cross gain $T_{12}(s)$ is also present.

The response of each headbox to a ± 1% set-point change in total head (1100 Pa) before and after the addition of decoupler D_{21} is presented in Figures 49 and 50 for the traditional and weir headboxes respectively. Each headbox was simulated with the same feedback gains

presented in Table 3. For both headboxes the level controller responds to the pressure set-point change by opening or closing the bleed valve more than it did without the decoupler. The response of the pressure loop to the pressure set-point change is changed from previously being underdamped to being overdamped as predicted from the closed-loop frequency responses. The settling times of both the level and pressure loops remain the same but a significant reduction in the deviations of the controlled level is observed. The maximum stock level deviations of the traditional and weir headboxes are reduced by approximately 5.2 and 4.7 times over the simulated resulted obtained prior to the inclusion of the decoupler.

This section proved that the control performance of the level loop of an air-cushioned headbox could benefit from the addition of one-way decoupling. By improving the performance of the level control loop stock level deviations are reduced thereby also improving the performance of the pressure control loop. As a result during paper grade changes the amount of off-grade paper that is generated is reduced since the fan pump can be ramped up more quickly since large fluctuations in the stock level will not occur.

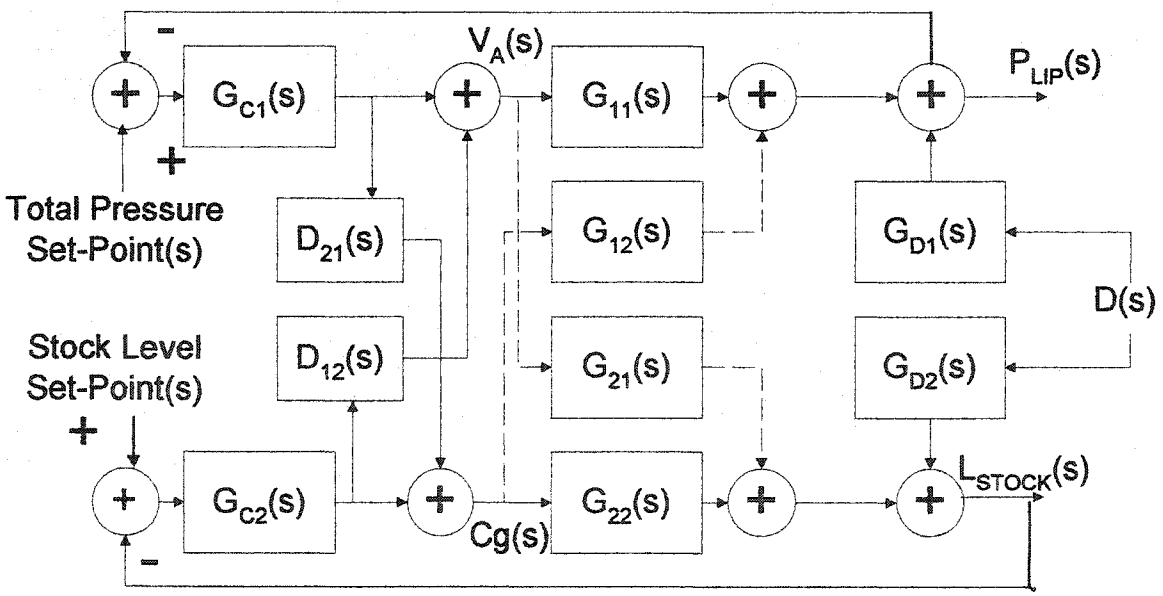

Figure 44: 2 x 2 MIMO System with 2-Way Decoupling

Figure 45: Traditional Headbox Decoupler D21(s) Freq. Resp.

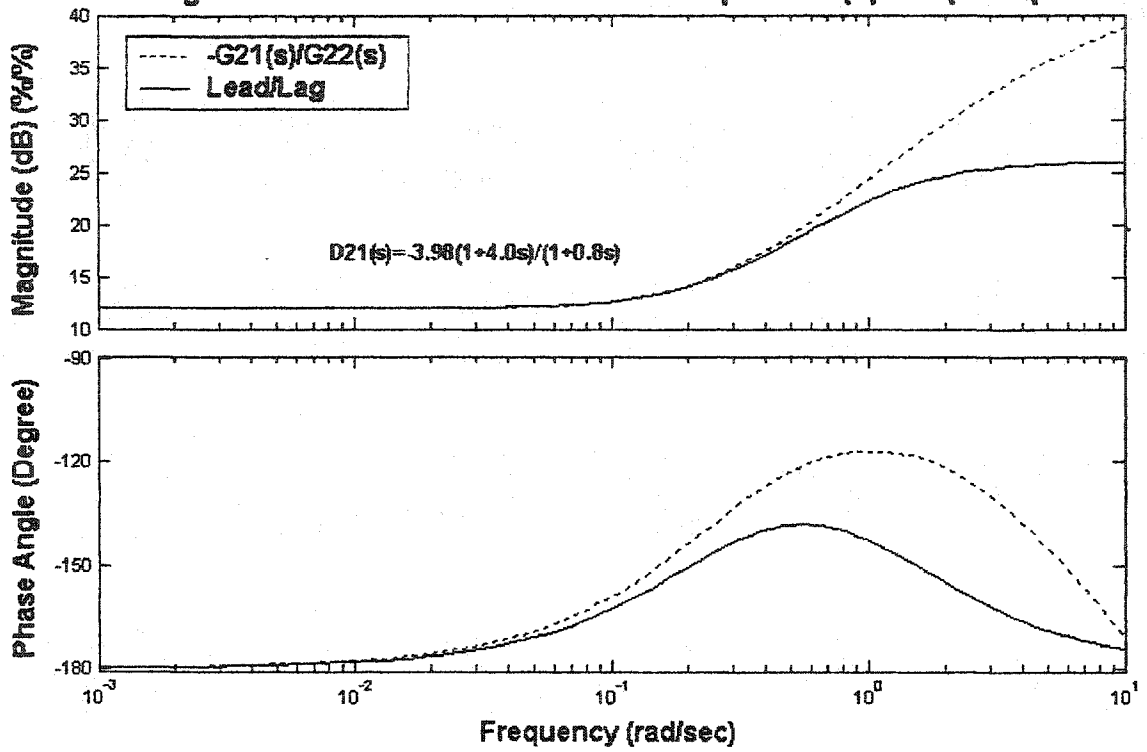

Figure 46: Weir Headbox Decoupler (D21) Freq. Resp.

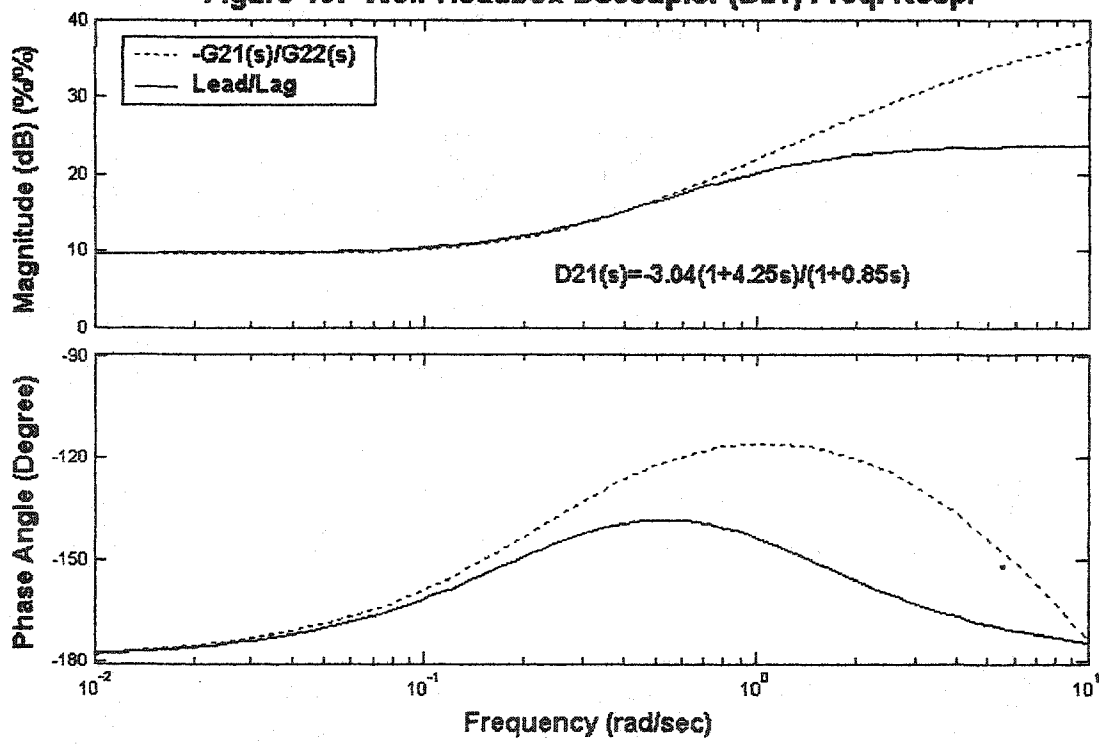

Figure 47: Traditional Headbox Closed-Loop Freq. Resp. With Decoupler D21(s)=-3.98*(1+4s)/(1+0.8s)

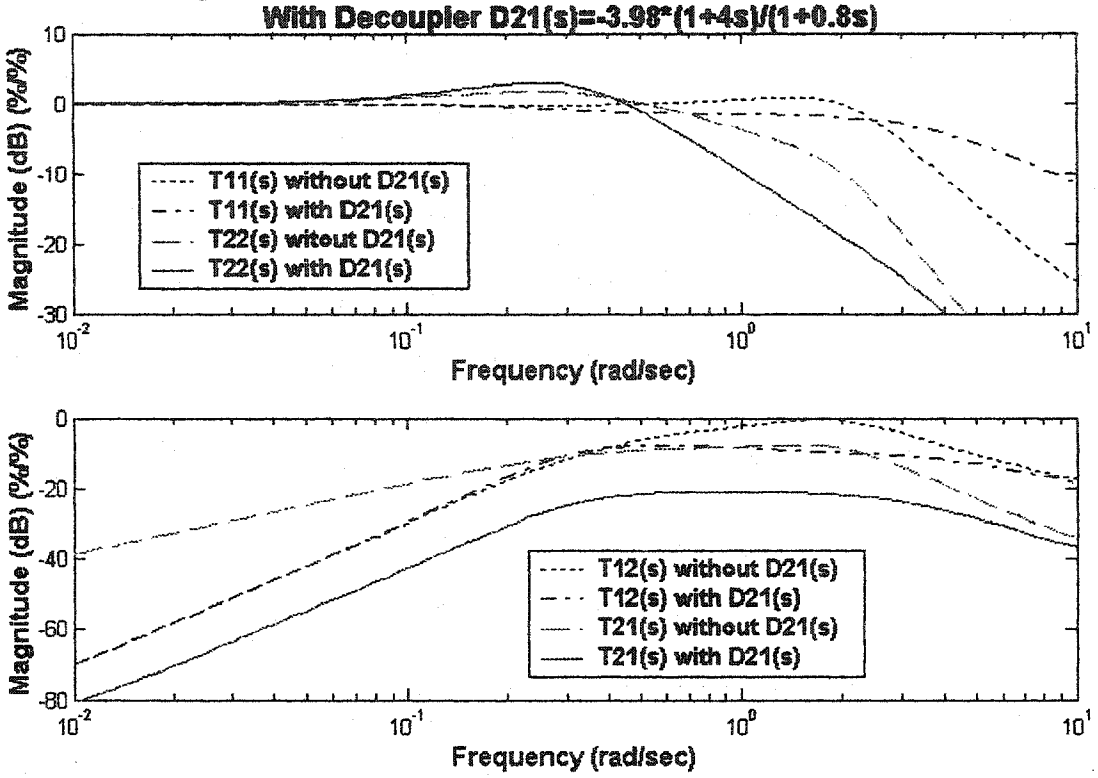

Figure 48: Weir Headbox Closed-Loop Freq. Resp. With Decoupler D21(s)=-3.04*(1+4.25s)/(1+0.85s)

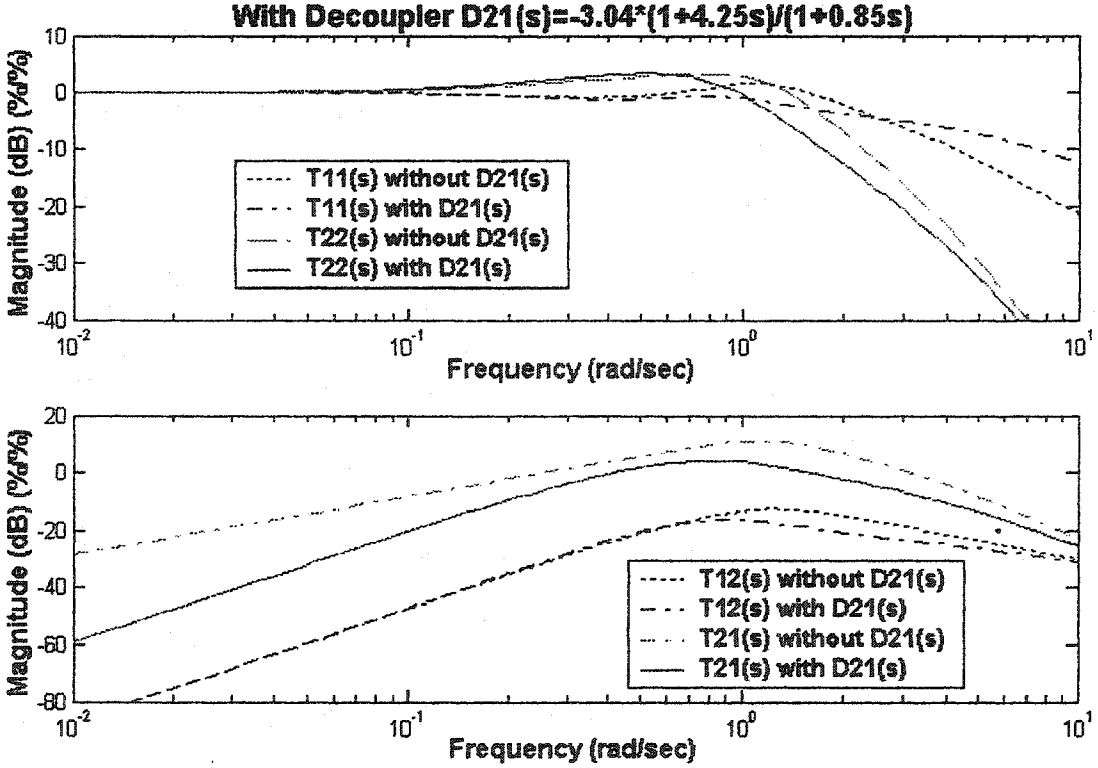

Figure 49: Traditional Headbox: Set-Point Change in Total Head With Decoupler D21

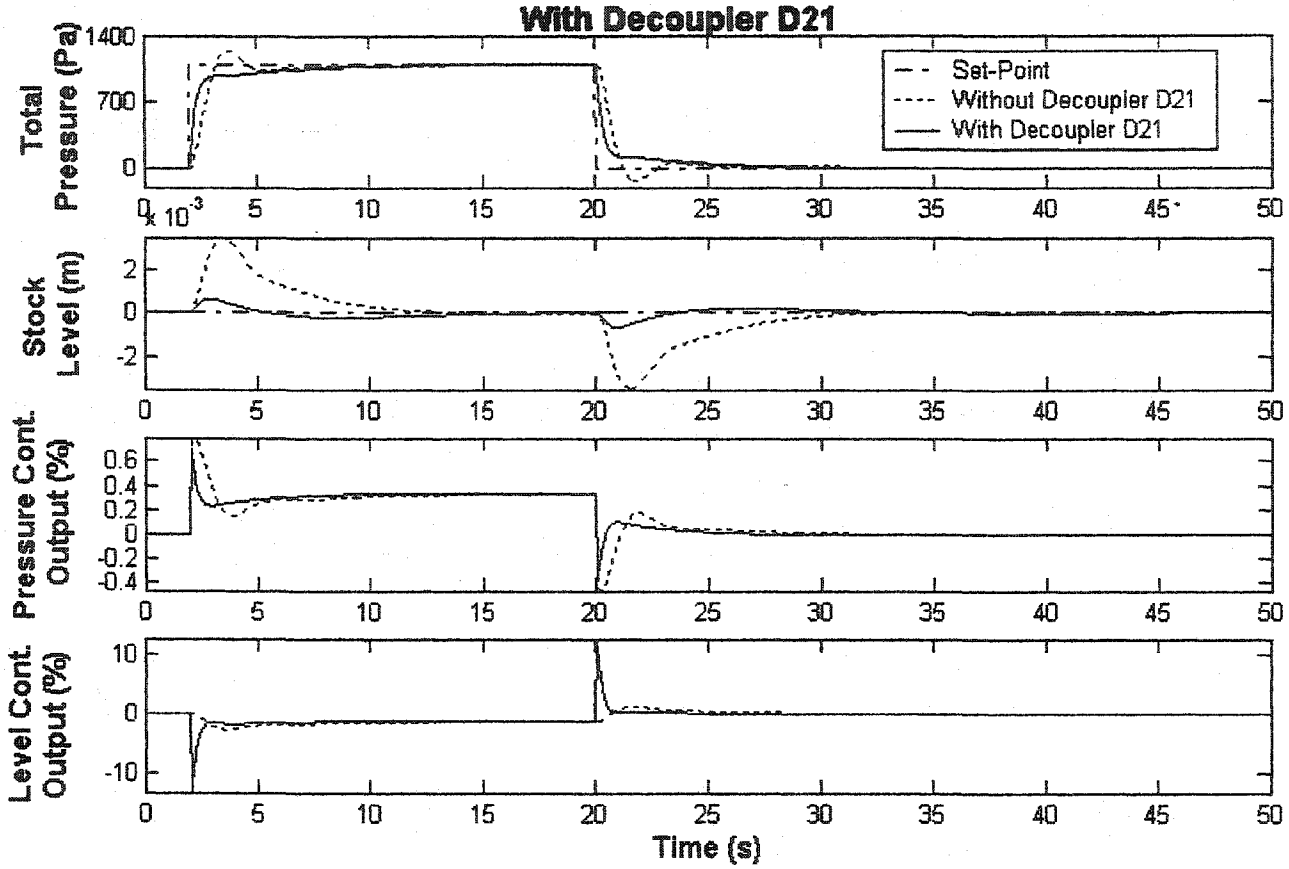

Figure 50: Weir Headbox: Set-Point Change in Total Head With Decoupler D21

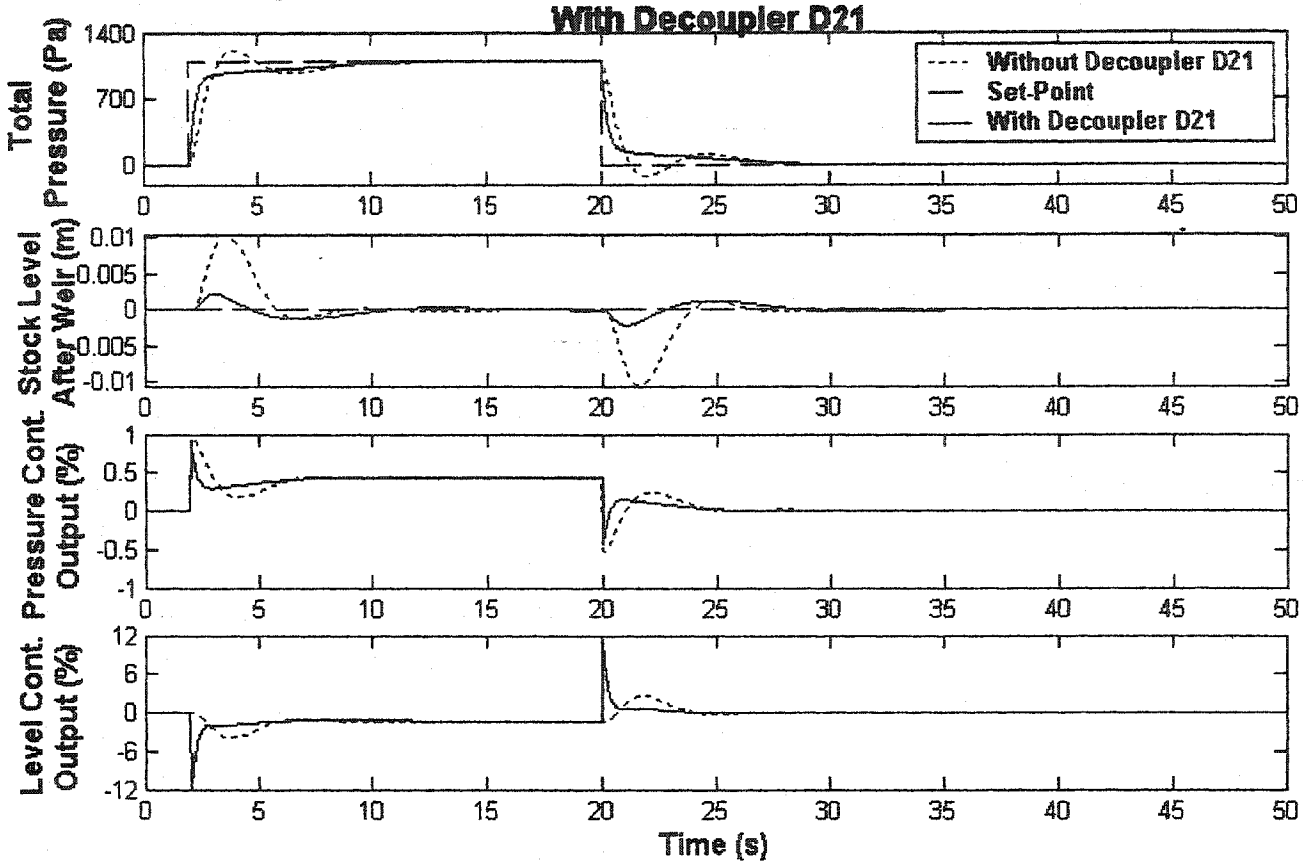

CHAPTER 6

Conclusions

In this thesis complete models of a hydraulic and two air-cushioned (traditional, weir) headboxes were presented. The headbox models were limited to surge flow models that are capable of predicting the behaviour of the system for frequencies less than 10 rad/s.

Tuning of all PI controller gains using the IAE performance criterion gave all headbox models an underdamped response. Step response simulations reinforced the concept that the simple hydraulic headbox requiring only 1-PI controller provided the quickest response to set-point changes in total head. In addition it was found that pressure control of an air-cushioned headbox is only possible if level control is implemented.

Interaction between the level and pressure control loops of the air-cushioned headboxes was clearly illustrated in closed-loop frequency response plots by the presence of resonant peaks located at frequencies covered by the feedback controllers. From these plots the closed-loop total pressure bandwidth was also discovered to be less than 0.5 rad/s. The closed-loop bandwidth of the level loop is further limited by the actions of the pressure loop.

Open-loop frequency responses showed the non-linear behaviour of each headbox model as a result of the dynamics of the fan pump. For the air-cushioned headboxes the effect of the bleed valve and fan pump on the stock level was found to be strong. The effect of the fan pump on total head was observed to be strong within the normal operating range of frequencies of the air-cushioned headboxes. At very low frequencies the effect of the bleed valve on total head was found to be weak for the traditional headbox and strong for the weir headbox but weak/moderate for both headboxes at intermediate frequencies.

To reduce the coupling that exists between control loops, one-way decoupling was suggested. It was found that with a lead/lag compensator stock level deviations caused by changes to the pressure loop are significantly decreased. Step and closed-loop frequency response plots illustrated that the lead/lag decoupler does not degrade the overall performance of the pressure control loop. It is concluded that the use of one-way decoupling enables the performance of the air-cushioned headbox to approach that of the hydraulic headbox. This is possible since stock level deviations that previously limited how fast a pressure set-point change could occur have been reduced. The economic benefits of being able to make quicker pressure set-point changes are that the amount of off-grade paper made is decreased.

APPENDIX A

Derivation of Model Equations

Appendix A.1 - Derivation of Equation (16)

$$\frac{d}{dt}Q_{PUMP} = g\left[\frac{A}{L}\right]\left[H_{PUMP} - H_{STATIC} - H_{LIP} - f_1 Q_{INT}^{\ 2}\right] \quad (16)$$

A change in volumetric flow is caused by a variation in the net force (F_{NET}) acting on the fluid in the control volume (fan pump to headbox slice). This applied net force can be determined as follows:

$$\vec{F}_{NET} = P_1 A - P_2 A - \rho g f_1 Q_{INT}^{\ 2} A \quad (16A)$$

Where P_1 and P_2 represent the pressure at the suction end of the fan pump (Pa) and the total pressure at the headbox slice (Pa) respectively. f_1 refers to the head loss coefficient (s^2/m^5) and A represents the effective cross sectional area of the control volume (m^2). The average volumetric flow through the control volume (m^3/s) is represented by Q_{INT}. The variables ρ and g refer to the density of fluid in the control volume (kg/m^3) and the gravitational acceleration constant (9.81 m/s^2) respectively.

The last term in the force equation relates how head loss varies with the square of the average volumetric flow through the control volume. From Newton's second law it is known that the net force acting on the fluid in the control volume will cause it to accelerate or decelerate. Therefore the right side of Equation (16A) can be expanded as follows:

$$\vec{F}_{NET} = m\vec{a} = \rho AL\frac{d\vec{v}}{dt} = \rho AL\frac{d\frac{Q_{PUMP}}{A}}{dt} \quad (16B)$$

Where m, L and v refer to the mass of fluid in the control volume (kg), the effective length of the pipe section (m) and the velocity of fluid in the control volume (m/s) respectively. Substituting the right side of Equation (16B) into (16A) yields the following equation:

$$\rho AL\frac{d\frac{Q_{PUMP}}{A}}{dt} = P_1 A - P_2 A - \rho g f_1 Q_{INT}^{\ 2} A \quad (16C)$$

Expressing the right side of Equation (16C) in terms of head of stock and separating the pressure difference P_1 - P_2 yields the following equation:

$$P_1 A - P_2 A - \rho g f_1 Q_{INT}{}^2 A = \rho g H_{PUMP} A - \rho g H_{STATIC} A - \rho g H_{LIP} A - \rho g f_1 Q_{INT}{}^2 A \quad (16D)$$

Where H_{PUMP}, H_{STATIC} and H_{LIP} refer to the net head of stock developed by the fan pump (m), the static head (elevation difference between fan pump and headbox slice (m)) and the total head at the headbox lip (m) respectively. Substituting the right side of Equation (16D) back into Equation (16C) and cancelling common terms yield Equation (16).

Appendix A.2 - Derivation of Equation (29)

Since the original Fisher Valve Equation as stated below is expressed in Imperial units, a simple conversion to S.I. units is required.

$$Q_{DISCHARGE} = C_V \sqrt{\frac{\Delta P}{G}} \quad (29A)$$

Where $Q_{DISCHARGE}$ refers to the volumetric flow of stock through the discharge valve (USGPM). ΔP represents the pressure differential (psi) across the discharge valve. G refers to the specific gravity of stock (dimensionless) whereas C_V represents the valve discharge coefficient (USGPM/psi$^{1/2}$). Expressing pressure in terms of an equivalent height of liquid, H_{TOTAL} yields the following changes to Equation (29A).

$$\Delta P = G \rho g \frac{H_{TOTAL}}{0.3048}$$

$$Q_{DISCHARGE} = C_V \sqrt{\frac{G \rho g H_{TOTAL}}{0.3048\ G}} \quad (29B)$$

$$Q_{DISCHARGE} = C_V \sqrt{\frac{\rho g H_{TOTAL}}{0.3048}}$$

The units of the variables expressed above are as follows: ρ=62.4 lb_m/ft^3, g=1.0 lb_f/ 1.0 lb_m, H_{TOTAL} (m). The constant 0.3048 referenced in Equation (29B) converts the units of H_{TOTAL} to imperial units (ft). By substituting the values of ρ, and g into Equation (29B) the following is obtained:

$$Q_{DISCHARGE} = C_V \sqrt{62.4 \frac{lb_m}{ft^3} \frac{1.0 ft^2}{144.0 in^2} \frac{1.0 lb_f}{1.0 lb_m} \frac{H_{TOTAL}}{0.3048}} \quad (29C)$$

$$Q_{DISCHARGE} = 1.19235\ C_V \sqrt{H_{TOTAL}}$$

The discharge flow, $Q_{DISCHARGE}$ is then converted to units of m^3/s as presented below to obtain Equation (29).

$$Q_{DISCHARGE} = \left[1.19235\, C_V \sqrt{H_{TOTAL}}\right] \frac{6.309x10^{-5}\ \frac{m^3}{\sec}}{1.0\ \frac{gal}{\min}} \tag{29}$$

$$Q_{DISCHARGE} = 7.52x10^{-5} C_V \sqrt{H_{TOTAL}}$$

Appendix A.3 - Derivation of Equation (35)

$$\frac{dH_{LIP}}{dt} = \frac{\sqrt{2gH_{LIP}}}{A_{LIP}\alpha}\left(\frac{A}{L}\right)_2\left[H_{INT} - H_{LIP} - 2gf_2 H_{LIP}\left(A_{LIP}\alpha\right)^2\right] \tag{35}$$

The derivation begins with Equation (34), which was stated as follows.

$$\frac{dQ_{LIP}}{dt} = g\left(\frac{A}{L}\right)_2\left[H_{INT} - H_{LIP} - f_2 Q_{LIP}{}^2\right] \tag{34}$$

Using Bernoulli's equation (Equation (19)) the derivative of flow through the slice with respect to time is determined giving Equation (35A).

$$Q_{LIP} = \alpha A_{LIP}\left[2gH_{LIP}\right]^{0.5} \tag{19}$$

$$\frac{dQ_{LIP}}{dt} = \frac{gA_{LIP}\alpha}{\sqrt{2gH_{LIP}}}\frac{dH_{LIP}}{dt} \tag{35A}$$

The left-hand side of Equation (34) is replaced by the right-hand side of Equation (35A), thereby forming Equation (35B).

$$\frac{gA_{LIP}\alpha}{\sqrt{2gH_{LIP}}}\frac{dH_{LIP}}{dt} = g\left(\frac{A}{L}\right)_2\left[H_{INT} - H_{LIP} - f_2 Q_{LIP}{}^2\right] \tag{35B}$$

Rearranging Equation (35B) and eliminating Q_{LIP} using Equation (19) gives the final form of Equation (35).

Appendix A.4 - Derivation of Equation (39)

$$\frac{dP_{ATT}}{dt} = \left[\frac{Q_{INT} - Q_{RECIRCULATION} - Q_{LIP}}{A_{ATT}}\right]\left[\frac{NK_{ATT}}{Level_{GAS}^{N+1} A_{ATT}^{N}}\right] \tag{39}$$

Using the gas law presented in Equation (36), the gas level in the attenuator (Equation (38)) can be determined by expanding the variables P and V as illustrated by Equation (39A).

$$PV^N = K_{ATT} \tag{36}$$

$$PV^N = (P_{ATT} + P_{ATM})(Level_{GAS} A_{ATT})^N = K_{ATT} \tag{39A}$$

$$Level_{GAS} = \left[\frac{1}{A_{ATT}}\right]\left[\frac{K_{ATT}}{P_{ATT} + P_{ATM}}\right]^{\frac{1}{N}} \tag{38}$$

From Equation (38) it is shown that a change in the volume of gas due to a variation in stock level will cause the gas pressure to change. This can be expressed mathematical by Equation (39B).

$$\frac{dP_{ATT}}{dt} = \frac{\partial P_{ATT}}{\partial Level_{GAS}} \frac{dLevel_{GAS}}{dt} \tag{39B}$$

The partial derivative $\partial P_{ATT}/\partial Level_{GAS}$ expressed in Equation (39B), which is determined from Equation (38) is stated as follows:

$$\frac{\partial P_{ATT}}{\partial Level_{GAS}} = \frac{-K_{ATT} A_{ATT} N}{A_{ATT}^{N+1} Level_{GAS}^{N+1}} \tag{39C}$$

A change in gas level is related to a change in stock level by the following equation:

$$\frac{dLevel_{GAS}}{dt} = -\frac{dLevel_{STOCK}}{dt} = -\frac{[Q_{INT} - Q_{RECIRCULATION} - Q_{LIP}]}{A_{ATT}} \tag{39D}$$

Substituting the right-hand sides of Equations (39C) and (39D) into Equation (39B) and eliminating common terms will give the final form of Equation (39).

Appendix A.5 – Derivation of Equation (56)

NOTE: Laplace operator s has been omitted from proof. Therefore $G_{11} \equiv G_{11}(s)$, $T_{11} \equiv T_{11}(s)$ etc.

$$G = [I - T]^{-1} T [C]^{-1}$$

$$\Downarrow \tag{56}$$

$$\begin{bmatrix} G_{11} & G_{12} \\ G_{21} & G_{22} \end{bmatrix} = \left[\begin{bmatrix} 1 & 0 \\ 0 & 1 \end{bmatrix} - \begin{bmatrix} T_{11} & T_{12} \\ T_{21} & T_{22} \end{bmatrix} \right]^{-1} \begin{bmatrix} T_{11} & T_{12} \\ T_{21} & T_{22} \end{bmatrix} \begin{bmatrix} C_1 & 0 \\ 0 & C_2 \end{bmatrix}^{-1}$$

The proof of Equation (56) will be given by first acknowledging that each element in the closed-loop matrix $T(s)$ can be derived from the 2 x 2 MIMO system provided in Figure 42. From the block diagram the elements of $T(s)$ are given as [23]:

$$T_{11} = \frac{CV_1}{SP_1} = \frac{C_1 G_{11} + C_1 C_2 [G_{11} G_{22} - G_{12} G_{21}]}{CE} \tag{56A}$$

$$T_{12} = \frac{CV_1}{SP_2} = \frac{C_2 G_{12}}{CE} \qquad T_{21} = \frac{CV_2}{SP_1} = \frac{C_1 G_{21}}{CE} \tag{56B-C}$$

$$T_{22} = \frac{CV_2}{SP_2} = \frac{C_2 G_{22} + C_1 C_2 [G_{11} G_{22} - G_{12} G_{21}]}{CE} \tag{56D}$$

Where:

$$CE = 1 + C_1 G_{11} + C_2 G_{22} + C_1 C_2 [G_{11} G_{22} - G_{12} G_{21}] \tag{56E}$$

The closed-loop transfer function in matrix notation for a MIMO system is given as:

$$T = [I + GC]^{-1} GC$$

$$\Downarrow \tag{56F}$$

$$\begin{bmatrix} T_{11} & T_{12} \\ T_{21} & T_{22} \end{bmatrix} = \left[\begin{bmatrix} 1 & 0 \\ 0 & 1 \end{bmatrix} + \begin{bmatrix} G_{11} & G_{12} \\ G_{21} & G_{22} \end{bmatrix} \begin{bmatrix} C_1 & 0 \\ 0 & C_2 \end{bmatrix} \right]^{-1} \begin{bmatrix} G_{11} & G_{12} \\ G_{21} & G_{22} \end{bmatrix} \begin{bmatrix} C_1 & 0 \\ 0 & C_2 \end{bmatrix}$$

Expanding Equation (56F) yields the following Equations:

$$\begin{bmatrix} T_{11} & T_{12} \\ T_{21} & T_{22} \end{bmatrix} = \left[\begin{bmatrix} 1 + G_{11} C_1 & G_{12} C_2 \\ G_{21} C_1 & 1 + G_{22} C_2 \end{bmatrix} \right]^{-1} \begin{bmatrix} G_{11} C_1 & G_{12} C_2 \\ G_{21} C_1 & G_{22} C_2 \end{bmatrix} \tag{56G}$$

$$\begin{bmatrix} T_{11} & T_{12} \\ T_{21} & T_{22} \end{bmatrix} = \frac{1}{CE} \begin{bmatrix} 1 + G_{22} C_2 & -G_{12} C_2 \\ -G_{21} C_1 & 1 + G_{11} C_1 \end{bmatrix} \begin{bmatrix} G_{11} C_1 & G_{12} C_2 \\ G_{21} C_1 & G_{22} C_2 \end{bmatrix} \tag{56H}$$

Where:

$$\begin{aligned} CE &= [1 + G_{22} C_2][1 + G_{11} C_1] - G_{12} C_2 G_{21} C_1 \\ \therefore CE &= 1 + G_{11} C_1 + G_{22} C_2 + C_2 C_1 [G_{11} G_{22} - G_{12} G_{21}] \end{aligned} \tag{56I}$$

Multiplying the matrices on the right side of Equation (56H) yields Equation (56J), which expresses the closed-loop transfer functions in (Equations (56A-56D)) in matrix form.

$$\begin{bmatrix} T_{11} & T_{12} \\ T_{21} & T_{22} \end{bmatrix} = \frac{1}{CE}\begin{bmatrix} G_{11}C_1 + C_1C_2\left[G_{11}G_{22} - G_{12}G_{21}\right] & G_{12}C_2 \\ G_{21}C_1 & G_{22}C_2 + C_1C_2\left[G_{11}G_{22} - G_{12}G_{21}\right] \end{bmatrix} \quad (56J)$$

Equation (56) is obtained by performing the following mathematical operations to Equation (56F):

$$T = \left[I + GC\right]^{-1}GC \quad (56F)$$

$$T\left[I + GC\right] = \left[I + GC\right]^{-1}\left[I + GC\right]GC$$

$$T + TGC = GC$$

$$\left[I - T\right]^{-1}TC^{-1} = G \quad (56)$$

APPENDIX B

Model of an Air Chamber Attenuator With Diaphragm

An air chamber attenuator with a diaphragm as shown in Figure 51 could be used to provide acceptable damping of stock surges. The properties of the diaphragm will determine the bandwidth of frequencies that will be attenuated. The attenuator works on the principle that the movement of the diaphragm will be out of phase with the disturbance (stock surge) thereby effectively cancelling out the unwanted disturbance. Applying acoustic-mechanical analogy to the attenuator enables an estimate of the natural frequencies that will be attenuated based on the physical description of the attenuator to be calculated [17]. The dynamic equations for the attenuator will be developed using the analogy of a spring system as pictured in Figure 52. The small volume of stock between the diaphragm and main pipe section and the physical mass of the diaphragm will be representative of the mass of the spring in the mechanical system. The mechanical capacitance of the spring, C_M (inverse of the spring constant) will be a function of the air pressure above the diaphragm. Assuming that the outer perimeter of the diaphragm is held rigidly in place and only the inner section of the diaphragm can deform, then the mechanical resistance, R_M will be a function of the modulus of the material selected. The following second-order differential equation pertaining to a mechanical spring system will provide the basis for the air chamber type attenuator [8].

$$F_{NET} = M_T \frac{d^2X}{dt^2} + R_M \frac{dX}{dt} + \frac{X}{C_M} \tag{72}$$

Where F_{NET} refers to the net force acting on the diaphragm (N), M_T is the total mass of diaphragm and the mass of fluid "plug" in the attenuator neck section (kg), R_M is the mechanical resistance (N·s/m), C_M represents the mechanical capacitance (N/m) and X is the centreline position of diaphragm (m). It is assumed that the mass of fluid in the neck of the attenuator moves as though it was a solid plug [17]. Also the variable X is assumed to be the deviation of the centreline position of the diaphragm from its steady-state position. The mass of the "plug" of fluid and diaphragm can be calculated as follows:

$$M_T = X_O \rho A_N + M_{MEM} \tag{73}$$

Where X_0 is the height of fluid in attenuator "neck" (m), A_N refers to the cross-sectional area of piping section into attenuator (m^2), M_{MEM} is the mass of the attenuator diaphragm (kg) and ρ represents the density of stock (kg/m^3).

A force balance around the attenuator system is used to determine the net force acting on the membrane. Movement of the membrane could be a result of a change in air pressure above the attenuator membrane or due to a stock fluctuation across the entrance to the attenuator. Equation (74) can be used to determine the net force acting on the membrane.

$$F_{NET} = \frac{\rho}{A_N}\left[Q_{INT} - Q_{RECIRCULATION} - Q_{LIP}\right]^2 - \frac{\rho_{AIR}}{A_N}\left[Q_{AIR,IN} - Q_{AIR,OUT}\right]^2 \tag{74}$$

Where $Q_{AIR,IN}$ is the flow rate of air into attenuator air pad (m^3/s), $Q_{AIR,OUT}$ is the flow rate of air out of the attenuator air pad (m^3/s) and ρ_{AIR} represents the density of air (kg/m^3). The density of air, ρ_{AIR} is given as:

$$\rho_{AIR} = \frac{P_{ATT} MW_{AIR}}{RT_{ATT}} \tag{75}$$

Where P_{ATT} is the absolute gas pressure in the attenuator (Pa), MW_{AIR} is the average molecular weight of air (kg/kg mole), R is the gas constant (8314 m^3·Pa/kg mole·K) and T_{ATT} represents the absolute temperature of gas in the attenuator (K).

The flow of air entering or exiting the attenuator air pad can be determined using the Fisher Gas equation (Equation (24)). To relate the dynamics of the attenuator to the hydraulic headbox, the following algebraic equation describing the total head at the base of the attenuator is required:

$$H_{INT} = X_O + X + \frac{\left(P_{ATT} - P_{ATM}\right)}{\rho g} \tag{76}$$

The rate of change of the air pressure in the attenuator, P_{ATT} can be determined using Equations (48-50).

$$\frac{dP_{ATT}}{dt} = \frac{RT_{ATT}}{V_{ATT}}\frac{dN_{ATT}}{dt} - \frac{P_{ATT}}{V_{ATT}}\frac{dV_{ATT}}{dt} \tag{48}$$

$$\frac{dN_{ATT}}{dt} = \frac{P_{ATT}\left[Q_{AIR_{IN}} - Q_{AIR_{OUT}}\right]}{RT_{ATT}} \tag{49}$$

$$\frac{dV_{ATT}}{dt} = -A_N \frac{dX}{dt} \tag{50}$$

Where N_{ATT} refers to the number of moles of air in attenuator air pad (kg mole) and V_{ATT} refers to the volume of the attenuator (m^3).

To prevent the membrane from getting damaged during operation, the pressure in the attenuator air pad is set at the same pressure set-point requested at the slice. Varying the exhaust valve position could be used to control the air pressure within the attenuator air pad.

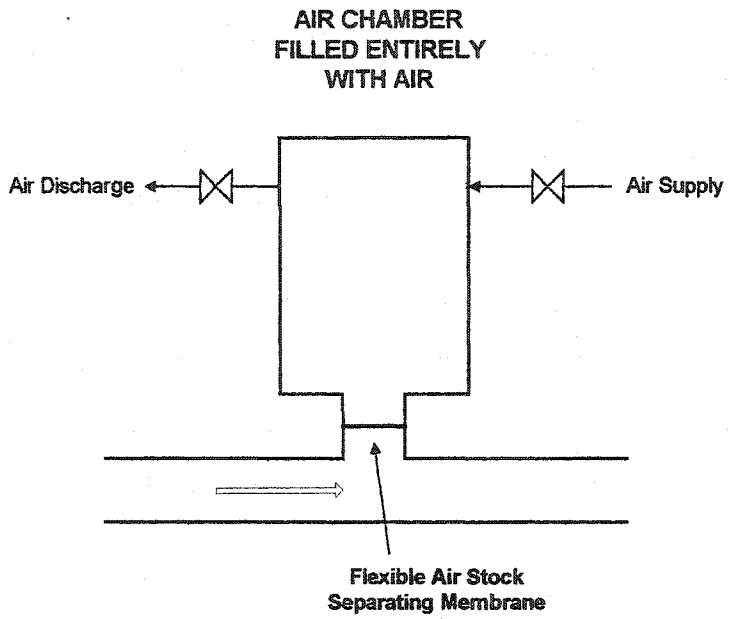

Figure 51: Air Chamber Attenuator With A Diaphragm

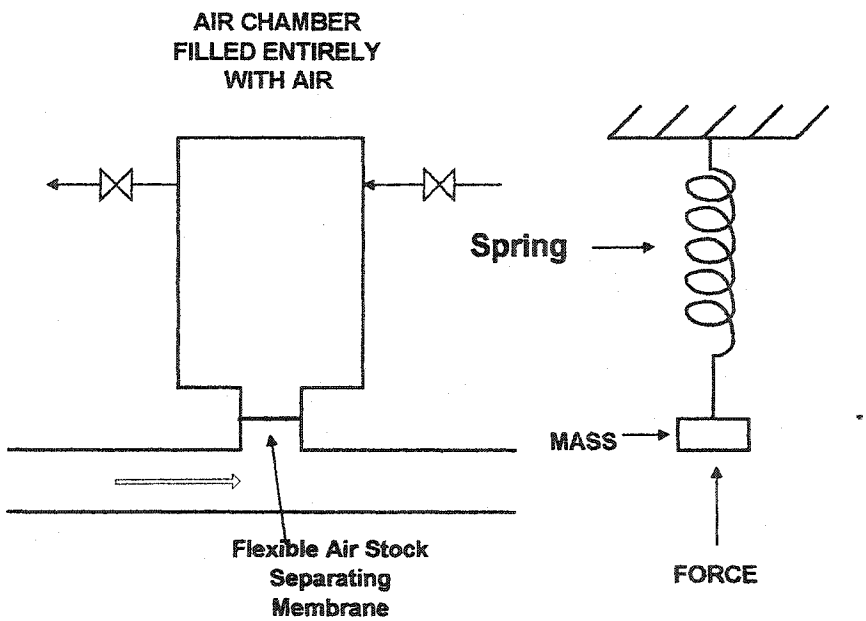

Figure 52: Attenuator/ Spring Analogy

REFERENCES

1. Leask, R.A., "Pulp and Paper Manufacture 3rd Edition, (Volume 2 Mechanical Pulping)", The Joint Textbook Committee of the Paper Industry, Montreal, Que., pp. 181,206, (1987).
2. Odell, M. H., "Report on Technical Comparison of Hydraulic Headboxes", (June 1979).
3. Smook, G.A., "Handbook for Pulp & Paper Technologists, 2nd Edition", Angus Wilde Publications Inc., Vancouver, B.C., pp. 1,3,30,38,163,228,229,230,234,237, (1994).
4. Hautamaki, R., "Sym-nozzle headbox", Technical paper from the Valmet Corporation.
5. Technical paper presented at the International Symposium on paper machine headboxes, Dept. of Chemical Engineering, McGill University, Montreal, (1979).
6. Lebeau B., Arrese, R., Bauduin, S., Grobet, R., Foulard, C. "Non-Interacting Multivariable Paper Machine Headbox Control: Some comparisons with Classical Loops", Proc. 4th IFAC Conf on Instr. & Automation, Ghent, pp. 227-38 (1980).
7. Tuladhar, A., Davies, M.S., Yim, C., Woods, G.R., "Headbox Modeling and Wet End Pressure Pulsations Analysis", Pulp and Paper Canada, 98:9, (1997).
8. Bateson, R.N., "Introduction to Control System Technology, 5th Edition", Prentice Hall, Columbus, Ohio, pp. 158,436,444,445,446,449, (1996).
9. Slemon, G.R., & Straughen, A., "Electric Machines", Addison-Wesley, Don Mills Ont., pp. 290, (1992).
10. Streeter, V. L., & Wylie, E.B.,"Fluid Mechanics, 8th Edition", McGraw-Hill, New York, pp. 398,536, (1985).
11. Ahlstrom Technical Services Inc., 1630-N Provencher, Brossard, Quebec, J4W 2VC, (1988).
12. Foust, A.S., & Wenzel, L.A., & Clump, C.W., & Maus, L.& Anderson, L.B., "Principles of Unit Operations", John Wiley & Sons Inc., (1980).
13. http://www.fisherregulators.com/technical/sizingcalculations/
14. Geankoplis, C.J. "Transport Processes and Unit Operations 3rd Edition", Prentice Hall, New Jersey, pp. 132, (1993).
15. Rempel, C., "The Converflo-A High Turbulence Headbox", Beloit Corporation, Beloit, Wisconsin, pp. 49-52.
16. Hack, K., "Modern Headbox Operation", Paper Technology and Industry, pp. 58-59, (March 1979).

17. Mardon, J. and Hauptmann E.G. "Design of Hydraulic Surge Suppression Devices" Volume 7, No. 4, (September 1981).
18. Gilbert, A.F., & Natarajan, K., "Modelling and Control Design for a Headbox Section of a Paper Machine", Manuscript Submitted to: IEE Proceedings- D Control Theory and Applications, pp. 1-26, (2001).
19. Mott, R.L., "Applied Fluid Mechanics 4th Edition", Prentice Hall, New Jersey, pp. 380, (1994).
20. Bennington, C. and Kerekes, R.J., "Power requirements for pulp suspension fluidization", Vol. 79, No 2, Tappi Journal, (1996).
21. Munson, B., & Young, D., & Okiishi, T., "Fundamentals of Fluid Mechanics 3rd Edition", John Wiley & Sons, Inc., Toronto, (1998).
22. The Boeing Company, "EASY5 User Guide", Seattle Washington, (1998).
23. Marlin, T. E., "Process Control – Designing Processes and Control Systems for Dynamic Performance", McGraw-Hill Inc., New York, pp. 201-211,350,351,435,644,650-659, (1995).
24. Nelder, J.A., & Mead, R., "A Simplex Method for Function Minimization", Computer Journal, Vol. 7, pp. 308-313, (1965).
25. Lindstrom, R., "A Study of Headbox Pressure and Level Control Systems", Paper Trade Journal, (March 30, 1970).
26. Smith, B.W., "The Automatic Control of Pressurized Flowboxes", Australian Paper Manufacturers Ltd., (May 1968).
27. Gilbert, A.F., & Yousef, A., & Natarajan, K., & Deighton, S., "Tuning of PI controllers with One-Way Decoupling in 2 x 2 MIMO Systems Based on Finite Frequency Response Data", Lakehead University, Thunder Bay, Ontario, pp. 3, (2001).
28. Henrikson, L., & Gunnarson, K., & Torok, V., "Variable-Speed Blower For Total Head Control", Tappi Journal, Vol. 54, No. 9, (September 1971).

NOMENCLATURE

α = discharge coefficient of slice channel (dimensionless)

α, β = weighting factors for minimization of IAE for MIMO systems

δ = weighting factor (dimesionless)

λ_{ij} = RGA element row i, column j

η = pump efficiency (fraction)

θ = process dead-time (s)

ΔP = pressure difference across valve (psi)

ρ = density of stock (kg/m^3)

ρ_{AIR} = density of air (kg/m^3)

τ = process time-constant (s)

τ_{LAG} = lag time constant of lead/lag decoupler (s)

τ_{LEAD} = lead time constant of lead/lag decoupler (s)

μ =stock viscosity (Pa·s).

μ_{AVG} = average viscosity of stock around control volume (Pa·s)

$\mu_{AVG,C}$ = average stock viscosity at temperature T, (Pa·s)

$\mu_{AVG,20}$ = average stock viscosity at reference temperature, (Pa·s)

a = variable used to reproduce fan pump characteristic curves (m·s^2/rad^2)

A,B,C,D = state space matrices

A_0 = area of holes in orifice plate (m^2)

A_1 = cross-sectional area of pipe section into attenuator (m^2)

A_{EQUAL} = cross-sectional area of headbox above weir (m^2)

$A_{HEADBOX}$ = cross sectional area of headbox (m^2)

A/L = effective area/length ratio of control volume (m)

$(A/L)_1$ = effective area to length of control volume *1*

$(A/L)_2$ = effective area to length ratio of control volume *2* (m)

A_{LIP} = area of headbox slice (m^2)

A_N = cross-sectional area of piping section into attenuator (m^2)

A_{ATT} = cross-sectional area of attenuator (m^2)

b = variable used to reproduce fan pump characteristic curves ($s^2/(m^2 \cdot rad)$)

B = bone dry mass of fibre in sample (kg)

B_L = viscous friction of pump ($N \cdot m \cdot s/rad$)

B_M = viscous friction of motor ($N \cdot m \cdot s/rad$)

B_{TOTAL} = total viscous friction of motor / pump combination ($N \cdot m \cdot s/rad$)

c = variable used to reproduce fan pump characteristic curves (s^2/m^5)

$C0$ = consistency of stock entering fan pump (%)

$C_1 = C_g/C_V$

$C1$ = consistency of stock entering pressure screen (%)

$C2$= consistency of stock exiting "accepts" stream of pressure screen (%)

$C3$ = consistency of stock exiting headbox slice (%)

C_{AVG} = average consistency of stock (%)

C_D = discharge coefficient of attenuator orifice plate (dimensionless)

C_g = gas sizing coefficient (dimensionless)

C_M = mechanical capacitance (N/m)

C_V = liquid sizing coefficient ($USGPM/psi^{1/2}$)

CV_i = control variable (total pressure at headbox slice, stock level)

d = variable used to reproduce fan pump characteristic curves (m)

$D_{21}(s)$ = decoupler transfer function (pressure loop to level loop) (%/%)

e_1, = variable used to relate efficiency of pump at different operating points ($\% \cdot rad/m^3$)

e_2 = variable used to relate efficiency of pump at different operating points ($\% \cdot rad^2/m^6$)

$ERI(t)$ = integrated error signal of PI controller (%)

E, F = constants for Andrade's Equation

f_1 = head loss coefficient for control volume *1* (s^2/m^5)

f_2 = head loss coefficient for control volume *2* (s^2/m^5)

F_{NET} = net force acting on the diaphragm (N)

$G_{11}(s)$ = open-loop process gain relating pressure controller output (fan pump armature voltage) to total pressure at slice (%/%)

$G_{12}(s)$ = open-loop process gain relating level controller output (bleed valve) to total pressure at slice (%/%)

$G_{21}(s)$ = open-loop process gain relating pressure controller output (fan pump armature voltage)

to stock level (%/%)

$G_{22}(s)$ = open-loop process gain relating level controller output (bleed valve) to stock level (%/%)

g = gravitational acceleration constant (9.81 m/s^2)

G_{AIR} = gas specific gravity (for air = 1.0)

Gas_{LEVEL} = gas level in attenuator (m)

G_{RATIO} = ratio of number of teeth in pump gear to number of teeth in motor gear (dimensionless)

h = stock level above jet (m)

H_{ATT} = height of attenuator (m)

$H_{HBX\ HEADER}$ = Total head at the headbox distributor (m)

H_{INT} = total head of stock inside the attenuator (m)

H_{LIP} = total head at slice (m)

$H_{ORIFICE}$ = head loss through attenuator orifice plate (m)

H_{PUMP} = total head generated by fan pump (m)

H_{S2} = elevation difference between the bottom of the headbox and discharge valve (m)

H_{STATIC} = difference in elevation between headbox and fan pump (m)

H_{TOTAL} = total head at valve opening (m)

I_A = armature current (ampere)

J_L = moment of inertia of pump ($N{\cdot}m{\cdot}s^2/rad$)

J_M = moment of inertia of motor ($N{\cdot}m{\cdot}s^2/rad$)

J_{TOTAL} = total inertia of motor / pump combination ($N{\cdot}m{\cdot}s^2/rad$)

K = steady-state gain of decoupler $D_{21}(s)$ (%/%)

K_A = armature reaction constant (ohm)

K_B = back electromotive force constant ($V{\cdot}s/rad$)

K_{ATT} = attenuator gas constant ($Pa{\cdot}(m^3)^N$)

K_C = proportional control gain of PI controller (%/%)

K_I = Integral control gain of PI controller ($sec.^{-1}$)

K_L = limiter gain of PI controller (dimensionless)

K_P = steady-state gain

K_T = motor torque constant ($N{\cdot}m/A$)

L_A = armature inductance (Henry)

L_{EQUAL} = level of stock on backside of weir (m)

$Level_{GAS}$ = level of gas in the attenuator (m)

L_{STOCK} = level of stock being controlled (for the weir headbox this is the level after the weir) (m)

L_{WEIR} = height of weir (m)

M_{MEM} = mass of attenuator diaphragm (kg)

M_T = total mass of diaphragm and mass of fluid "plug" of attenuator neck section (kg)

MV_j = manipulated variable (armature voltage, air bleed valve position)

MW_{AIR} = average molecular weight of air (kg/kg mole)

N = polytrophic exponent (1.2 for air)

N_{AIRPAD} = moles of air in the air pad at any time t, (kg mole)

N_{ATT} = number of moles of air in attenuator air pad (kg mole)

P = absolute pressure of gas in attenuator (Pa)

P_{AIRPAD} = air pressure in air pad (Pa)

P_{ATM} = atmospheric pressure (Pa)

P_{ATT} = absolute gas pressure in attenuator (Pa)

P_1 = inlet pressure to valve (psia)

P_i = i'th point of simplex containing controller parameters

P_0 = initial point of simplex containing controller parameters

P_{GAUGE} = gauge air pressure (Pa)

P_{LIP} = total pressure at lip (Pa)

Q_{AIR} = flow of air in/out of air pad (scfh)

$Q_{AIR,IN}$ = flow rate of air into attenuator air pad (m^3/s)

$Q_{AIR,OUT}$ = flow rate of air out of attenuator air pad (m^3/s)

$Q_{DISCHARGE}$ = flow through headbox discharge valve (m^3/s)

$Q_{HEADBOX}$ = flow of stock into headbox (m^3/s)

Q_{INT} = "accepts" flow from primary pressure screen (m^3/s)

Q_{LIP} = flow of stock out through slice (m^3/s)

Q_{PUMP} = flow from pump (m^3/s)

$Q_{RECIRCULATION}$ = flow of stock that passes through headbox distributor (m^3/s)

$Q_{REJECTS}$ = flow of stock rejected by pressure screen (m^3/s)

Q_{WEIR} = refers to the volumetric flow of stock over weir (m^3/s)

R = gas constant (8314 m^3·Pa/kg mole·K)

R_A = armature resistance (ohm)

R_C = fibre distribution ratio (consistency of reject stream : consistency of feed stream)

R_R = reject ratio from pressure screen (fraction)

R_M = mechanical resistance (N·s/m)

$S_1(t)$, $S_2(t)$ = input and output of PI controllers (%)

t = time (s)

$T_{11}(s)$ = closed-loop process gain relating pressure set-point to total pressure at slice (%/%)

$T_{12}(s)$ = closed-loop process gain relating level set-point to total pressure at slice (%/%)

$T_{21}(s)$ = closed-loop process gain relating pressure set-point to stock level (%/%)

$T_{22}(s)$ = closed-loop process gain relating level set-point to stock level (%/%)

T = absolute temperature (Kelvin) or torque developed by DC motor (N·m)

T_A =effect that armature reaction has on the induced Bemf of DC motor (N·m)

T_{AIRPAD} = average absolute temperature of air in air pad (Kelvin)

T_{ATT} = absolute temperature of gas in attenuator (Kelvin)

T_{LOAD} = torque of pulp stock on pump (N·m)

u_0 = steady-state values of controller outputs (%)

U_i = i'th unit vectors

V = stock jet velocity (m/s)

V_A = applied armature voltage (V)

V_{ATT} = volume of gas in attenuator (m^3)

V_{AIRPAD} = represents the volume of air-pad (m^3)

V_B = Back electromagnetic force (V)

V_{GAS} = gas volume (m^3)

V_L = voltage through inductance (V)

V_M = armature reaction voltage (V)

Vol_1 = volume of control volume from fan pump to pressure screen (m^3)

Vol_2 = volume of pressure screen (m^3)

Vol_3 = volume of control volume from pressure screen "accepts" to the headbox slice (m^3)

$V_{HEADBOX}$ = maximum capacity (liquid + air) of headbox (m^3)

V_R = voltage through resistor (V)

W_{HBX} = width of headbox (m)

W_{PUMP} = speed of pump (rad/s)

x = vector of state variables

x_0 = vector of steady-state values of state variables

X = centreline position of diaphragm (m)

X_0 = height of fluid in attenuator "neck" (m)

$X(s)$ = input variable

$Y(s)$ = output variable